Optical and Fluorescent Biosensor Based on Liquid Crystals

Xiaoxue Du

Submitted in accordance with the requirements for the degree of Doctor of Philosophy in the faculty of Engineering and Physical Science

The University of Leeds
Faculty of Engineering and Physical Sciences
School of Physics and Astronomy

October 2022

Declaration

The candidate confirms that the work submitted is her own and that appropriate credit has been given where reference has been made to the work of others. The contribution of the candidate and the other authors to this work has been explicitly indicated below. The candidate confirms that appropriate credit has been given within the thesis where reference has been made to the work of others.

For my family and friends

Acknowledgements

During this PhD period, I had many valuable experiences and really gained a lot from them. Not only the study in lab but also the daily life in the new environment left me the precious wealth. Due to this opportunity to study in a totally different city and different country, I met some new friends based on different cultures, and know more about some topics from the global view. There are really lots of people that I must thank for attendance in my past fantastic years.

Firstly, I would like to thank my supervisor Professor Helen Gleeson, Professor Stephen Evans and Professor Dan Luo. On behalf of their guidance and kind help, I can enjoy a happy and fulfill PhD life in the past four years. When I faced up with difficulties, they were always giving some useful suggestions in time. In my past student life, I was used to solve problems all by myself instead of asking for help. I was afraid to be a student with a lot of questions. However, no one will be familiar with each field, it will take me a lot of time in early searching. Helen told me to be optimistic about asking others for help. It truly changed my principle in research. I can overcome the problems in study more efficiently due to the cooperation with others which were more professional in those fields. Each time when I feel nervous or not confident, they were always giving me encouragement to keep going.

This research has been carried out by a team which has included Daniel Paterson, Bao Peng, Sally Peyman, Jonathan Sandoe, Stephen Evans, Richard Bushby, and Cliff Jones. Here I want to express my thanks to their contributions to my project and thesis.

Thanks to the Soft Matter Physics group and the Molecular and

Nanoscale Physics group in faculty of Engineering and Physical Science for the support in my study. I obtained lots of training opportunity and enjoyed fantastic experiment environment with their help. I would like to give exceptional thanks to all the seniors in the lab for their kind guidance. When I faced up with some difficulties, they are always coming to give me some useful suggestions without any hesitations.

What is more, University of Leeds and Southern University of Science and Technology are significant for me in the past days. They both give me supports to finish this PhD education. Because of them, I have this opportunity to be here and submit this thesis.

Lastly, but not least, I want to thank my family and friends for their selfless support. Thanks to my mom and dad for giving a birth and raising me up over the 26 years. In the past days, they offer me a carefree living environment, so that I can live a happy life and go to further education as I pleased. My parents play the important roles during my growing up, including the establishment of world view, outlook on life and values.

Abstract

As the perception of liquid crystals gradually deepens, more researchers try to apply different phases of liquid crystals and different configurations of them to various fields. A detailed research study of sensors based on liquid crystals in different configurations is presented in this thesis. There are four main topics involved as described in the following.

The first part of this thesis presents a general background of the project, the materials properties and the experimental techniques. The preparation of cholesteric liquid crystal (CLC) droplets with a lipid monolayer coating is described, for potential applications with the aim of producing biological sensors. The liquid crystal director alignment in the droplets is sensitive to the surface anchoring. The responsivity of the surface to biological materials alters the surface anchoring and therefore provides a mechanism for sensing biological materials.

Microfluidic chips have become an important direction in the development of analytical instruments. Recently, microfluidic chips based on polydimethylsiloxane (PDMS) have been widely used in studies due to their ease of use and fabrication and their low cost. In this project, we have produced a PDMS microfluidic chip to make uniform droplets with the size of 60 μm. These droplets are made up of nemetic liquid crystal, chiral dopant and azobenzene liquid crystal. We can use UV light to change the topology of the director structure in the initially uniform chiral nematic liquid crystal droplets. Several topological configurations have been demonstrated under one-directional illumination of UV light such as closed-ring structures with cone-shaped centers and concentric elliptical centers, and open-rings structures. Structures with parallel CLC stripes center and with central point

singularity can be formed under multi-directional UV illumination. A wide range of potential applications in biosensors and microlasers are made possible by the fact that all of the proposed configurations of CLC droplets are stable and light controllable.

Most existing ion detection methods suffer from time consuming, complicated sample pre-treatment, and expensive equipment, which hinder their broad use in real-time detection. Herein, we show a new fluorescent sensor for detecting lead ions derived from liquid crystals doped with an aggregation-induced emission luminogen. The proposed fluorescence sensor exhibits a low detection limit of 0.65 nM. The detection ranges of the Pb^{2+} fluorescence sensor is broad, from 20 nM to 100 μM, and it also select lead ion from numerous metal ions exactly, resulting in a highly sensitive, highly selective, simple and low-cost detection strategy of Pb^{2+} with potential applications in chemical and biological fields. This approach to designing a liquid crystal fluorescence sensor offers an inspiring stage for detecting biomacromolecule or other heavy metal ions by varying decorated molecules.

It is known that liquid crystal elastomers can achieve a large elongation compared to normal liquid crystal films. When the liquid crystal elastomers doped with an aggregation-induced emission luminogen, a fluorescent liquid crystal elastomer can be obtained. In this situation, a force can lead to the liquid crystal film’s elongation, which will in turn cause the change of the fluorescence intensity. Between the force of 0 ~ 2.5 N, the maximum strain was 316.4%, causing a 66.808 (a.u.) change in fluorescence intensity. As a result, the force can be calculated through the relationship with the fluorescence intensity caught by the digital single lens reflex camera.

In the last section of the thesis, overall conclusions are presented and suggestions for further research are proposed. Our ultimate aim is to use lipids

that are sensitive to external influences, such as toxins, to realize a highly sensitive, cheap, and fast sensor. This thesis offers a wide-ranging starting point to achieve this aim.

List of Publications

Journal publications

Xiaoxue Du, Yanjun Liu, Fei Wang, Dongyu Zhao, Helen F. Gleeson and Dan Luo, “A Fluorescence Sensor for Pb^{2+} Detection Based on Liquid Crystals and Aggregation-Induced Emission Luminogens”, *ACS Appl. Mater. Interfaces,* 2021, 13, 19, 22361–22367. (This work refers to Chapter 7)

Daniel A. Paterson, Xiaoxue Du, Peng Bao, Parry Adele, Sally A. Peyman, Jonathan A. T. Sandoe, Stephen D. Evans, Dan Luo, Richard J. Bushby, J. Cliff Jones and Helen F. Gleeson, “Chiral Nematic Liquid Crystal Droplets as a Basis for Sensor Systems”, *Molecular Systems Design & Engineering,* 2022, 7, 607-621. My contribution is the part of experimental work and manuscript writing. (This work refers to Chapter 5)

Xiaoxue Du, Fei Yang, Yanjun Liu, Helen F. Gleeson, Dan Luo, “Light-driven dynamic hierarchical architecture of three-dimensional self-assembled cholesteric liquid crystal droplets”, *Langmuir,* 2023, 39, 1611-1618. (This work refers to Chapter 6)

Xiaoxue Du, Yanjun Liu, Dongyu Zhao, Helen F. Gleeson, Dan Luo, “Fluorescent force sensor based on liquid crystals and aggregation-induced emission luminogens”, *(in submission).* (This work refers to Chapter 8)

Poster presentations

“Cholesteric liquid crystal droplets with lipid modification: towards novel biological sensors”, British Liquid Crystal Society Conference 2019, Leeds, UK, 2019.

“Highly sensitive and selective liquid crystal optical sensor”, 2nd Photonic Technology Conference in China, Guangzhou, China, 2020.

“Highly sensitive fluorescence sensor based on liquid crystals and

aggregation-induced emission luminogens", CPS Fall Meeting 2020/2021, Lanzhou, China, 2021.

"A Fluorescence Sensor for Pb^{2+} Detection Based on Liquid Crystals and Aggregation-Induced Emission Luminogens", 28^{th} International Liquid Crystal Conference, Lisbon, Portugal, 2022.

Table of Contents

Abbreviations

5CB	4-pentyl-4’-cyanobiphenyl
3D	Three-dimensional
ACQ	Aggregation-induced emission
AIE	Aggregation-caused quenching
APTES	(3-Aminopropyl) triethoxysilane
Azo-LC	Azobenzene liquid crystals
CCD	Charge coupled device
CLC	Cholesteric liquid crystal
CNT	Carbon nanotubes
DI water	Deionized water
DF	Di-ferro
DMOAP	1,2-dineopentadecane-sn-glycero-3-phosphocholine
DnPdPc	Dimethyloctadecyl [3-(trimethoxysilyl) propyl] ammonium chloride
DOPC	1,2-dioleoyl-sn-glycero-3-phosphocholine
DOPG	1,2-dioleoyl-sn-glycero-3-[phospho-rac-(1-glycerol)]
DPA	Dipropylamine
DSC	Differential scanning calorimetry
DTAB	Dodecyl trimethyl ammonium bromide
EDDET	2,2'-[1,2-Ethylenedioxy] diethanethiol
GA	Glutaral
GO	Graphene-Oxide
HTP	Helical twisting power
ISO	International Organization for Standardization
LC	Liquid crystal
LCE	Liquid crystal elastomer
LOD	Limit of detection
PBG	Photonic band gap

PCs	Photonic crystals
PDLC	Polymer-dispersed liquid crystal
PDMS	Polydimethylsiloxane
PETMP	Pentaerythritol tetrakis (3-mercaptopropionate)
PL	Photoluminescence
POM	Polarized optical microscope
PVA	Polyvinyl alcohol
RM257	1,4-Bis-[4-(3-aryloyloxypropyloxy) benzoyloxy]-2-methylbenzene
SDS	Sodium Dodecyl Sulfate
SLR	Single lens reflex
SF	Single ferro
TEM	Transmission electron microscopy
TPE-PPE	Tetraphenylethylene-propylphenylethyne
UV	Ultraviolet
VOC	Volatile organic compound

List of Symbols

$\vec{n}$	Vector of the liquid crystal phase
n	Refractive index
$\bar{n}$	Average refractive index
n_e	Extraordinary refractive index
n_o	Ordinary refractive index
Δn	Birefringence
λ	Wavelength
$\Delta\lambda$	Linewidth of photonic band
p	Helical pitch
x_c	Concentration of the chiral material
R	Radius of droplets
r	Curvature radius
θ	Threshold angle
σ	Standard deviation
I	Fluorescence intensity
ΔI	Changes of fluorescence intensity
S_{strain}	Tensile strain
S_{stress}	Tensile stress
F	Force applied to the LCE
W	Width of the clamp in the tensile-testing machine
t	Thickness of the LCE sample at the cutter area
E	Elongation of the LCE
L_0	The original length of the LCE
L	The final length of the LCE
R^2	Goodness of fit

List of Figures

List of Tables

Chapter 1 Motivation and direction

The aim of this thesis was simple at the outset:

"Optical and Fluorescent Biosensor based on liquid crystals."

In recent years, liquid crystals (LCs) have been widely applied to detect weak external stimuli and have attracted significant attention as a promising branch of highly sensitive, quick-response, and low-cost materials. By enlarging and altering molecular occurrences in environment, LCs produce macroscopic signals. It is possible to use LCs to react to alterations in the environment or the presence of binding events. Since specific bonding events between biomolecules have an impact on LC molecules' orientation, which is the cornerstone of LC-based sensing platforms, LCs have been extensively exploited as sensitive elements in LC biosensors.

This thesis will begin with the introduction of the fundamental of liquid crystals including its phase and phase transition, optical properties, and various formations in chapter 2. Chapter 3 presents that many research groups have been devoted to developing LC-based biosensors due to their self-assembly potential and functional diversity. This chapter is based on the literature review. The materials, equipment and experimental methods utilized in the following experiments will then be described in chapter 4 before diving into the experimental results and discussion half of this thesis.

Chapter 5 showed a sensor based on the liquid crystal droplets modified with different lipids. The molecular orientation will change due to the effect of modification. A macroscopic signal can be caught to reflect the molecular level changes. It's attractive to investigate in the context of a variety of sensing applications based on the liquid crystals. Chapter 6 described a sensor based

on the liquid crystal droplets induced by UV light. Several novel 3D dynamic hierarchical architecture in the cholesteric liquid crystal (CLC) droplets can be obtained by the UV light's induction. Chapter 7 demonstrates a lead ion sensor based on the liquid crystal and aggregated-induced emission materials. A highly sensitive, highly selective, simple and low-cost detection strategy for Pb^{2+} with potential applications in chemical and biological fields can be achieved. Chapter 8 illustrates a fluorescence and force sensing actuator based liquid crystal elastomer. A useful sensor in situations where direct measurement is difficult, such as unreachable distances, watery environments, and hazardous surroundings can be provided. Then the thesis will be summarized in chapter 9. All the works in this thesis are based on the flexible use of liquid crystal orientation's changes and combination of several functional materials.

Chapter 2 Introduction to Liquid Crystals

As the perception of liquid crystals gradually deepens, more researchers try to apply different phases and forms of liquid crystals to various fields. For my thesis, the optical and fluorescence biosensor based on liquid crystals, liquid crystals play a crucial role in this topic. The properties of the various liquid crystals determine their application fields. So, the background of the liquid crystals including the classification and the formation is necessary to be explored before the projects.

Liquid crystal materials and samples can be classified in ways that describe both the phase type and the bulk sample; both are important to the optical and other properties observed. For example, according to the formation conditions, they can be divided into lyotropic and thermotropic liquid crystals. Lyotropic liquid crystals are crystals formed by the dissolution of an amphiphilic mesogen in a suitable solvent (for example, a mixture of soap in water), whereas thermotropic liquid crystals are crystals with a mesophase that exist within a certain temperature range. The main distinction is that the former only have mesophase, while the latter might have a number of different phases. The thermotropic materials usually have nematic, smectic and cholesteric states. Nematic liquid crystal is utilized in the most following work.

2.1 Liquid crystal phases and the phase transition

The phases of liquid crystals can be characterized by the type of ordering, and phase transitions can be induced by the external environment. In a liquid crystal phase, a vector, $\vec{n}$, can be defined as the "director" about which the molecules are preferentially oriented (Figure 2.1). The long axes of the molecules will tend to align in this direction. The macroscopic orientation of the director can be influenced by external electric fields, external magnetic fields, surface treatments and chiral agents.

The most common classification of thermotropic liquid crystals, whose properties are controlled by temperature, is into three phases: nematic (N), smectic (Sm) and chiral nematic (or cholesteric) (N*) phases. Figure 2.1 shows the structures of the three phases. The least ordered phase is the nematic phase, which has only long-range orientational order (Figure 2.1a). In this situation, the long axes of the molecules point in the same direction on average. The order of phase will increase as the temperature decreases. Higher order liquid crystal phases are the so-called smectic phases, which combine orientational order with positional order (Figure 2.1b). The chiral nematic phase, in fact, was the first liquid crystal discovered, by Reinitzer in 1888; it is also called a cholesteric liquid crystal, because the original materials were derivatives of cholesterol [1]. The molecules are chiral and can be described as have left or right handedness. There is actually no layered structure as suggested by Fig.2.1c and the local ordering is identical to that of the nematic phase. The defining length scale of this phase is the pitch p, the distance over which the director rotates through an angle of 2π (Figure 2.1c shows the half pitch $\frac{p}{2}$ for rotating π) [2-4]. A chiral nematic phase can be induced in a nematic material through the addition of a small concentration of chiral dopant molecules. The chiral dopant are liquid crystal materials. They are optically active chemicals that create helical structures in a host nematic liquid crystal mixture. Liquid crystals are made up of mesogenic molecules, which have orientational order. A chiral molecule has a mirror impact image that is different from itself. However, for nematic liquid crystal, the mirror image is identical to itself. In the nematic phase, long axes of molecules are aligned along the liquid crystal director, which is a single direction. In its initial state, the liquid crystal director is unidirectional in space. A liquid crystal director bends in space if a constituent molecule (or a constituent component) is chiral. Increasing the concentration of dopant molecules will lead to increasing twisting power, and shortening of the pitch.

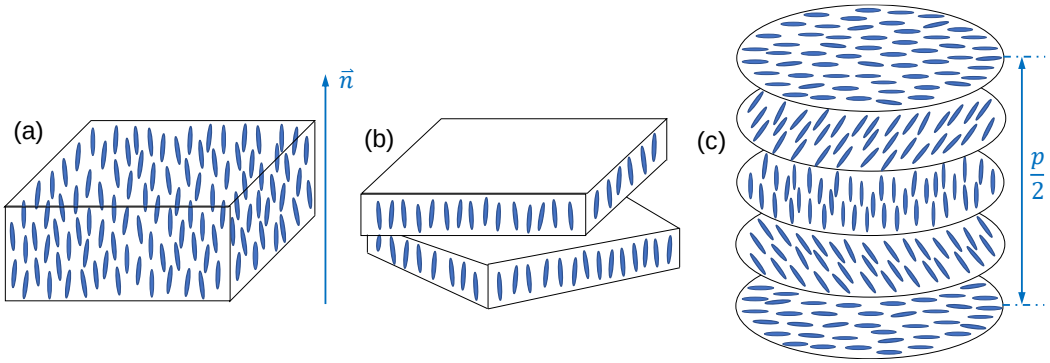

Figure 2.1 The three phase states of thermotropic liquid crystal
(a) nematic phase; (b) a smectic phase; (c) chiral nematic phase.

The phases of a liquid crystal can be characterized by the type of ordering, and a phase transition can occur in response to the external environment (temperature, pressure, UV illumination etc). Alternatively, the application of external electric fields, external magnetic fields, or surface treatments, can influence the bulk orientation of a liquid crystal sample.

In order to obtain a required liquid crystal's alignment, some methods are utilized to control the orientation of the liquid crystal's director. There are multiple ways to align liquid crystals depending on the desired result, such as micro-rubbing [5-6], direct laser writing [7-8], nanoimprinting [9-11], photoalignment [12] and chemical surface induction [13-14]. Even the rubbing method cannot provide a high resolution, it is still often used for liquid crystal displays due to its mature technique. As for chemical surface induction, both homeotropic and planar alignment can be realized through this method.

2.2 Optical properties of chiral nematic liquid crystal

Cholesteric liquid crystals (CLC) exhibit a number of exceptional optical properties that are not found with the nematic phase [2]. The helical structure of the N* phase leads to a photonic bandgap so that when the pitch is of the same order as the wavelength of light, selective reflection can occur. The central wavelength of the chiral nematic liquid crystal's reflection spectrum can be calculated by the equation:

$$\lambda = \bar{n} \times p, \tag{2-1}$$

where $\bar{n}$ is the average refractive index, and p is the pitch of CLC chiral structure. The pitch can be deduced from the relationship of

$$p = [HTP \times x_c]^{-1}, \tag{2-2}$$

where HTP is the helical twisting power and x_c is the concentration of the chiral material respectively in a mixture. The linewidth $\Delta\lambda$ of the photonic band gap is determined by

$$\Delta\lambda = p \times \Delta n, \tag{2-3}$$

where Δn is the birefringence, given by

$$\Delta n = n_e - n_o, \tag{2-4}$$

where n_o is the ordinary refractive index and n_e is the extraordinary refractive index of the liquid crystal [3]. The PBG is caused by a lattice or a crystal structure. Materials with a periodic dielectric profile are called PBG material, which can block the propagation of light at certain frequencies or wavelengths in one, two, or a variety of polarization orientations. Bragg grating structure is the best known one-dimensional PBG. In our experiments with CLC, the effect is one-dimensional (along the helical axis only) and is only present for one handedness of circularly polarised light. These materials, that can form a photonic band gap naturally, have a multitude of potential applications (for example, photonic waveguide, cheaper bio-chemical sensor, solar cell, fluorescent enhance device, color displays, and etc.). Here, in this thesis, the chiral nematic liquid crystals were utilized in lipid coated droplets for the potential of antibody detection and azo-doped droplets for inducing reconfiguration, separately.

2.3 Liquid crystals in the form of droplets

Usually, the term ‘droplet’ is used to describe spherical particles that are less than ~500 μm diameter. The spherical shape means that the liquid crystal director cannot be uniform within the droplet and the structure adopted depends on several factors, including the director orientation at the droplet surface, the anchoring energy and the elastic constants of the liquid crystal. The main structures formed in nematic droplets have been identified [15-17] and transitions between those structures have been studied [18] using several techniques for structure determination that have now become well established (for example, changing the temperature, applying polymer matrix, applying external electric and magnetic fields) [18].

There are two primary director structures for nematic liquid crystal droplets, radial and bipolar, as illustrated in Figure 2.2. Figure 2.2 (a) is a schematic of a radial droplet. It is a nematic droplet in the vertically oriented environment. The radial droplet structure is adopted for strong perpendicular surface alignment, which is optically and structurally anisotropic. The radial structure has only one-point defect at the centre of the droplet; the director field lines point radially from the centre to the surface. Figure 2.2 (b) shows a bipolar droplet. The bipolar structure has strong surface alignment of the liquid crystal director parallel to the boundary. It has two diametrically opposite point defects on the surface, while the director field lines point away radially from the pole of one surface defect and join at the pole at the other.

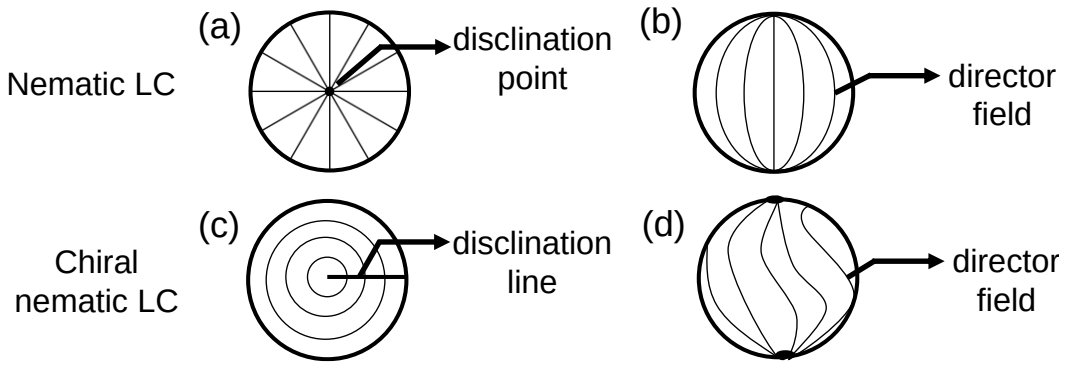

Figure 2.2 The main structures of nematic LC droplets (a & b) and chiral nematic LC droplets (c & d). (a) radial; (b) bipolar; (c) the Frank-Pryce structure; (d) the twisted bipolar structure. The black lines represent the director field of the droplet.

The confined chiral nematic liquid crystal systems have rather more complex structures and defects [19-20]. When a chiral dopant is added, the droplet will have an additional distortion due to the inherent twisting effect. Besides the surface anchoring and elastic constants, the ratio of the droplet radius (r) to the pitch length (p) also plays a role in determining the director configuration. If $\mathrm{p} < \mathrm{r}$, the Frank-Pryce structure occurs. When $\mathrm{p} > \mathrm{r}$, the twisted bipolar structure forms. This is shown in Figure 2.2 where black lines represent the director field of the droplet, and where the director fields end is the point defect [19-22]. Figure 2.2 (c) presents a Frank-Pryce structure in a chiral nematic LC droplet under the perpendicular surface anchoring, while figure 2.2 (d) indicated a twist bipolar structure in a chiral nematic LC droplet.

When fabricating LC droplets, there are several methods can be applied, such as UV or thermally induced phase separation, microfluidic generation, “spinning cup” method, emulsification, etc. In order to control the droplet’s size better and obtain the droplets with uniform size, the microfluidic generation technique is chosen for the later experiment.

2.4 Liquid crystals in the form of elastomers

Liquid crystal elastomers were first reported by Finkelmann in 1981 [23], which are rubbery networks of entropically dominated polymer chains that exhibit mobile liquid crystalline order. The two polymer chains will connect with each

other by the crosslinker. The new chemical bond will appear after the chemical reaction, leading to a network. Generally speaking, liquid crystal elastomers are regarded as the low-crosslinked liquid crystal networks [24]. Normally in the LCE, the T_g (glass transition temperature) is positive related to the crosslinked degree. If the T_g is above the room temperature, it can be regarded networks. If it below the room temperature, it is low-crosslinked networks, which is also an elastomer. As shown in figure 2.3, the liquid crystal elastomers contain anisotropic polymer chains. When heating up to transition temperature (nematic to isotropic phase), the anisotropic polymer chains will turn into isotropic phase temporarily due to the low degree crosslinking, leading to a contraction along the alignment and a reduction in LCE's order. When the temperature is lower than transition temperature (nematic to isotropic phase), the polymer netw'rk's existence assures that the LCE can regain its original orientation. This demonstrates that as the temperature changes, the LCE experiences reversible anisotropic deformation.

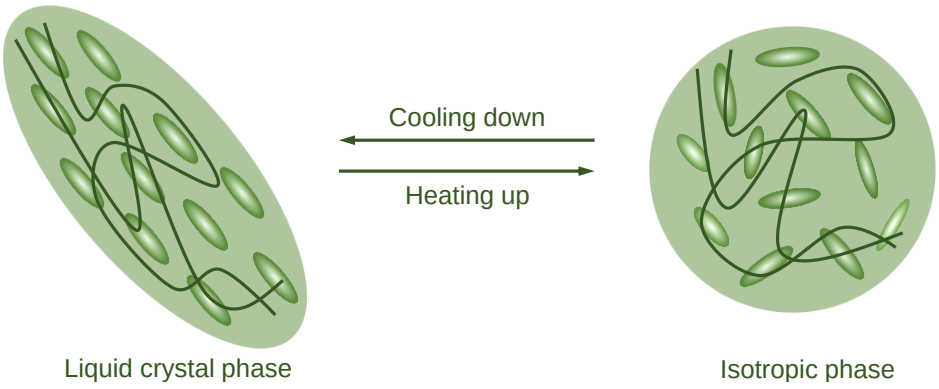

Figure 2.3 The schematic of the contraction along the director of liquid crystal elastomers when changing the temperature. The transition between the liquid crystal phase (left) and the isotropic phase (right) in a liquid crystal elastomer.

There are two mainly two groups of synthetic routes, which are two-step crosslinking and one-step crosslinking. The two-step crosslinking has two steps of crosslinking process. The first step is for forming liquid crystal networks with partial polymerization, and the second step can obtain the strong cross-linked polymer networks which have stable shape and

orientation, such as the liquid crystal elastomer based on polysiloxane reaction or hydrosilylation reaction [23-27]. The preparation of liquid crystal elastomers (LCEs) based on the chain extension reaction of diacrylate-based reactive mesogens (RMs) gets attention due to the easy access to reaction materials. There are two main methods for chain extension reaction of diacrylate-based RMs, aza-Michael addition [25, 26] and Thiol-Michael addition [27]. As for the one-step crosslinking, the polymerizable liquid crystal monomer, cross-linking agent and initiator can be mixed directly without any pre-polymerizations, for example the liquid crystal elastomer with free-radical polymerization of acrylates. The one-step crosslinking without pre-polymerization process leading to a low viscosity of precursor, which is significant for some complex surface orientation [28]. Compared to two-step crosslinking, this method only takes a few minutes to obtain liquid crystal elastomers, which is time-saving.

In general, the stretchability of a liquid crystal elastomer is closely related to its crosslinking degree. In order to obtain a greater tensile capacity, two-step crosslinking method was adopted in our later experiments and only the first step crosslinking reaction was carried out. In the following LCE materials, the RM material is 1,4-Bis-[4-(3-aryloyloxypropyloxy) benzoyloxy]-2-methylbenzene (RM257), the extender is 2,2'-[1,2-Ethylenedioxy] diethanethiol (EDDET), the crosslinker is pentaerythritol tetrakis (3-mercaptopropionate) (PETMP) and the addition catalyst is dipropylamine (DPA). The polymerization process is shown in Figure 2.4.

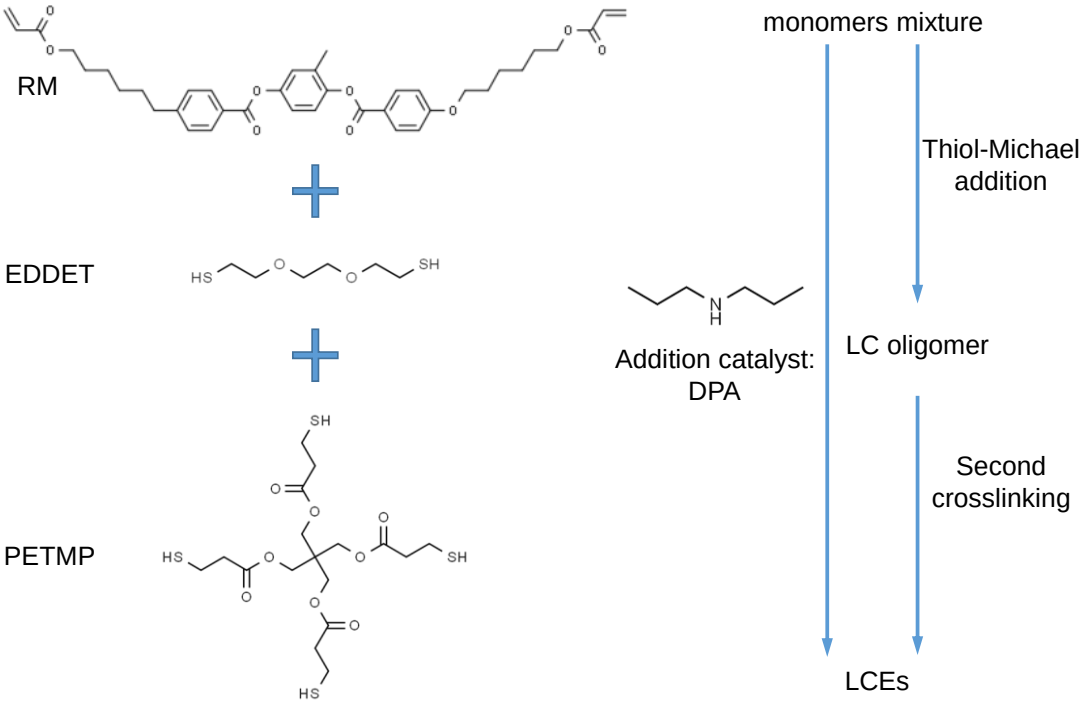

Figure 2.4 The synthetic route for cross-linked liquid crystal chemistry applied in our later experiment, which is called Thiol-Michael addition of diacrylate-based RMs and thiols.

As a kind of popular smart material, liquid crystal elastomers and networks have become the materials of choice for the fabrication of bio-inspired micro/nanostructured surfaces. For further application, many groups combined some functional materials with the liquid crystal elastomer to form a liquid crystal elastomer-based composite material. A responsive photonic crystal with tunable photonic band gap (PBG) can be achieved by combining liquid crystal elastomer with photonic crystals (PCs) [29-37]. A liquid crystal elastomer film with inverse opal was obtained by Li's group for the first time. The liquid crystal elastomer was infiltrated into the opal structure assembled by silica spheres. The film could change the inverse opal structure with thermal stimulation, leading to a blue shift of the Bragg peak [29]. Brannum *et al.* reported a design of photonic crystal with thermally tunable reflection wavelengths using chiral nematic liquid crystal elastomer [30]. It is clear that LCE with photonic crystal structure has the potential of photo-induced mechanical deformation due to the development of photo-thermal conversion materials. The liquid crystal elastomer can also be combined with graphene-

oxide (GO) for a better photo-thermal actuation performance. A photo-triggered dual-phase liquid crystal photonic actuator was proposed by Wei *et al.* The liquid crystal elastomer film can be reversibly bent under the light stimulation owing to the photo-thermal effect of GO. This film is capable of inducing complex changes in its shape and function by selectively photo-patterned UV light at nematic or isotropic state [38]. Certain wavelengths of light can be absorbed by photo-thermal materials, which then transform the light energy into heat energy and deliver it to LCEs for driving. Moreover, various photo-thermal materials can be added to LCEs to improve their mechanical qualities [38].

References

1. F. Reinitzer, Beiträge zur Kenntniss des Cholesterins. *Monatsh. Chem.* **1888**, 9, 421-441.
2. De Gennes, P. G.; Prost, J. The Physics of Liquid Crystals. *Oxford: Clarendon Press.* **1993**.
3. Hird, M.; Collings, P. J. Introduction to liquid crystals chemistry and physics. *Taylor & Francis,* **1997**.
4. Dierking, I. Textures of liquid crystals. *John Wiley & Sons*, **2003**.
5. Varghese, S.; Crawford, G. P.; Bastiaansen, C. W. M.; de Boer, D. K. G.; Broer, D. J. Microrubbing technique to produce high pretilt multidomain liquid crystal alignment. *Appl. Phys. Lett.* **2004**, 85, 230–232.
6. Honma, M.; Nose, T. Twisted nematic liquid crystal polarization grating with the handedness conservation of a circularly polarized state. *Opt. Express.* **2012**, 20, 18449–18458.
7. Lee, C. H.; Yoshida, H.; Miura, Y.; Fujii, A.; Ozaki, M. Local liquid crystal alignment on patterned micrograting structures photofabricated by two photon excitation direct laser writing. *Appl. Phys. Lett.* **2008**, 93, 173509.
8. He, Z.; Tan, G.; Chanda, D.; Wu, S. T. Novel liquid crystal photonic devices enabled by two-photon polymerization. *Opt. Express.* **2019**, 27, 11472–11491.
9. Park, S.; Padeste, C.; Schift, H.; Gobrecht, J.; Scharf, T. Chemical nanopatterns via nanoimprint lithography for simultaneous control over azimuthal and polar alignment of liquid crystals. *Adv. Mater.* **2005**, 17(11), 1398–1401.
10. Yi, Y.; Nakata, M.; Martin, A. R.; Clark, N. A. Alignment of liquid crystals by topographically patterned polymer films prepared by nanoimprint lithography. *Appl. Phys. Lett.* **2007**, 90, 163510.
11. Takahashi, H.; Sakamoto, T.; Okada, H. Liquid crystal device with 50 nm nanogroove structure fabricated by nanoimprint lithography. *J. Appl. Phys.* **2010**, 108, 113529.
12. Yaroshchuk, O.; Reznikov, Y. Photoalignment of liquid crystals: basics and current trends. *J. Mater. Chem.* **2012**, 22, 286–300.

13. Brake, J. M.; Mezera, A. D.; Abbott, N. L. Effect of surfactant structure on the orientation of liquid crystals at aqueousliquid crystal interfaces. *Langmuir* **2003**, 19(16), 6436-6442.
14. Lockwood, N. A.; De Pablo, J. J.; Abbott, N. L. Influence of surfactant tail branching and organization on the orientation of liquid crystals at aqueous-liquid crystal interfaces. *Langmuir* **2005**, 21(15), 6805-6814.
15. Ondris-Crawforde, R.; Boyko, E. P.; Wagner, B. G.; et al. Microscope textures of nematic droplets in polymer dispersed liquid crystals. *J. Appl. Phys.* **1991**, 69(9), 6380-6386.
16. Xu, F.; Kitzerow, H. S.; Crooker, P. P. Electric-field effects on nematic droplets with negative dielectric anisotropy. *Phys. Rev. A.* **1992**, 46(10), 6535.
17. Xu, F.; Kitzerow, H. S.; Crooker, P. P. Director configurations of nematic-liquid-crystal droplets: Negative dielectric anisotropy and parallel surface anchoring. *Phys. Rev. E.* **1994**, 49(4), 3061.
18. Erdmann, J. H.; Žumer, S.; Doane, J. W. Configuration transition in a nematic liquid crystal confined to a small spherical cavity. *Phys. Rev. Lett.* **1990**, 64(16), 1907.
19. Kurik, M.; Lavrentovich, O. Negative-positive monopole transitions in cholesteric liquid crystals. *JETP Lett*. **1982**, 35(9), 444-447.
20. Kitzerow, H. S. Polymer-dispersed liquid crystals from the nematic curvilinear aligned phase to ferroelectric films. *Liq. Cryst.* **1994**, 16(1), 1-31.
21. Volovik, G. E.; Lavrentovich, D. Topological dynamics of defects: Boojums in nematic drops. *Zh Eksp Teor Fiz.* **1983**.
22. Gupta, J.; Sivakumar, S.; Caruso, F.; et al. Size-Dependent Ordering of Liquid Crystals Observed in Polymeric Capsules with Micrometer and Smaller Diameters. *Angew. Chem. Int. Ed.* **2009**, 48(9), 1652-1655.
23. Finkelmann, H.; Kock, H. J.; Rehage, G. Liquid Crystalline Elastomers - A New Type of Liquid Crystalline Materia. Makromol. *Chem*. **1981**, 2(4), 317-322.
24. White, T. J.; Broer, D. J. Programmable and Adaptive Mechanics with Liquid Crystal Polymer Networks and Elastomers. *Nat. Mater.* **2015**, 14(11), 1087-98.

25. Ware, T. H.; McConney, M. E.; Wie, J. J.; Tondiglia, V. P.; White, T. J. Voxelated Liquid Crystal Elastomers. *Science*. **2015**, 347(6225), 982-4.
26. Ware, T. H.; White, T. J. Programmed Liquid Crystal Elastomers with Tunable Actuation Strain. *Polym. Chem.* **2015**, 6(26), 4835-4844.
27. Xia, Y.; Zhang, X.; Yang, S. Instant Locking of Molecular Ordering in Liquid Crystal Elastomers by Oxygen-Mediated Thi-ol-Acrylate Click Reactions. *Angew. Chem. Int. Ed. Engl.* **2018**, 57(20), 5665-5668.
28. Thomsen, D. L.; Keller, P.; Naciri, J.; Pink, R.; Jeon, H.; Shenoy, D.; Ratna, B. R. Liquid Crystal Elastomers with Mechanical Properties of a Muscle. *Macromolecules* **2001**, 34(17), 5868-5875.
29. Wu, G.; Jiang, Y.; Xu, D.; Tang, H.; Liang, X.; Li, G. Thermoresponsive Inverse Opal Films Fabricated with Liquid-crystal Elastomers and Nematic Liquid Crystals. *Langmuir* **2011**, 27, (4), 1505-1509.
30. Brannum, M. T.; Steele, A. M.; Venetos, M. C.; Korley, L. T. J.; Wnek, G. E.; White, T. J. Light Control with Liquid Crystalline Elastomers. *Adv. Opt. Mater.* **2019**, 7(6), 1801683.
31. Xing, H.; Li, J.; Guo, J.; Wei, J. Bio-Inspired Thermal-responsive Inverse Opal films with Dual Structural Colors Based on Liquid Crystal Elastomer. J. Mater. Chem. C 2015, 3, (17), 4424-4430.
32. Kim, S. U.; Lee, Y. J.; Liu, J.; Kim, D. S.; Wang, H.; Yang, S. Broadband and Pixelated Camouflage in Inflating Chiral Nematic Liquid Crystalline Elastomers. Nat. Mater. 2022, 21, (1), 41-46.
33. Shi, Y.; Zhu, C.; Li, J.; Wei, J.; Guo, J. A Color-Changing Plasmonic Actuator Based on Silver Nanoparticle Array/Liquid Crystalline Elastomer Nanocomposites. New J. Chem. 2016, 40, (9), 7311-7319.
34. Guo, Y.; Shahsavan, H.; Sitti, M. Microscale Polarization Color Pixels from Liquid Crystal Elastomers. Adv. Opt. Mater. 2020, 8, (17).
35. Zhang, Y. S.; Jiang, S. A.; Lin, J. D.; Yang, P. C.; Lee, C. R. Stretchable Freestanding Films of 3D Nanocrystalline Blue Phase Elastomer and Their Tunable Applications. Adv. Opt. Mater. 2020, 9, (1).

36. Xing, H.; Li, J.; Shi, Y.; Guo, J.; Wei, J. Thermally Driven Photonic Actuator Based on Silica Opal Photonic Crystal with Liquid Crystal Elastomer. ACS Appl. Mater. Interfaces 2016, 8, (14), 9440-5.
37. Akamatsu, N.; Hisano, K.; Tatsumi, R.; Aizawa, M.; Barrett, C. J.; Shishido, A. Thermo-, Photo-, and Mechano-Responsive Liquid Crystal Networks Enable Tunable Photonic Crystals. Soft Matter 2017, 13, (41), 7486-7491.
38. Wei, W.; Zhang, Z.; Wei, J.; Li, X.; Guo, J. Phototriggered Selective Actuation and Self-Oscillating in Dual-Phase Liquid Crystal Photonic Actuators. *Adv. Opt. Mater.* **2018**, 6(15), 1800131.

Chapter 3 Background to the development of the Existing Liquid Crystal Sensors

In the past decade, the application of liquid crystal has developed fast. The application fields are not limited to the electro-optic response, such as in displays, optical shutters or light modulators anymore. There is a field full of potential now coming into public view, that is various kinds of sensors. The most critical point is the sensitive response of liquid crystal to simulations from an external environment, such as temperature [1-16], humidity [17-18], mechanical stimulus [19-24], gas [25-37], chemical ions [38-46], biomolecules [47-64] and so on. This thesis is concerned with the application of liquid crystals to different sensors. This chapter provides a background and context to the work that is reported in the thesis through the lots of literature review.

3.1 Environmental sensors

3.1.1 Thermal sensors

Thermal sensors were the earliest kind where liquid crystals were employed and had undergone a lot of changes over the years. With the efforts of researchers, the design of thermal sensor is more varied and comprehensive. Moreira *et al.* reported the temperature dependence of an optical fiber sensor. A chiral nematic liquid-crystal laser was coupled to an optical fiber. When the temperature is varied, there are unexpected wavelength oscillations in the laser emission, which can be explained by the competition between bulk and surface anchoring torques [1]. Besides, Wolinski *et al.* demonstrated a method of optical fiber sensing with wide sensitivity and operating regions by using different combinations of photonic crystal fibers and liquid crystals [2]. If a different type of hybrid photonic crystal fibres, liquid crystal infiltrated photonic crystal fibres, were utilized in the temperature sensing, an efficient thermo-optic fibre switch can be achieved [3]. Marcos *et al.* fulfilled the use of liquid

crystals to sense shear and temperature fields later [4]. Hu *et al.* demonstrated a linearly, repeatable and sensitive temperature sensor, which was achieving by filling the nematic liquid crystal 6CHBT into a single void within a photonic crystal fiber structure. It could detect the temperature through the resonance wavelength from 44°C to 53°C with a sensitivity around 3.90 nm/°C, which conducting the mode properties in theoretical and proving the coupling principle [5]. A battery-free autonomous and constantly working radio frequency identification (RFID) temperature sensor was proposed by Shafiq *et al.* This sensor utilized reversible actuators based on the shape morphing cold-temperature reactive liquid crystal elastomers, which can detect temperature threshold crossings for several (room-to-cold and cold-to-room) temperature cycles [6].

Some researchers tend to combine the fiber with the liquid crystal to detect the changing temperature [7-16]. There is frequently a direct phase transition between an optically scattering smectic or chiral nematic mesophase and the transparent isotropic phase in liquid crystal systems. Together with the qualities of low loss optical fibers, this innovative property of liquid crystal devices forms the cornerstone of a precise optical temperature switch [7]. It was stated that an optical fiber temperature sensor has been modified by covering the tip of the fiber with a thermochromic liquid crystal (TLC) film. From 28 °C to 46 °C, the TLC sensor indicates a reversible wavelength change of the reflective light peak [8]. Lu et al. proposed a photonic crystal fiber (PCF) surface plasmon resonance (SPR) based temperature sensor, which was composed of a photonic crystal fiber and different concentrations of analyte and silver nanowires. As the temperature increases, a blue shift occurs, and the concentration changes the resonance wavelength and confinement loss. It can reach the selectivity of 2.7 nm/°C, which was analyzed by numerical simulations and experimental demonstration [9]. A temperature response of LC-filled photonic crystal fiber was evidenced in detail by Sun *et al.* Depending on the temperature response

at different temperature ranges, the photonic band gap can be high-tuned with a sensitivity of 105 nm/°C around the liquid crystal's clearing point temperature [10]. Hameed *et al.* reported a novel SPR temperature sensor based on photonic crystal fiber with nematic liquid crystal core. The ordinary and extraordinary refractive indices of the nematic liquid crystal material will be affected by temperature changes, leading to a resonance wavelength peak shift, so a temperature change may be detected by observing the peak shift [11]. What is more, Du *et al.* further optimized the theoretical simulation for a better performance in the narrow full width at half maximum and sensitivity from 15 °C to 85 °C, which is superior to previous optical fibers infiltrated by LC material [12]. Compared to the conventional one-dimensional photonic crystal structures and photonic crystals fibers, a unique temperature sensor based on one-dimensional annular photonic crystals presented a higher sensitivity with 0.224 nm/°C [13].

There is another design of thermal-sensor that combining circuit and liquid crystal [14-16]. A wireless temperature sensor based on the capacitance of an LC cell is suggested by Torres *et al.* This prototype is intended to be the seed of a wearable temperature sensor for biomedical monitoring [14]. According to Jing's work, the sensing performance of the capacitive-type liquid crystal temperature sensor was investigated using the impact of liquid crystal thermal sensitivity on the capacitance of a liquid crystal cell. It provides a theoretical framework for future study and development of low-power electronic devices [15]. Aigorri *et al.* also investigated a highly improved temperature sensor composed of three electrodes, which refers to the possibility of incorporating this sensor with other LC devices [16].

3.1.2 Humidity sensors

In recent study, liquid crystals have been used to sense the environmental humidity. A humidity sensor based on printable chiral nematic liquid crystal has been developed. It was made by printing an H-bonded chiral nematic liquid

crystal polymer film and converting it into a hygroscopic polymer salt film. As a consequence, by altering the reflection colour between green and yellow, a fast-responding temperature and humidity sensor was obtained [17]. Hernandez *et al.* proposed a sensor probe film by depositing alternating layers of Poly (allylamine hydrochloride) (PAH) and silica nanoparticles on the cleaved tip of an optical fiber coupler. Because of the quick reaction time, fluctuations in humidity in individual breaths may be addressed. The designed sensor offers a sensitive, small, and quick technique of detecting humidity [18].

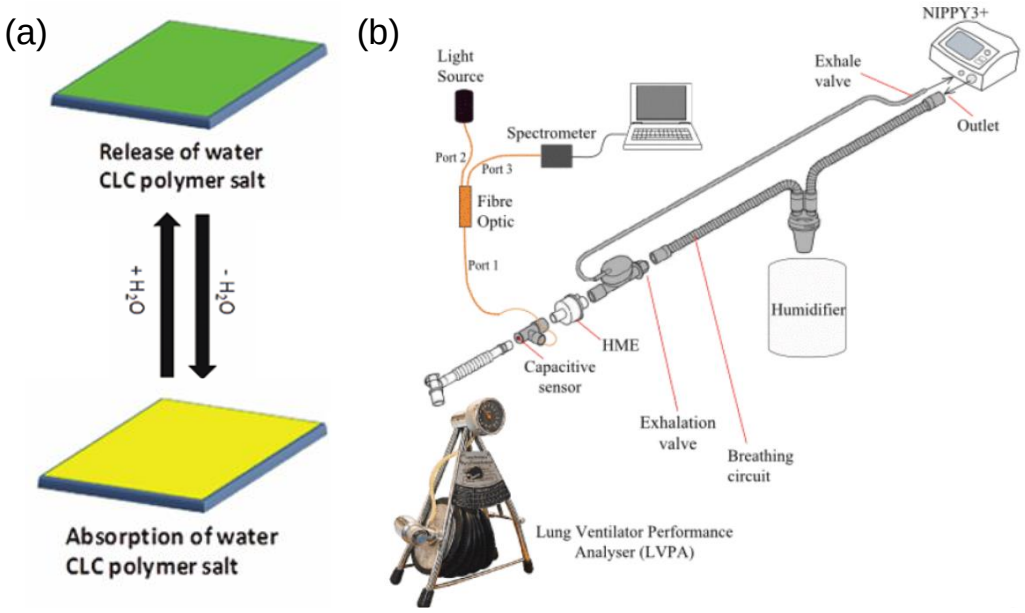

Figure 3.1 (a) Schematic representation of the humidity sensor [17]; (b) Experimental setup to measure the humidity level inside a breathing circuit connected to the ventilator [18].

3.1.3 Mechanical stimulus sensors

Mechanical stimulus is also an important field of the environmental sensing. Chatterjee and Anna examined the influence of shear fields on defects in LCs [19]. Feng *et al.* suggested a photoelastic pressure sensor based on a liquid crystal tunable fiber polarizer. As a tunable birefringent cladding of the fibre, a low-index LC is utilized. Thus, a 0.25 rad/N sensitivity pressure sensor is exhibited [20]. Kim *et al.* proposed a sensor, made up of a liquid crystal capacitor and a sensing circuit made up of amorphous silicon thin film

transistors (a-Si TFTs). The sensing circuit in the pixel converts the change in sensor capacitance when the sensor is touched into a change in current [21]. Lai *et al.* investigated a novel 4 × 4 pressure sensing array with tunable sensing ranges. The resistive sensing material is carbon nanotubes (CNTs) distributed in nematic liquid crystals (LC) composite. By adjusting the frequency of the driving voltage provided by the array scanning circuitry, the force sensing ranges may be modified [22]. Picot *et al.* reported a rather highly cross-linked chiral nematic LCE is applied in the real-time optical strain sensor [23]. The sensor comprises of a spray-coated, crosslinked cholesteric liquid crystal layer on a polyamide 6 substrate that is uniaxially orientated. According to Mistry's work, when mechanically strained, acrylate-based isotropic LCE display a classical isotropic rubber response with high strain-optic coefficients and high compliances [24]. But it can only distinguish the magnitude of the force by the different kinds of colors, which is not sensitive enough.

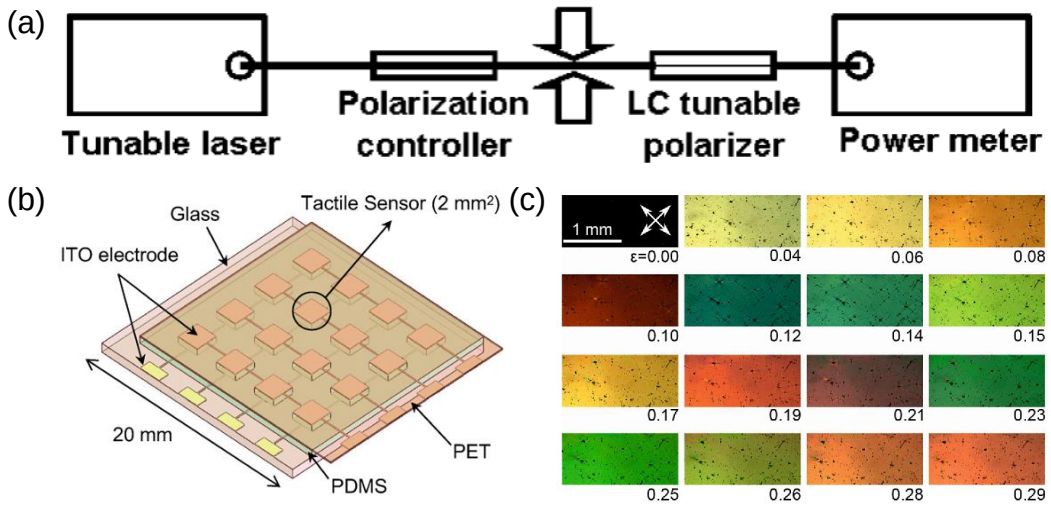

Figure 3.2 (a) Experimental setup to demonstrate the LC tunable fiber polarizer and pressure sensor [20]; (b) the schematic of the sensing array with the tunable sensing range [22]; (c) Strain-induced birefringence colors for LCE as seen via crossed polarizers [24].

3.2 Chemical vapor sensors

At concentrations as low as a few parts per million, liquid crystal sensors can detect the presence of pollutants, chemical warfare agents, and other vapor-

phase toxins. To be helpful, LC sensors must activate quickly and selectively in the presence of target analytes.

Some LC sensors are made up of a thin LC film that is placed on a reactive substrate. One of the first attempts to use LCs as detectors of volatile organic compounds (VOCs) is described by Poziomek *et al.* in 1974. In this work a nematic-isotropic transition was used as an indicator of VOC exposure [25]. In [26], the discotic liquid crystals based on phthalocyanines were used to detect low concentration of nitrogen oxide. From the work of Shah *et al.*, a system providing parts-per-billion (by volume) sensitivity to either organoamine or organophosphorus compounds was investigated [27]. The targeted analyte diffuses quickly from the environment to the surface-immobilized receptor through the micrometer-thick liquid crystal layer (on the order of seconds), which has potential of wearable personalized sensors for real-time measurement. There is a chiral nematic liquid crystal film coated side polished fiber demonstrated by Tang *et al.* that can detect the VOC (volatile organic compounds) gas, tetrahydrofuran, acetone and methanol gas, for example [28]. The work demonstrates how to embed the sensitive liquid crystal onto the fiber for the construction of liquid-crystal-based fiber sensors. For some latest research, the impact of liquid crystal sensor material parameters on sensor activation times for typical air contaminants is quantified using molecular simulations. It suggested that by estimating the influence of LC composition on analyte transport, molecular simulations can be utilized to select LC materials for increased sensor selectivity. Altering the composition of the LC film can change activation timings to identify activation by various analytes based on estimations of analyte permeances and corresponding transport timescales [29].

The reflection band in chiral nematic materials also offers a lot of information that can be applied to sensing when exposed to a target gas environment. Functionalized cholesterol derivatives forming chiral nematic films with a selective reflection band in a visible part of the spectrum were

studied by Kirchner *et al.* as promising sensors for detecting amine vapors. The absorption of VOCs resulted in a spectral shift of the selective reflection band position [30]. Kek *et al.* evidenced the relationship between the chiral nematic liquid crystal's molecular structures and the shift in their reflection spectrum caused by contact with volatile organic molecules [31]. The mechanism to explain why the peak wavelength shifts red or blue when contacting with VOC vapor was put forward. The selective reflection band 's position changing of chiral nematic liquid crystal in gas environmental exposure were further explored in [32]. When different analyte vapours are incorporated into CLC layers, the pitch length is disrupted, changing the optical characteristics and moving the absorption band.

Combining the liquid crystal with other materials is also a useful method for gas sensing. Chiral nematic liquid crystals are employed as sensitive coatings for both polar and non-polar compounds to detect organic solvent vapours [33]. The insertion of various analyte vapours in the CLC layers alters the pitch length, which modifies the optical characteristics, i.e., shifting the absorption band [33]. Sutarlie *et al.* used chiral nematic liquid crystals doped with dodecylamine to detect aldehyde vapors [34]. A chemical reaction between amine and aldehyde groups was the main detecting technique. Aksimentyeva *et al.* reported a new method for creating an active medium for optical gas sensors for carbon monoxide detection based on a liquid crystal doped with iron compounds [35]. In this primary transducer of a carbon monoxide sensor, the chiral nematic liquid crystal CLC-2103L was doped with Fe_3O_4 magnetite nanoparticles at a concentration of 0.30-0.67%. Another example is an optical sensor based on a mixture of chiral nematic liquid crystal BLO-62 and nematic 5CB as a sensitive medium for the detection of acetone vapor that has been proposed by Ivakha's group [36].

The nanotechnology platform based on liquid crystals and targeted to detection of biological threats and toxic gases is a growing field. For example, a sensing film consisting of a polymer-dispersed liquid crystal (PDLC) doped

with carbon nanotubes (CNT) for acetone detection was reported by Lai *et al.* in [37]. The orientational ordering transitions of the CNT and LC generate variations in the electrical resistance of the sensing film, which can be exploited to detect chemical gas. The sensor has a linear response range of 100 to 1500 ppm and a reaction time of less than 32 seconds.

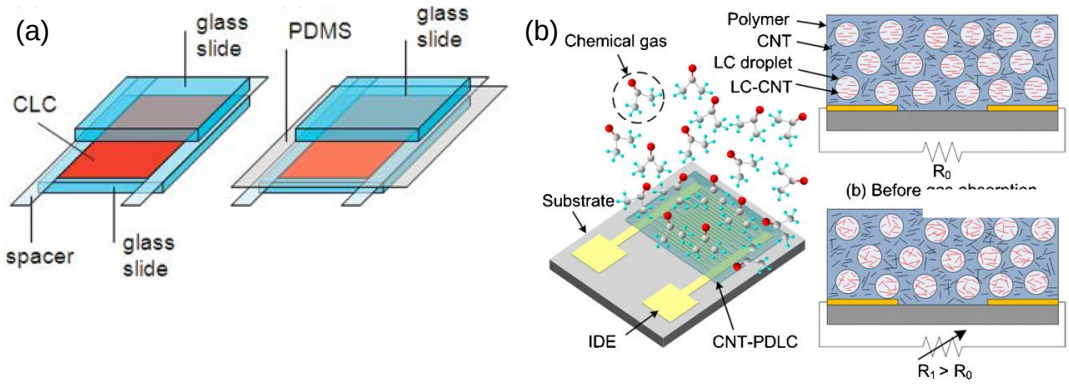

Figure 3.3 (a) Configurations of CLC-based gas sensors [34]; (b) Schematic diagram of the CNT-PDLC chemical sensing device and the sensor reactions when the CNT-PDLC material absorbs chemical gas [37].

3.3 Ion and chemical detection sensors

Ions detection is also an important field for liquid crystal sensing. Yang *et al.* postulated that the competing binding of 5CB and DMMP to the cations of metal perchlorate salts causes the orientational response of 5CB to DMMP [38]. This system can tell the metal ions with high electron affinities (>15.64 eV) (Cu^{2+}, Zn^{2+}, Cd^{2+}, Ni^{2+}, Co^{2+}, La^{3+}, Al^{3+}, Eu^{3+}, Fe^{3+}, etc.) from that with low electron affinities (Mn^{2+}, Mg^{2+}, Ag^{+}, Cs^{+}, Na^{+}, etc.). By preparing surfaces from perchlorate salts of aluminum(III), zinc(II) and iron(III), it was possible to distinguish between chemical warfare agents sarin (GB), VX and either soman (GD) or tabun (GA), proving the viability of designing surfaces patterned with metal salts to detect and positively identify chemical warfare agents [39]. A high spatial resolution sensor used to accurately monitor the presence of enzyme inhibitors such as heavy metal ions in real-time was reported by Jang's group. When urea was in contact with the copper nitrate hydrate-

blocked urease, the optical appearance of the LC did not alter. A bright-to-dark change in the optical signal was regenerated after the copper-inhibited urease was reactivated by EDTA, showing an orientational transition of the LC [40].

For some specific ions, there are also many designs of LC-based sensors. The presence of organophosphonate compounds can be detected using orientational transitions of thin films of the smectic liquid crystal (8CB) on surfaces presenting copper ions [41].

Lead ions (Pb^{2+}) can be detected by a liquid crystal droplet pattern-based sensor in a phosphate buffer saline (PBS) solution. A planar-to-homeotropic order transition of LC droplets was triggered during the single-stranded DNAzyme's working process [42]. There is another liquid crystal optical sensor for detection of Pb^{2+} based on DNAzyme and its combined strand. The ordered and disordered liquid crystal configurations, generated separately by complementary DNA strand and catalytically cleaved DNA in the presence of lead ion, result in dark and bright optical images under POM [43].

As for the detection of mercury ions (Hg^{2+}), a simple liquid crystal droplet sensor can be formed with trimethyl octadecyl ammonium bromide (OTAB) and an Hg^{2+}-binding aptamer [44]. 5CB doped with a sulfur- and nitrogen-containing ligand 5-(pyridine-4-yl)-2-(5-(pyridin-4-yl)thiophen-2-yl)thiazole (ZT) can also be rearded as the Hg^{2+} specific LCs in aqueous solutions [45]. If doped a newly synthesized amphiphilic potassium N-methyl-N-dodecyldithiocarbamate (MeDTC) into the 5CB, a label-free and real time detection method for mercuric ions (Hg^{2+}) can also be realized. A dark to bright change of the polarization image of LCs was seen when this sensor system was incubated in an aqueous solution containing Hg^{2+} ions [46].

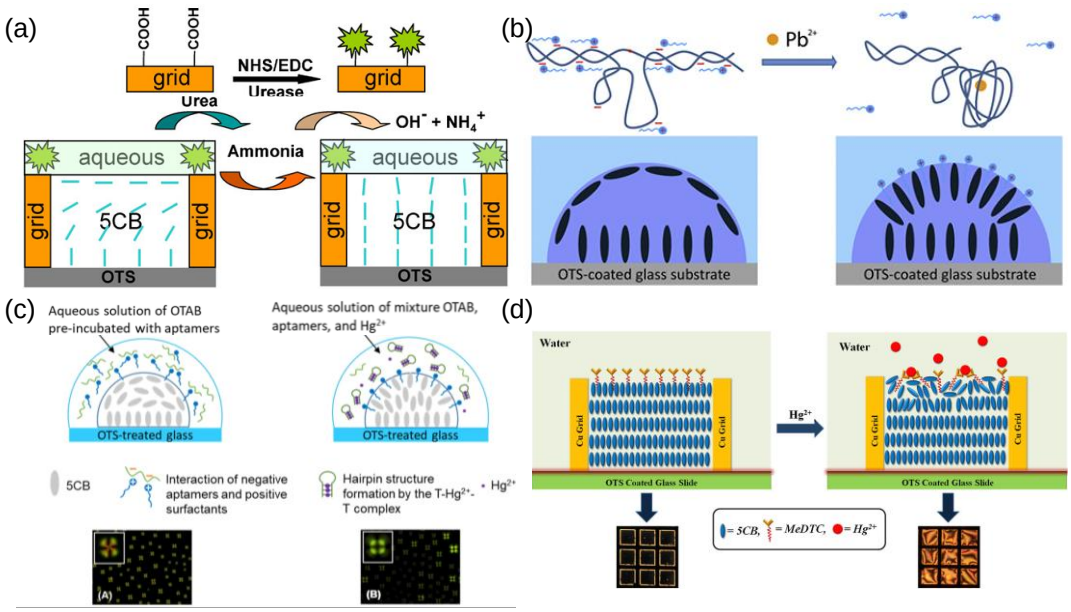

Figure 3.4 (a) Procedures used for urease immobilization and schematic illustration of the orientational transition of UV-treated 5CB after adding urea to the optical cell [40]; (b) Schematic illustration of the LC orientational transition after introducing Pb^{2+} for the lead ion sensors [42]; (c) Schematic illustration of the liquid crystal (LC)-based droplet sensor showing the optical responses resulting from transitioning of the LC orientation induced by the Hg^{2+}-mediated formation of the hairpin structure [44]; (d) Schematic illustration of orientational transitions of 5CB molecules doped with MeDTC at LC/aqueous interface in the absence and presence of Hg^{2+} ions [46].

3.4 Biomolecular sensors

Compared to traditional approaches for biomolecular sensing, LC-based sensors have potential advantages since they don't need sophisticated apparatus or labels (enzymatic or fluorescent). The coupling between the aliphatic tails of the adsorbed amphiphiles and the mesogens of the LCs can lead to some changes in orientational order [47-48]. The amphiphiles' structure (e.g., tail length or head group structure) [49-50] as well as chemical or physical processes in the aqueous phase that disturb or perturb these assemblies (e.g., binding or enzymatic action of a protein) [47, 51-52] affect the form and extent of these changes. In recent studies, the inclusion of lipids [53-56], surfactants [49-50, 58], proteins [51-52, 59], and viruses [60-61] can trigger the orientational ordering transitions in LC have been investigated. For example, Birchall *et al.* reported a system to detect and distinguish between

different proteases, which was the first time to combine solid-phase synthesis (SPS) and liquid crystal display (LCD) [62]. As for the detection of the glucose, there are also several methods. Proton sensitive glucose sensors employing classical 4-cyano-4-pentylbiphenyl (5CB) material were successfully tested by Khan *et al.* in [63]. A new and sensitive LC-droplet-based glucose biosensor was proposed by Kim *et al.* in [64]. This functionalized liquid crystal droplet's configuration could change from radial to bipolar when identifying glucose at concentration as low as 0.03 mM. Sivakumar *et al.* demonstrated a way for the development of a new class of LC microdroplet-based biological sensors that can distinguish between types of bacteria and viruses based on their cell-wall/envelope structure [48]. When Gram-negative bacteria (E. coli) and lipid-enveloped viruses (A/NWS/Tokyo/67) come into contact with 5CB, it's structure changes from bipolar to radial.

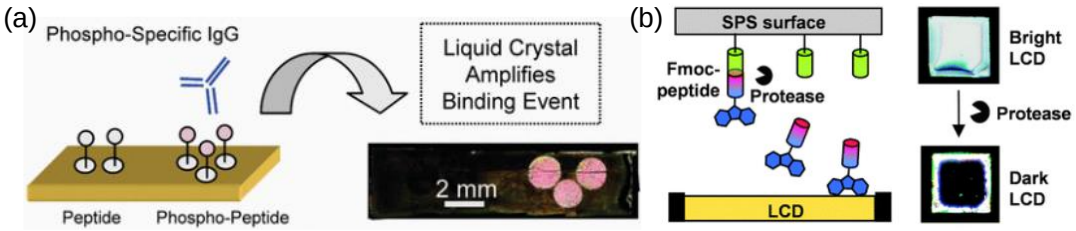

Figure 3.5 (a) Schematic illustrations that demonstrate the use of liquid crystals to amplify and report specific protein-peptide binding events occurring at interfaces [58]; (b) Schematic representation of the sensor chamber in our combined SPS–LCD protease sensor [62].

3.5 Summary

In this chapter, it is clear that many research groups have been devoted to developing LC-based biosensors over the past decades. LCs are employed as the sensor elements since very early times, and it has become more diverse in application and implementation methods after years' improvements. However, there still have a lot of potential to be explored in LC-based sensors, such as through combining with other novel functional materials. In order to explore the potential of liquid crystal in biosensors, the following projects are

carried out.

References

1. Moreira, M. F.; Carvalho, I. C. S.; Cao, W.; Bailey, C.; Taheri, B.; Palffy-Muhoray, P. Cholesteric liquid-crystal laser as an optic fiber-based temperature sensor. *Appl. Phys. Lett.* **2004**, 85(14), 2691-2693.
2. Wolinski, T. R.; Czapla, A.; Ertman, S.; Tefelska, M.; Domanski, A. W.; Wojcik, J.; Nowinowski-Kruszelnicki, E.; Dabrowski, R. Photonic Liquid Crystal Fibers for Sensing Applications, *IEEE Trans. Instrum. Meas.* **2003**, 57, 1796 – 1802.
3. Larsen, T. T.; Broeng, J.; Hermann, D. S.; Bjarklev, A. Thermo-optic switching in liquid crystal infiltrated photonic bandgap fibres. Electron. Lett. 2003, 39, 1719-2.
4. Marcos, C.; Pena, J. M. S.; Torres, J. C.; Santos, J. I. Temperature-Frequency Converter Using a Liquid Crystal Cell as a Sensing Element. *Sensors* **2012**, 12(3), 3204-3214.
5. Hu, D. J. J.; Lim, J. L.; Cui, Y.; Milenko, K.; Yixin Wang; Shum, P. P.; Wolinski, T. Fabrication and Characterization of a Highly Temperature Sensitive Device Based on Nematic Liquid Crystal-Filled Photonic Crystal Fiber. *IEEE Photonics Journal* **2012**, 4(5),1248-1255.
6. Shafiq, Y.; Henricks, J.; Ambulo, C. P.; Ware, T. H.; Georgakopoulos, S. V. A Passive RFID Temperature Sensing Antenna with Liquid Crystal Elastomer Switching. *IEEE Access* **2020**, 8, 24443-24456.
7. Coles, H. J.; Bone, E. L.; Bowdler, A. R.; Gleeson, H. F. A fibre optic liquid crystal temperature switch, *SPIE Conference Proceedings* **1998**, 949, 185-190.
8. He, C.; Korposh, S.; Correia, R.; Hayes-Gill, B. R.; Morgan, S. P.Optical fibre temperature sensor based on thermochromic liquid crystal. *Seventh European Workshop on Optical Fibre Sensors* **2019**, 1119908
9. Lu, Y.; Wang, M. T.; Hao, C. J.; Zhao, Z. Q.; Yao, J. Q. Temperature Sensing Using Photonic Crystal Fiber Filled with Silver Nanowires and Liquid. *IEEE Photonics Journal* **2014**, 6(3), 1-7.

10. Bing, S.; Huang, Y.; Chao, W.; He, J.; Wang, Y. Ultra-sensitive temperature sensor based on liquid crystal infiltrated photonic crystal fibers. *Fifth Asia-Pacific Optical Sensors Conference* **2015**, 96551W.
11. Hameed, M.; Azab, M. Y.; Heikal, A. M.; El-Hefnawy, S. M.; Obayya, S. Highly Sensitive Plasmonic Photonic Crystal Temperature Sensor Filled with Liquid Crystal. *IEEE Photonics Technol. Lett.* **2016**, 28(1), 59-62.
12. Du, C.; Wang, Q.; Zhao, Y. Electrically tunable long period gratings temperature sensor based on liquid crystal infiltrated photonic crystal fibers. *Sens. Actuators, A* **2018**, 278, 78-84.
13. Abadla, M. M.; Elsayed, H. A.; Mehaney, A. Sensitivity enhancement of annular one dimensional photonic crystals temperature sensors with nematic liquid crystals. Phys. Scr. **2020**, 95(8), 085508.
14. Torres, J. C.; García-Cámara, B.; Pérez, I.; Urruchi, V.; Sánchez-Pena, J. M. Wireless Temperature Sensor Based on a Nematic Liquid Crystal Cell as Variable Capacitance. *Sensors* **2018**, 18(10), 3436.
15. Jing, S.; Gao, N.; Tang, Z. Y.; Wu, K. M.; Sun, J. J.; Cai, M. L.; Zhao, T. Z.; Yang, C. Y.; Xing, H. Y.; Ye, W. J.. Capacitive-type liquid crystal temperature sensor. *Liq. Cryst.* **2020**, 48(8), 1103-1110.
16. Algorri, J. F.; Lallana, P. C.; Urruchi, V.; Sanchez-Pena, J. M. Liquid crystal temperature sensor based on three electrodes and a high-resistivity layer. *IEEE Sensors J.* **2015**, 15(9), 5222-5227.
17. Herzer, N.; Guneysu, H.; Davies, D. J. D.; Yildirim, D.; Vaccaro, A. R.; Broer, D. J.; Bastiaansen, C. W. M.; Schennung, A. P. H. J. Printable optical sensors based on h-bonded supramolecular cholesteric liquid crystal networks. *J. Am. Chem. Soc.* 2012, 134(18), 7608-7611.
18. Hernandez, F. U.; Morgan, S. P.; Hayes-Gill, B. R.; Harvey, D.; Kinnear, W.; Norris, A.; Evans, d.; Hardman, J. G.; Korposh, S. Characterization and use of a fiber optic sensor based on pah/sio2 film for humidity sensing in ventilator care equipment. *IEEE Trans. Biomed. Eng.* **2016**, 63(9), 1985-1992.

19. Chatterjee, S.; Anna, S. L. Formation and ordering of topological defect arrays produced by dilatational strain and shear flow in smectic-a liquid crystals. *Phys. Rev. E* **2012**, 85(1 Pt 1), 011701.
20. Jing, F.; Yun, Z.; Li, S. S.; Lin, X. W.; Xu, F.; Lu, Y. Q. Fiber-optic pressure sensor based on tunable liquid crystal technology. *IEEE Photonics J.* **2010**, 2(3), 292-298.
21. Kim, C. S.; Kang, B. K.; Jung, J. H.; Lee, M. J.; Kim, H. B.; Oh, S. S.; Jang, S. H.; Lee, H. J.; Kastuyoshi, H.; Shin, J. K. Active matrix touch sensor perceiving liquid crystal capacitance with amorphous silicon thin film transistors. *Jpn. J. Appl. Phys.* **2010**, 49(3S), 03CC03.1-03CC03.4.
22. Lai, Y. T.; Chen, Y. M.; Liu, T.; Yang, Y. J. A tactile sensing array with tunable sensing ranges using liquid crystal and carbon nanotubes composites. *Sens. Actuators, A* **2012**, 177, 48-53.
23. Picot, O. T.; Dai, M.; Billoti, E.; Broer, D. J.; Peijs, T.; Bastiaansen, C. W. M. A real time optical strain sensor based on a cholesteric liquid crystal network. *RSC Advances* **2013**, 3, 18794-18798.
24. Mistry, D.; Nikkhou, M.; Raistrick, T.; Hussain, M.; Jull, E.; Baker, D. L.; Gleeson, H. F. Isotropic Liquid Crystal Elastomers as Exceptional Photoelastic Strain Sensors. *Macromolecules* **2020**, 53, 3709-3718.
25. Poziomek, E. J.; Novak, T. J.; Mackay, R. A. Use of liquid crystals as vapor detectors, *Mol. Cryst. Liq. Cryst.* **1974**, 27(1-2), 175–185.
26. Wright, J. D.; Roisin, P.; Rigby, G. P.; Nolte, R.; Cook, M. J.; Thorpe, S. C. Crowned and liquid-crystalline phthalocyanines as gas-sensor materials. *Sens. Actuators, B* **1993**, 13(1-3), 276-280.
27. Shah, R., R.; Abbott, N. L. Principles for measurement of chemical exposure based on recognition-driven anchoring transitions in liquid crystals. *Science* **2001**, 293(5533), 1296-1299.
28. Tang, J. Y.; Fang, J. B.; Liang, Y. L.; Zhang, B.; Luo, Y. H.; Liu, X. Y.; Li, Z. B.; Cai, X. J.; Xian, J. Q.; Lin, H.; Zhu, W. G.; Guan, H. Y.; Lu, H. H.; Zhang, J.; Yu, J. H.; Chen, Z. All-fiber-optic VOC gas sensor based on side-polished fiber wavelength selectively coupled with cholesteric liquid crystal film, *Sens. Actuators, B* **2018**, 273, 1816-1826.

29. Jonathan, K. S.; Jake I. G.; Manos M.; Reid C. V. L. Molecular simulations of analyte partitioning and diffusion in liquid crystal sensors. *Mol. Syst. Des. Eng.* **2020**, 5(1), 304-316.
30. Kirchner, N.; Zedler, L.; Mayerhöfer, T. G.; Mohr, G. J. Functional liquid crystal films selectively recognize amine vapours and simultaneously change their colour. *Chem. Commun.* **2006**, 14(14), 1512-1514.
31. Kek, K. J.; Lee, J.; Otono, Y.; Ishihara, S. Chemical gas sensors using chiral nematic liquid crystals and its applications, *J. Soc. Inf. Disp.* **2017**, 25(4-6), 366-373.
32. Mujahid, A.; Stathopulos, H.; Lieberzeit, P. A.; Dickert, F. L. Solvent vapour detection with cholesteric liquid crystals—optical and mass-sensitive evaluation of the sensor mechanism. *Sensors* **2010**, 10(5), 4887-4897.
33. Mujahid, A.; Stathopulos, H.; Lieberzeit, P. A.; Dickert, F. L. Solvent Vapour Detection with Cholesteric Liquid Crystals—Optical and Mass-Sensitive Evaluation of the Sensor Mechanism. *Sensors* **2010**, 10(5), 4887-4897.
34. Sutarlie, L.; Lim, J. Y.; Yang, K. L. Cholesteric liquid crystals doped with dodecylamine for detecting aldehyde vapors. *Anal. Chem.* **2011**, 83(13), 5253-5258.
35. Aksimentyeva, O.; Mykytyuk, Z.; Fechan, A.; Sushynskyy, O.; Tsizh, B. Cholesteric Liquid Crystal Doped by Nanosize Magnetite as an Active Medium of Optical Gas Sensor. *Mol. Cryst. Liq. Cryst.* **2014**, 589 (1), 83-89.
36. Mykytyuk, Z. M.; Kremer, I. P.; Ivakh, M.; Diskovskyi, I. S.; Khomyak, S. V. Optical sensor with liquid crystal sensitive element for monitoring acetone vapor during exhalation. *Mol. Cryst. Liq. Cryst.* **2021**, 721(4), 1-6.
37. Lai, Y. T.; Kuo, J. C.; Yang, Y. J. A novel gas sensor using polymer-dispersed liquid crystal doped with carbon nanotubes. *Sens. Actuators, A* **2014**, 215(1), 83-88.
38. Yang, K. L.; Cadwell, K.; Abbott, N. L. Mechanistic study of the anchoring behavior of liquid crystals supported on metal salts and their orientational responses to dimethyl methylphosphonate. *J. Phys. Chem. B* **2004**,108(52), 20180-20186.
39. Cadwell, K. D.; Lockwood, N. A.; Nellis, B. A.; Alf, M. E.; Willis, C.; Abbott, N. L. Detection of organophosphorous nerve agents using liquid crystals supported on chemically functionalized surfaces. *Sens. Actuators, B* **2008**, 128(1), 91-98.

40. Hu, Q. Z.; Jang, C. H. Liquid crystal-based sensors for the detection of heavy metals using surface-immobilized urease. *Colloids Surf. B* **2011**, 88(2), 622-626.
41. Yang, K. L.; Cadwell, K.; Abbott, N. L. Use of self-assembled monolayers, metal ions and smectic liquid crystals to detect organophosphonates. *Sens. Actuators, B* **2005**, 104(1), 50-56.
42. Duong, T.; Jang, C. H. A label-free liquid crystal droplet-based sensor used to detect lead ions using single-stranded DNAzyme. *Colloids Surf. A* **2020**, 604(9), 125304.
43. Niu, X. F.; Liu, Y. J.; Wang, F.; Luo, D. Highly sensitive and selective optical sensor for lead ion detection based on liquid crystal decorated with DNAzyme. *Opt. Express* **2019**, 27, 30421-30428.
44. Hong, P. T. K.; Yun, K.; Jang, C. H. Liquid Crystal-Based Droplet Sensor for the Detection of Hg(II) Ions Using an Aptamer as the Recognition Element. *BioChip J.* **2021**, 15(2), 152–161.
45. Chen, C. H.; Lin, Y. C.; Chang, H. H.; Lee, S. Y. Ligand-Doped Liquid Crystal Sensor System for Detecting Mercuric Ion in Aqueous Solutions. *Anal. Chem.* **2015**, 87(8), 4546–4551.
46. Singh, S. K.; Nandi, R.; Mishra, K.; Singh, H. K.; Singh, R. K.; Singh, B. Liquid crystal based sensor system for the real time detection of mercuric ions in water using amphiphilic dithiocarbamate. *Sens. Actuators, B* **2016**, 226, 381-387.
47. Gupta, V. K.; Skaife, J. J.; Dubrovsky, T. B.; Abbott, N. L. Optical Amplification of Ligand-Receptor Binding Using Liquid Crystals. *Science*, **1998**, 279, 2077-2080.
48. Sivakumar, S.; Wark, K. L.; Gupta, J. K.; Abbott, N. L.; Caruso, F. Liquid Crystal Emulsions as the Basis of Biological Sensors for the Optical Detection of Bacteria and Viruses. *Adv. Funct. Mater.* **2009**, 19(14), 2260-2265.
49. Brake, J. M.; Mezera, A. D.; Abbott, N. L. Effect of surfactant structure on the orientation of liquid crystals at aqueousliquid crystal interfaces. *Langmuir* **2003**, 19(16), 6436-6442.
50. Lockwood, N. A.; De Pablo, J. J.; Abbott, N. L. Influence of surfactant tail branching and organization on the orientation of liquid crystals at aqueous-liquid crystal interfaces. *Langmuir* **2005**, 21(15), 6805-6814.

51. Park, J. S.; Abbott, N. L. Ordering transitions in thermotropic liquid crystals induced by the interfacial assembly and enzymatic processing of oligopeptide amphiphiles. Adv. Mater. **2010**, 20(6), 1185-1190.
52. Brake, J. M.; Abbott, N. L. Coupling of the orientations of thermotropic liquid crystals to protein binding events at lipid-decorated interfaces. *Langmuir* **2007**, 23(16), 8497-8507.
53. Brake, J. M.; Daschner, M. K.; Luk, Y. Y.; Abbott, N. L. Biomolecular interactions at phospholipid-decoratedsurfaces of liquid crystals. *Science* **2003**, 302, 2094-2097.
54. Gupta, J. K.; Meli, M. V.; Teren, S.; Abbott, N. L. Elastic energy-driven phase separation of phospholipid monolayers at the nematic liquid-crystal-aqueous interface. *Phys. Rev. Lett.* **2008**, 100(4), 392-396.
55. Meli, M. V.; Lin, I. H.; Abbott, N. L. Preparation of microscopic and planar oil-water interfaces that are decorated with prescribed densities of insoluble amphiphiles. JACS **2008**, 130(13), 4326-4333.
56. Price, A. D.; Schwartz, D. K. Fatty-acid monolayers at the nematic/water interface: phases and liquid-crystal alignment. *J. Phys. Chem. B* **2007**, 111(5), 1007-1015.
57. Bao, P.; Paterson, D. A.; Harrison, P. L.; Miller, K.; Peyman, S.; Jones, J. C.; Sandoe, J. A. T.; Stephen D. Evans, S. D.; Bushby, R. J.; Gleeson, H. F. *Lab Chip*, **2019**, 19, 1082-1089.
58. Gupta, J. K.; Abbott, N. L. Principles for manipulation of the lateral organization of aqueous-soluble surface-active molecules at the liquid crystal-aqueous interface. *Langmuir* **2009**, 25(4), 2026-33.
59. Clare, B. H.; Abbott, N. L. Orientations of nematic liquid crystals on surfaces presenting controlled densities of peptides: amplification of protein-peptide binding events. *Langmuir* **2005**, 21(14), 6451-6461.
60. Jang, C. H.; Cheng, L. L.; Olsen, C. W.; Abbott, N. L. Anchoring of nematic liquid crystals on viruses with different envelope structures. *Nano Lett.* **2006**, 6(5), 1053-1058.

61. Espinoza, L. A. T.; Schumann, K. R.; Luk, Y. Y.; Israel, B. A.; Abbott, N. L. Orientational behavior of thermotropic liquid crystals on surfaces presenting electrostatically bound vesicular stomatitis virus. *Langmuir* **2004**, 20(6), 2375-2385.
62. Birchall, L. S.; Ulijn, R. V.; Webb, S. J. A combined SPS–LCD sensor for screening protease specificity. *Chem. Commun.* **2008**, 2008(25), 2861-2863.
63. Khan, M.; Park, S. Y. Liquid crystal-based proton sensitive glucose biosensor. *Anal. Chem.* **2014**, 86(3), 1493–1501.
64. Kim, J.; Khan, M.; Park, S. Y. Glucose Sensor using Liquid-Crystal Droplets Made by Microfluidics. *ACS Appl. Mater. Interfaces* **2013**, 5(24), 13135–13139.

Chapter 4 Materials, experiments and technology methods

In this chapter, functional materials used throughout this thesis will be introduced, as will some of the general experimental and technical methods used.

4.1 Materials

Several materials including LC materials and non-LC materials were used in the following projects to explore the applications of liquid crystal in the field of biosensors. The nematic liquid crystal used in the later experiments is 5CB (4-pentyl-4'-cyanobiphenyl) due to its suitable transition temperature, accessibility and low cost. Chiral dopant applied in the following work are S1011 (HTP=40 μm^{-1}) and S811 (HTP=10.1 μm^{-1}). In the lipid coated droplet's observation, S1011 with a higher helical twisting power makes the pitches clear even in the small size of droplets. As for the UV induced droplets, the more important is the three-dimensional configuration of the inner liquid crystal molecules. S811 with a lower helical twisting power help the droplets present more clear changes of stripes under the same condition. Besides these basic liquid crystal materials, the functional materials with specific properties, azobenzene liquid crystals and aggregation induced emission materials are deserving an external introduction before the experiments.

4.1.1 Azobenzene liquid crystals

There are widespread applications of azobenzene-doped liquid crystals in several fields including holographic technology; photoactuators; and biosensing. Azobenzene compounds contain a conjugated π system and have strong absorption in the wavelength range from ultraviolet to visible red. They show a strong set of $\pi - \pi*$ transitions in the ultraviolet region and a weaker set of $n - \pi*$ transitions in the visible region [1-2]. For most azobenzene

compounds, the trans-isomer can be efficiently converted to the cis-isomer under UV irradiation conditions, while the cis-isomer can be completely reversibly converted to the trans-isomer under heating or visible light irradiation conditions. Azobenzene can be used as an optical trigger for the design and synthesis of a large variety of photoresponsive systems [3].

When azobenzene liquid crystals are mixed with normal nematic liquid crystals, the azobenzene liquid crystal molecules will follow the host molecules and align in the nematic phase. The isomerization of the azobenzene molecule causes it to change shape from elongated to bent, reducing the order parameter and disrupting the LC order. If the order of the aligned LC is disrupted sufficiently, there will be a phase change in the mixtures. When the azobenzene liquid crystal is stimulated by UV light after mixing and transforms into the isotropic state, the host liquid crystal is perturbed and has the opportunity to assume the isotropic state together [4].

We achieved a light-induced phase transition of the chiral nematic liquid crystal phase by doping with azobenzene liquid crystals (Azobenzene 1205, purchased from Beamco). Azobenzene 1205 is a mixture of liquid crystals that exists as nematic liquid crystal phase between 8°C and 59°C, while it has double bonds between the nitrogen atoms of the azobenzene molecules, which are very sensitive to light stimulation. The cis-state of the azobenzene liquid crystal is unstable and will revert to the trans-state when stimulated by thermal relaxation or long-wave (green) light. Therefore, it is possible to control the transition between the nematic liquid crystal and the isotropic state using UV and green light.

In this paper, azobenzene liquid crystals (azo-LC) are doped into CLC to study the characteristics of the light-driven phase transition in CLC droplets. The azo-LCs are generally nematic phase (trans-state) and can be transformed into the isotropic phase (cis-state) by stimulation with ultraviolet (UV) light [4]. Previous studies related to the photoisomerization in LC droplets including changing the surface energy and the chirality [5-6], but the

asymmetry of photoisomerization in droplets is not discussed in detail. Temperature-induced LC-isotropic phase transition is also asymmetrical [7]. The asymmetrical LC systems are in great potential while the case of symmetry breaking in LC droplets is only discussed in theory [8]. The particular characteristic of our experiment is the asymmetric introduction of a new interface in the droplets: isotropic-CLC (iso-CLC) interface. We find the iso-CLC interface can trigger changes of the internal structures of CLC droplets and finally results in different metastable topological architectures.

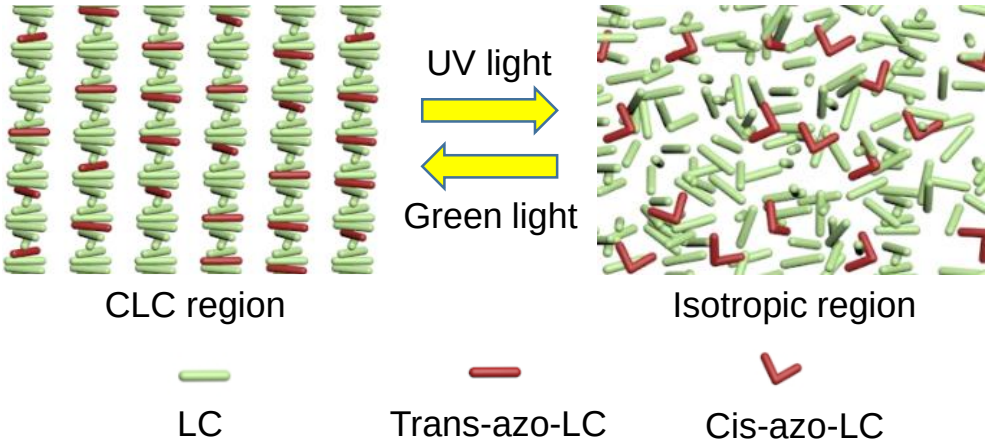

Figure 4.1 The phase transition of chiral nematic phase liquid crystals doped with azobenzene liquid crystals. Under UV stimulation the trans-state azobenzene liquid crystal molecules change to the cis-state and the liquid crystal system changes to an isotropic state, under green stimulation the cis-state azobenzene liquid crystal molecules revert to the trans-state and the liquid crystal system changes back to a chiral nematic phase liquid crystal.

Figure 4.1 is a schematic diagram of the phase transition of chiral nematic phase liquid crystals doped with azobenzene liquid crystals, the left diagram of chiral nematic phase liquid crystals doped with azobenzene liquid crystals is an ordered arrangement. In this situation, the trans azobenzene molecules do not affect the structural arrangement structure of the liquid crystal system. After irradiation with ultraviolet light, the structure of the azobenzene liquid crystal molecules changes to a bent conformation, disrupting the orderly arrangement of the liquid crystal system and producing a disordered arrangement which will form an isotropic state if the concentration of the

azobenzene components is large enough.

The details of azobenzene liquid crystals' performance and its significance in my project will be discussed in Chapter 6.

4.1.2 Aggregation-Induced emission materials

Fluorophore and chromophore components, which are responsible for the fluorescence or color of the molecule, respectively. As a result, several applications use the molecules containing those components as indicators. The main distinction between a fluorophore and a chromophore is that the former is a fluorescent chemical compound, whereas the latter is not. For more detail, a fluorophore is a fluorescent chemical molecule that, when excited by light, can emit light. Aggregation-Induced emission material is also a kind of fluorophore. Due to its ability of remitting, there are some applications include using as a dye or staining agent, as a substrate for enzymes, as a tracer in fluids, etc. Aggregation-Induced emission material is chosen in our later projects as a fluorophore to reflect the distribution and arrangement of liquid crystal molecules.

Aggregation-induced emission (AIE) is an opposite phenomenon of chromophore aggregation-caused quenching (ACQ) [9]. The configurations of AIEgens are highly twisted or propeller-shaped in space [10]. Due to the restriction of intramolecular rotation, they are highly emissive after aggregation formation [11]. The strong emissions in the aggregated state enable AIEgen-based supramolecular materials to have a promising prospect in the fields of luminescent materials [12], sensors [13], bioimaging [14], biology delivery [15], and theranostics [16-17]. The strong emissions of the AIEgens offer a characteristic of high sensitivity to some extent. Ding's group designed a new AIE probe (TPE-GFFYK(DEVDEE-Ac)), which had ultrahigh sensitivity toward detecting caspase-3 in water with limit of detection (LOD) of 0.54 pM [18].

Several research works have been reported that combine AIE materials

with liquid crystals, such as the work by Zhao who demonstrated light-emitting liquid crystal displays and reported their performance under electric field, based on an AIE luminogen obtained through synthesizing an AIE-LC material [19-21]. The AIE materials Zhao utilized is tetraphenylethylene-propylphenylethyne (TPE-PPE), which is also the AIE material we chose in the later works. It is expected that AIE luminogens will enable fluorescent LC based sensors and largely decrease the limit of detection in the probes, compared to previous naked-eye based LC sensors. Although research on the application of liquid crystal materials or the AIEgens to ion detection already exists, the combination of induced-aggregation emission and liquid crystals to achieve a lead ion detection method with high sensitivity, good selectivity, effectiveness, easy-reading and easy-operation has great application and application value.

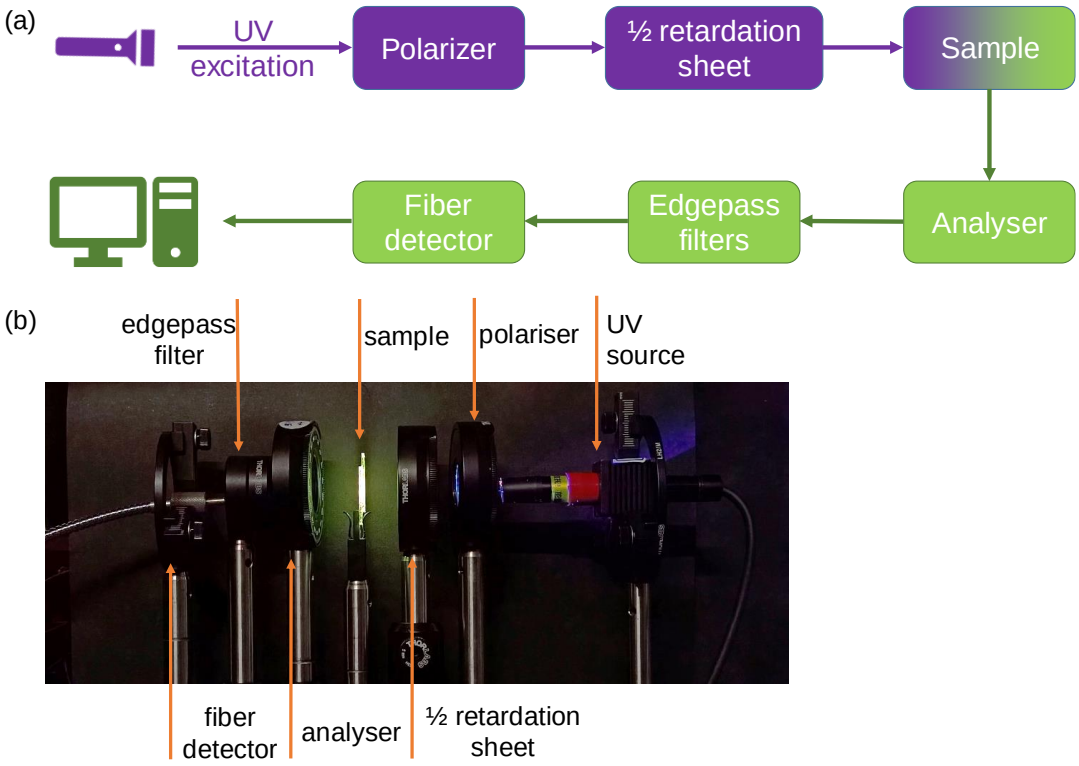

Figure 4.2 The experiment setting of the TPE-PPE's polarization analysis.

For the work on the TPE-PPE's polarization properties. As shown in

Figure 4.2 (a), the apparatus includes a collimated UV source (UVEC-4II, 365 nm), a polarizer, a $\lambda/2$ retardation sheet (working wavelength: 365 nm), an analyser, a longpass filter with a cut-on wavelength of 450 nm (FEL0450, Thorlabs Inc.), an optical fiber detector from a spectrometer (Avantes), and the spectrum analysis software (AvaSpec, Avantes B.V.) in the computer. The actual optical path and sample location are shown in Figure 4.2 (b). The sample should be put between the $\lambda/2$ retardation sheet and the analyzer. The UV light is incident vertically on a polarizing plate and turns into linearly polarized UV light. Then the modulated linearly polarized UV light is incident vertically on a $\lambda/2$ retardation sheet, and the intensity of the outgoing light remains unchanged. The polarization direction of the outgoing light is determined by the angle between the polarizer's polarization direction and the fast axis of the retardation sheet. When excited with a polarized UV light, the polarizer was put there as figure 4.2 shows. When excited with a non-polarized UV light, the polarizer was removed. As a result, a tunable polarization excitation system for the AIEgens was achieved.

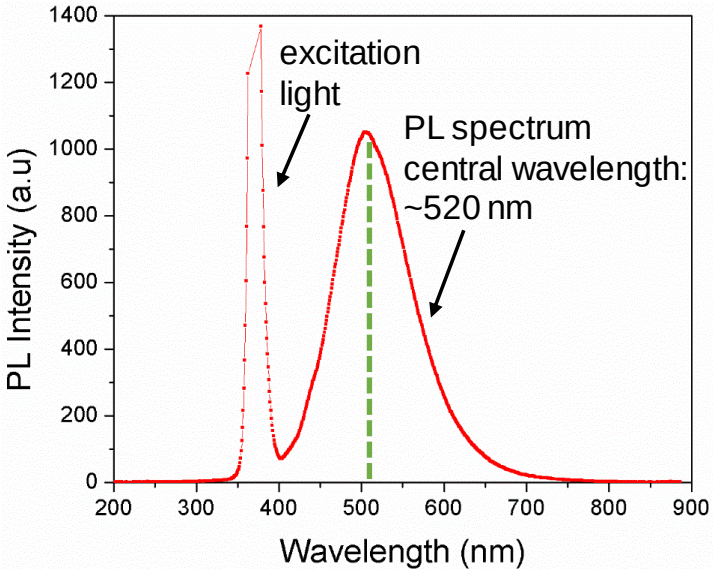

Figure 4.3 The photoluminescence (PL) spectra of TPE-PPE thin film. The first peak in this plot reflects the excitation wavelength, which is 365 nm. The second peak shows the fluorescence emission wavelength, which is around 520 nm.

When excited by the UV light with wavelength of 365 nm, the aggregation-induced luminescent molecules will show a strong fluorescence. As illustrated in Figure 4.3, the central wavelength of the PL spectrum is 520 nm, which is a yellow-green color.

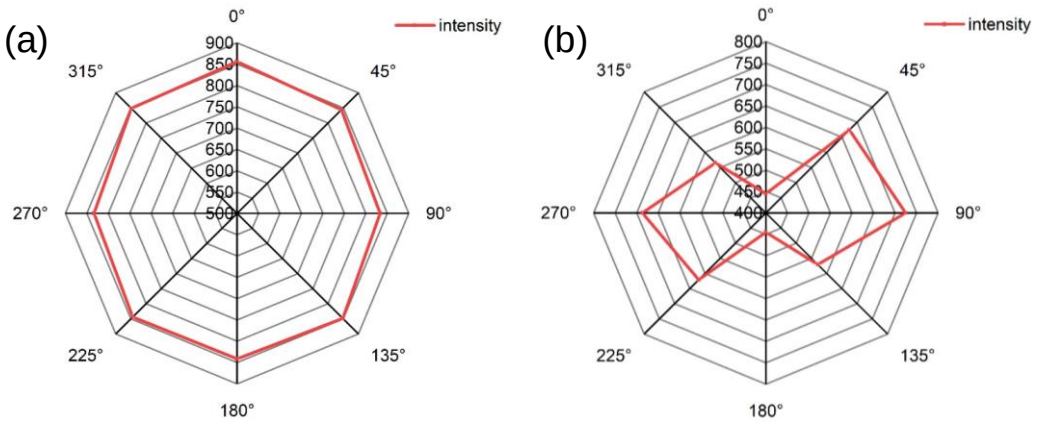

Figure 4.4 The polarization properties of (a) homeotropic TPE-PPE molecules and (b) homogeneous TPE-PPE molecules. The TPE-PPE molecules are filled into the glass cell for observation.

It can be seen that the TPE-PPE molecule in vertical alignment shows approximately equal fluorescence intensity in each direction (Figure 4.4 a). However, the TPE-PPE molecule in parallel alignment presents a distinct polarization dependence. The intensity that is perpendicular to the long axis is larger than that perpendicular to the short axis (Figure 4.4 b).

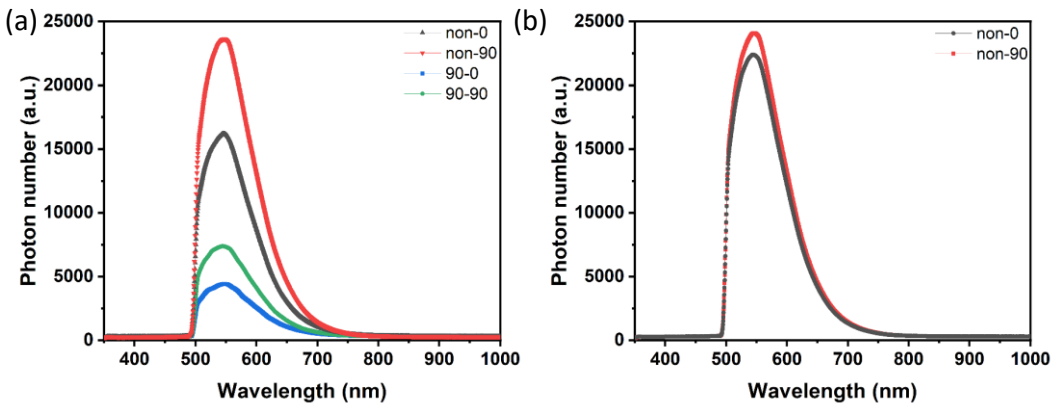

Figure 4.5 The fluorescence in the (a) parallel alignment sample and (b) vertical alignment sample. The labels “the presence or degree of the polarizer – the presence or degree of the analyzer” were shown in the top right corner of the plots. The black curve shows the 0° fluorescence excited by a non-polarized UV light. The red curve shows the 90° fluorescence excited by a non-polarized UV light. The blue curve shows the 0° fluorescence excited by a 0°-polarized UV light. The green curve shows the 90° fluorescence excited by a 90°-polarized UV light.

The TPE-PPE molecule in parallel alignment presents a distinct polarization dependence of its fluorescence (Figure 4.5 a). All these tests were excited by the UV source with the same condition (both the wavelength and the power). The fluorescence excited by non-polarized light is significantly higher than that excited by a polarized light. For the sample that excited by the same UV light condition, the 90° fluorescence is higher than 0° fluorescence ($I_{90^\circ} > I_{0^\circ}$). However, the TPE-PPE molecule in vertical alignment shows approximately equal fluorescence intensity in each direction (Figure 4.5 b). The 0° and 90°fluorescence excited by non-polarized UV light are nearly same. ($I_{90^\circ} = I_{0^\circ}$). For us, we usually observe the difference between the homeotropic state and the random state, or the changing between homogeneous state and the random state. So, we add the fluorescence of the TPE-PPE molecules in random into the comparison with the homeotropic and the homogeneous state, which can be seen in Figure 4.6.

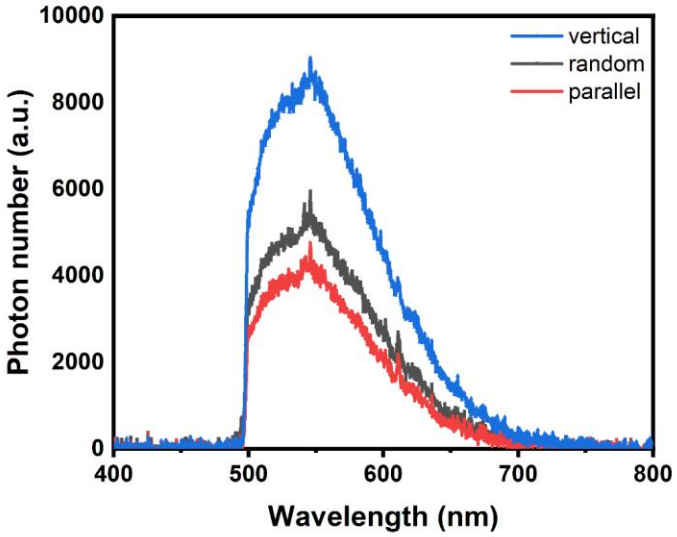

Figure 4.6 The comparison of the fluorescence among the TPE-PPE in vertical alignment (blue curve), the TPE-PPE in random alignment (black curve), and the TPE-PPE in parallel alignment (red curve).

The polarization property of the TPE-PPE is not related in the later experiment, so that its polarization dependence would not be discussed furthermore. The details of aggregation induced emission materials' performance and its significance in my project will be discussed in Chapter 7.

4.2 Differential scanning calorimetry

DSC is a thermo-analytical technique that measures the heat flow from the sample, allowing first order phase transitions to be determined from exo- or endo-thermic peaks. It does this by measuring the heat change associated with the molecule's thermal denaturation when heated at a constant rate. We use the differential scanning calorimeter (Q20 DSC with autosampler) to heat the materials from -20 ˚C to 70 ˚C and cool it back to -20 ˚C, and repeat this for three cycles. The speed of heating and cooling are both 10 ˚C /min. The accuracy for this Differential Scanning Calorimeter equipment is 0.01 ˚C (from the instrument manual of Q20 DSC). In this way, each mixtures' transition temperature between different phases can be obtained.

4.3 Photolithography

Photolithography is the technique of transferring a pattern from a mask plate to a substrate under the action of light with the aid of a photoresist. Photoresist is a photosensitive material whose properties change when exposed to light. Photoresist has positive and negative glue. For the substrate with positive photoresist, after exposure, the part receiving the light becomes easy to dissolve. After development, it is dissolved, leaving only the part not receiving the light to form the figure. On the contrary, for negative photoresist, after exposure, the part that receives the light will become insoluble, and after development, the part that leaves the light forms a pattern. The photoresist used in subsequent experiments is SU-8 negative photoresist, so the transparent area on the printed reflective mask is the channel part, and the opaque area is the non-channel part, as shown in Figure 4.7.

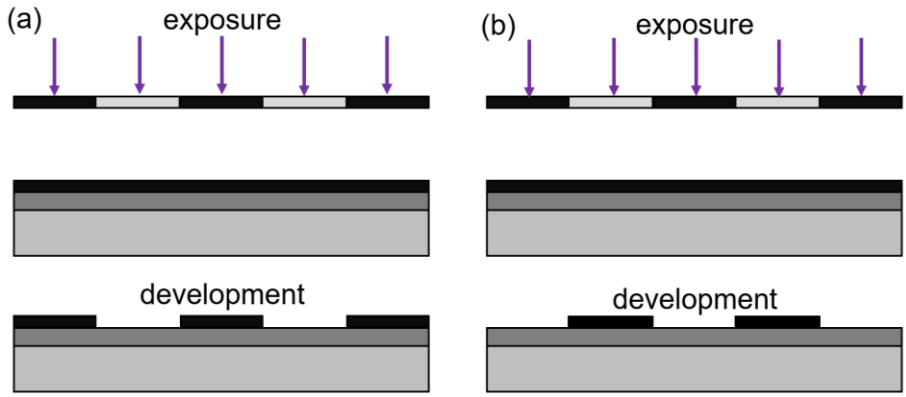

Figure 4.7 The two different kinds of photoresist
(a) positive photoresist; (b) negative photoresist.

A mask is made before the chip is made, which is used to mask certain areas during subsequent lithography, thereby transferring the design pattern to the photoresist. The lithography technique is mainly used to transfer the pattern on the mask onto the silicon wafer of SU-8 photoresist of certain thickness. The process of graphics transfer generally includes the following steps: pretreatment (wafer clean, pre-bake, primer vapor), photoresist coating, pre-bake, exposure, post-bake, development and hard bake.

The photolithography is used to create moulds for soft lithography fabrication of microfluidic devices, which are utilized to generate uniform droplets in the experiments of lipids coated liquid crystal droplets (Chapter 5) and UV induced liquid crystal droplets (Chapter 6).

4.4 Microfluidics

Microfluidics is a technology for the precise control and manipulation of microscale fluids, particularly submicron structures. It is also known as Lab-on-a-Chip or microfluidic chip technology. It is the integration of the basic units of sample preparation, reaction, separation and detection for biological, chemical and medical analysis into a micron-scale chip, which automates the entire process of analysis. Due to its great potential in the fields of biology, chemistry and medicine, it has developed into an emerging research field at the intersection of biology, chemistry, medicine, fluidics, electronics, materials and mechanics.

The elastic PDMS substrate for the microchannel of droplets generation was made by using the molding method after the mold of the chip was made. The basic principle of the molding method is to pour PDMS on the mold for curing, and then bond the PDMS substrates with glass to form a microfluidic chip. The specific process is shown in the Figure 4.8.

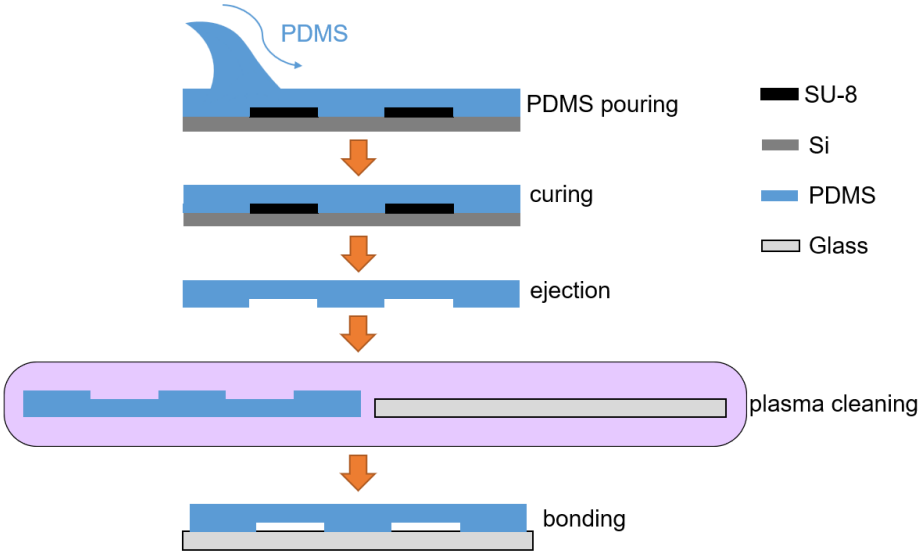

Figure 4.8 The process of PDMS chip making.

Before pouring PDMS, we would better put the silicon chip mold into the glass volatilization tank, drop 2~3 drops of chlorotrimethylsilane, cover the volatilization tank, and modify the volatilization for 3 min. The silane is used as an anti-adhesion layer for an easier delamination from the mould. After taking out the silicon wafer mold, put it into the petri dish, pour PDMS with thickness around 1 mm, bake at 80-150 ˚C. Then we can peel PDMS carefully.

In the process of bonding, there are some points where attention needs to be paid. First, the PDMS substrate and the glass substrate need to undergo ultrasonic cleaning in ethanol for 10 min. After drying, the glass substrate and the PDMS chip should be put in the plasma cleaner with the micro-channel side up. When fitting the PDMS chip and the glass substrate together, we use tweezers to press them gently. By this time, the PDMS chip have been sealing with the glass substrate irreversibly.

The microfluidics were utilized in the experiments related to the liquid crystal droplets, which is Chapter 5 and Chapter 6. The structures of the microfluidic chips are same, but the detail of the regulation methods will be elaborated in a number of ways to allow for different experiments in those two chapters. The design of the microfluidic chip is shown below (Figure 4.9). There are two inlets in this droplet formation device. The buffer will be injected

from the left entrance as the outer aqueous and divided into two side channels at the first conjunction. The CLC mixture was pumped into the chip through the middle entrance and wrapped by the buffer at the second conjunction. The droplets will be generated from the right outlet. The sizes of the generated droplets can be controlled by changing the flow speed of the buffer and the CLC mixture.

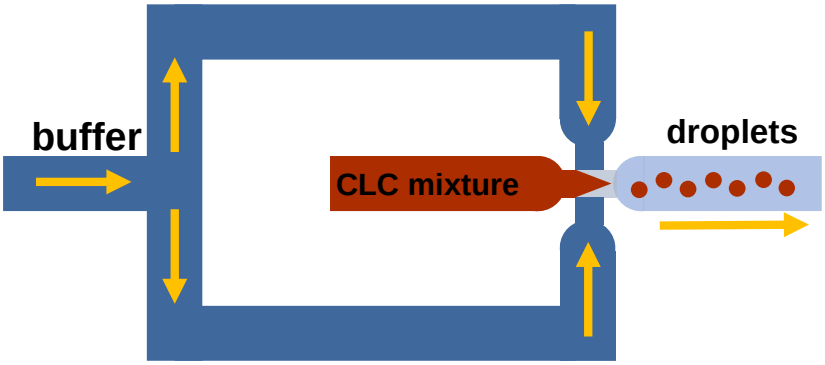

Figure 4.9 The design of microfluidic chip.

4.5 Other basic equipment

In this thesis, the polarized optical microscopy (Eclips Ti200, Nikon) was applied in the observation of the lipids coated droplets (Chapter 5), the UV induced droplets (Chapter 6) and the LC-based lead ion sensor (Chapter 7). The polarized optical microscopy (POM) is modified in a number of ways to allow for different experiments to be conducted.

An external UV light source UVEC-4II was coupled into different system in the following experiments, which are inducing the transition of droplets (Chapter 6), exciting the AIEgens in the lead ion detection system (Chapter 7) and exciting the AIEgens in the force sensor system (Chapter 8). The wavelength of this kind of UV source is 365 nm.

The Abbe refractometer (Model 60/ED) was utilized in Chapter 5 for the measurements of birefringence of nematic liquid crystal 5CB. It can be seen how the refractive index of the liquid crystal material changes with temperature.

References

1. Aemissegger, A.; Hilvert, D. Synthesis and application of an azobenzene amino acid as a light-switchable turn element in polypeptides. *Nat. Protoc.* **2007**, 2, 161-167.
2. Beharry, A. A.; Woolley, G. A. Azobenzene photoswitches for biomolecules. Chem. *Soc. Rev.* **2011**, 40, 4422-4437.
3. Renner, C.; Kusebauch, U.; Löweneck, M.; Milbradt, A.G.; Moroder, L. Azobenzene as photoresponsive conformational switch in cyclic peptides. *J. Pept. Res.* **2008**, 65, 4-14.
4. Hrozhyk, U. A.; Serak, S. V.; Tabiryan, N. V.; Bunning, T. J. Photoinduced Isotropic State of Cholesteric Liquid Crystals: Novel Dynamic Photonic Materials. *Adv. Mater.* **2007**, 19, 3244–3247.
5. Wang, L.; Chen, D.; Gutierrez-Cuevas, K. G.; Krishna Bisoyi, H.; Fan, J.; Zola, R. S.; Li, G.; Urbas, A. M.; Bunning, T. J.; Weitz, D. A.; Li, Q. Optically reconfigurable chiral microspheres of self-organized helical superstructures with handedness inversion. *Mater. Horiz.* **2017**, 4, 1190–1195.
6. Dubtsov, A. V.; Pasechnik, S. V.; Shmeliova, D. V.; Kralj, S. Light and phospholipid driven structural transitions in nematic microdroplets. *Appl. Phys. Lett.* **2014**, 105, 151606.
7. Melton, C.; Riahinasab, S.; Keshavarz, A.; Stokes, B.; Hirst, L. Phase Transition-Driven Nanoparticle Assembly in Liquid Crystal Droplets. *Nanomaterials*, **2018**, 8, 146.
8. Fu, F.; Abukhdeir, N. M. Chiral symmetry-breaking dynamics in the phase transformation of nematic droplets. *Liq. Cryst.* **2018**, 45, 1078-1083.
9. Hong, Y.; Lam, J. W. Y.; Tang, B. Z. Aggregation-induced emission: phenomenon, mechanism and applications. *Chem. Commun.* **2009**, 29, 4332-4353.
10. Li, J.; Wang, J. X.; Li, H. X.; et al. Supramolecular materials based on aie luminogens (aiegens): construction and applications. *Chem. Soc. Rev.* **2020,** 49, 1144-1172.

11. Chen, J.; Law, C. C. W.; Lam, J. W. Y.; et al. Synthesis, light emission, nanoaggregation, and restricted intramolecular rotation of 1,1-substituted 2,3,4,5-tetraphenylsiloles. *Chem. Mater.* **2003,** 15, 1535-1546.
12. Hong, Y.; Lam, J. W. Y.; Tang, B. Z. Aggregation-induced emission. *Chem. Soc. Rev.* **2011,** 40, 5361-5388.
13. Han, T. Y.; Feng, X.; Tong, B.; et al. A novel “turn-on’’ fluorescent chemosensor for the selective detection of Al3+based on aggregation-induced emission. *Chem. Commun.* **2012,** 48, 416−418.
14. Leung, C. W. T.; Hong, Y.; Chen, S.; et al. A photostable aie luminogen for specific mitochondrial imaging and tracking. *J. Am. Chem. Soc.* **2013,** 135, 62-65.
15. Yuan, Y. Y.; Zhang, C. J.; Liu, B. A. A Photoactivatable AIE polymer for light-controlled gene delivery: Concurrent endo/lysosomal escape and DNA unpacking. *Angew. Chem., Int. Ed.* **2015,** 54, 11419−11423.
16. Hu, F.; Xu, S. D.; Liu, B. Photosensitizers with aggregation-induced emission: materials and biomedical applications. *Adv. Mater.* **2018,** 30, 1801350.
17. Liu, Z. Y.; Zou, H.; Zhao, Z.; et al. Tuning Organelle Specificity and Photodynamic Therapy Efficiency by Molecular Function Design. *ACS Nano.* **2019,** 13, 11283–11293.
18. Han, A. T.; Wang, H. M.; Kwok, R. T. K.; et al. Peptide-Induced AIEgen Self-Assembly: A New Strategy to Realize Highly Sensitive Fluorescent Light-Up Probes. *Anal. Chem.* **2016,** 88, 3872-3878.
19. Zhao, D. Y.; Fan, F.; Cheng, J.; Zhang, Y. L.; Wong, K. S.; Chigrinov, V. G.; Kwok, H. S.; Guo, L.; Tang, B. Z. Light-Emitting Liquid Crystal Displays Based on an Aggregation-Induced Emission Luminogen. *Adv. Opt. Mater.* **2014,** 3, 199-202.
20. Zhao, D. Y.; Fan, F; Chigrinov, V. G.; Kwok, H. S; Tang, B. Z. Aggregate-Induced Emission in Light-Emitting Liquid Crystal Display Technology. *J. Soc. Inf. Display* **2015,** 23, 218-222.
21. Zhao, D. Y.; He, H. X.; Gu, X. G.; G, L.; Wongm K. S.; Lam, J. W. Y.; Tang, B. Z. Circularly Polarized Luminescence and a Reflective Photoluminescent Chiral Nematic Liquid Crystal Display Based on an Aggregation-Induced Emission

Luminogen. *Adv. Opt. Mater.* **2016,** 4, 534-539.

Chapter 5 Sensors Based on the Liquid Crystal Droplets that Modified with Different Lipids

As the perception of liquid crystals gradually deepens, more researchers try to apply different phases and forms of liquid crystals to various fields. The structure of the sphere maximizes the surface area under the same conditions, which determines that the liquid crystal in the form of microdroplets is more sensitive in the field of sensing. So, this project is carried out based on the liquid crystal droplets.

In this chapter, we change the surface alignment through surface treatment, which influences the director orientation. Here, we decide to use different kinds of lipids to modify the cholesteric liquid crystal (CLC) droplets, such as Single ferro (SF), Di-ferro (DF), 1,2-dineopentadecane-sn-glycero-3-phosphocholine (DnPdPc), and 1,2-dioleoyl-sn-glycero-3-phosphocholine: 1,2-dioleoyl-sn-glycero-3-[phospho-rac-(1-glycerol)] (DOPC: DOPG). From this, the change of detected data can be magnified into a kind of visible change. Because phospholipids can form lipid bilayers, they are an important part of biomembranes, so that this work is helpful in reaching the ultimate objective of a low-cost, sensitive, and simple-to-read biosensor that has numerous potentials in point-of-care testing.

Much of the work contained in this chapter was published by Xiaoxue Du and Helen F. Gleeson, “Chiral nematic liquid crystal droplets as a basis for sensor systems”, *Molecular Systems Design & Engineering*, 7(6), 2022 [1].

5.1 Materials

The chiral nematic liquid crystals were formed from nematic liquid crystals (5CB/6CB/7CB) and different amounts of a chiral dopant (S1011). The nematic liquid crystals 5CB/6CB/7CB were purchased from SYNTHON Chemicals GmbH & Co. KG, Germany. S1011 was provided by Merck NB-C,

UK. The helical twisting power (HTP) of S1011 is 40 μm^{-1} [2]. The structures of 5CB/6CB/7CB and S1011 are shown in Figure 5.1. In order to mix the components uniformly, chloroform was used to dissolve the mixture, which was then heated and stirred on a magnetic stirrer, dried with nitrogen and finally the solvent was evaporated. Table 5.1 shows the compositions of samples used in the experiments and their pitches calculated with the equation

$$p = [HTP \times x_c]^{-1}, \tag{2-2}$$

where HTP is helical twisting power, and x_c is the concentration of chiral dopant [3]. Here, we regard the CLC mixture with a chiral dopant concentration of 7.3 wt% as the high chirality CLC, and the 0.53 wt% as the lower chirality CLC.

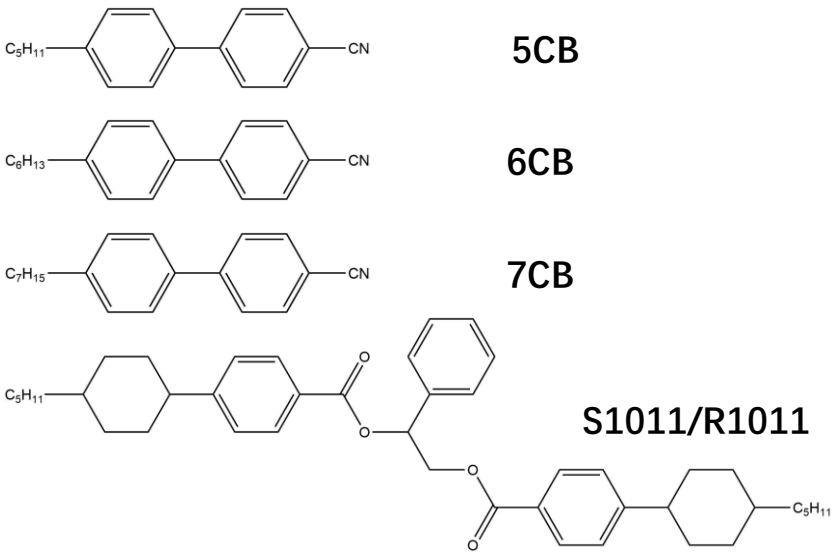

Figure 5.1 Chemical structures of the LCs and chiral dopant used in the experiments.

Table 5.1 The compositions of samples, their N* to isotropic phase transition temperature (from DSC test) and the calculated pitch.

	LC	concentration of S1011	Transition temperature (℃) (from chiral nematic phase to isotropic phase)	Calculated pitch (nm)
S1	5CB	7.3 wt%	27.2	343
S2	6CB	7.3 wt%	25.5	343

S3	7CB	7.4 wt%	36.9	337
S4	5CB	0.53 wt%	34.4	4717

5.2 Preparation of the samples

5.2.1 Preparation of droplets with polyvinyl alcohol coating

The uniform CLC droplets (diameter = 20 μm) with planar alignment induced by PVA (polyvinyl alcohol) coating were produced using a flow focus droplet microfluidic device [4]. The PVA is included to ensure planar alignment at the droplet surface. The PDMS microfluidic device fabrication follows the protocol reported previously [5]. The structure of the microfluidic chip is shown below (Figure 5.2), which is similar to the previous version in our published work [6].

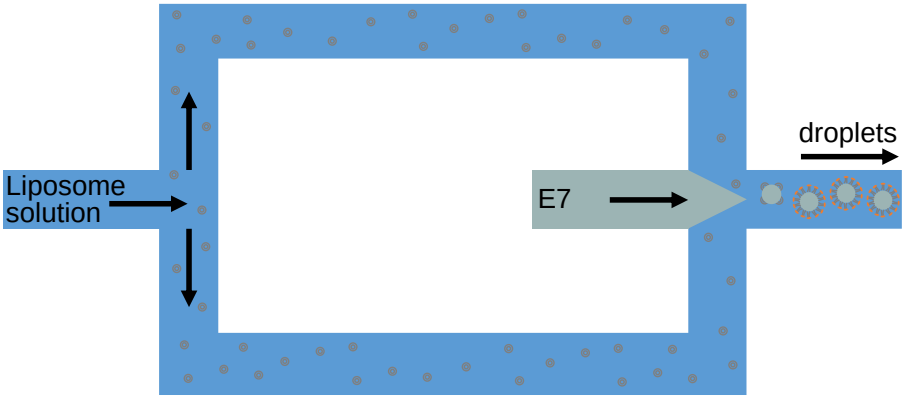

Figure 5.2 Structures of the microfluidic chip. The width of nozzle is about 15 μm and the width and length of channel after the nozzle are 100 μm and 4000 μm, respectively. The depth of all the channels is 25 μm. This microfluidic chip is connected to the syringe pumps through the fine bore polythene tubing.

Two mixtures are included in the microfluidic device; the relevant liquid crystal and an aqueous solution that includes the PVA or lipid that will coat the droplet. For the PVA droplets, firstly, mix PVA and water with ratio of 1: 100. Then, 15 vol% of glycerol was added to the solution in order to increase the viscosity, optimizing the flow properties for microfluid liquid crystal droplet production. Take the PVA buffer and CLC mixtures separately to put into the microfluidic equipment. The flow rate used for LC droplet generation was

0.075 μL·min^{-1} for CLC mixtures and 6 μL·min^{-1} for PVA buffer. The apparatus is allowed to run for 15 minutes, collecting the uniform droplets with a diameter of ~20 μm. The droplet size can be controlled by changing the flow rate of CLC and buffer. A small sample containing the uniform droplets is transferred onto a slide to observe the structure and physical properties of CLC droplets under a polarizing microscope (Leica DM LP).

5.2.2 Preparation of droplets with lipids coating

The lipids that we used were made by hydration and tip sonication of a dried lipid mixture (with 0.1% mol Texas Red) [7]. The four kinds of lipids are 1-palmitoyl-2-dodecaneferrocenyl-sn-glycero-3-phosphocholine (MFPC), 1,2-didodecaneferrocenyl-sn-glycero-3-phosphocholine (DFPC), 1,2-dineopentadecane-sn-glycero-3-phosphocholine (DnPdPC) and 1,2-dioleoyl-sn-glycero-3-phosphocholine: 1,2-dioleoyl-sn-glycero-3-[phospho-rac-(1-glycerol)] (DOPC: DOPG = 1: 1). The structure of the synthesized lipids used are shown in Figure 5.3. The Texas Red was included to allow fluorescence imaging of the lipid-coated droplets, providing confirmation of the presence or removal of the lipid. It will have a conjugation with the reactive groups of amino, sulfhydryl and carboxylic acid. The dyes can bond to the head of the phospholipid group, so that the phospholipid will be labeled and its trace can be detected. The lipid-coated droplets are made in the same way as the PVA coated droplets, changing the PVA solution for the lipids solution. Several different lipids were used to coat the CLC droplets and the results of different surface modifications were observed using a polarizing microscope (Leica DM LP) and fluorescence microscope (Nikon ECLIPSE E600).

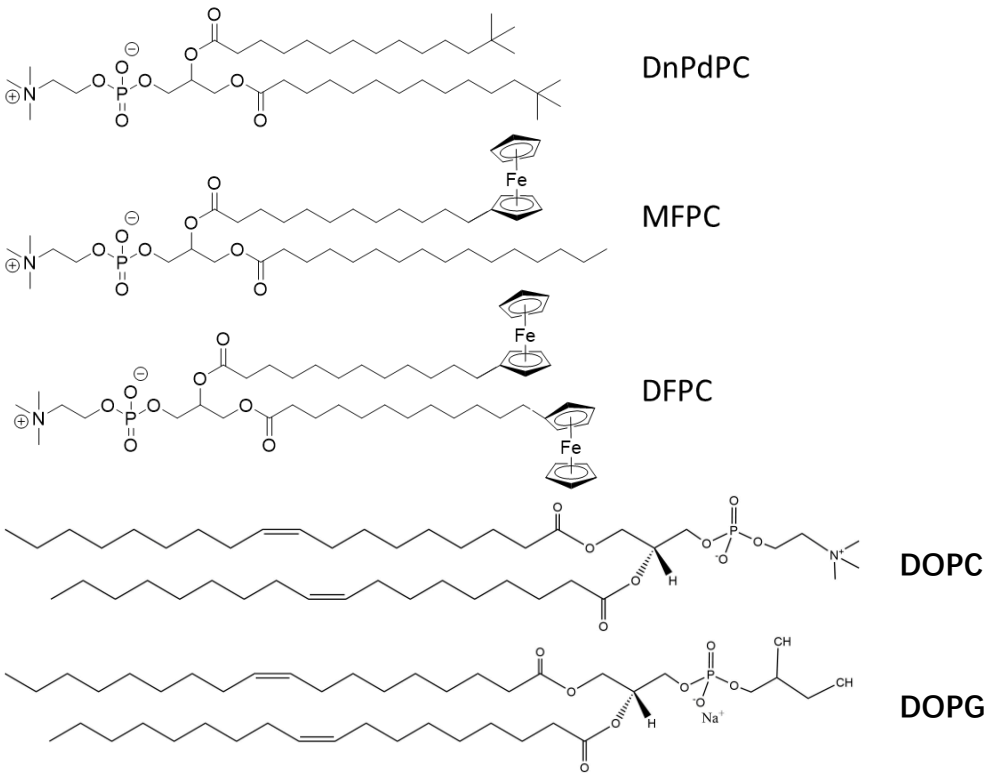

Figure 5.3 Chemical structures of the lipids used in the experiments.

5.2.3 Preparation of chiral nematic liquid crystal film

The optical properties of the high chirality CLC are best determined using a well-aligned thin film of the material. To form a thin film, the CLC is filled into a glass cell with a gap of 5 μm, treated with polyimide to provide excellent planar surface alignment. The empty glass cell was homemade with the spacers distributed at the edges of the cell. Drops of CLC mixture are placed on one of the filling ports and wait for the LC material to entirely fill the cell based on the capillary effect. The uniform monodomain sample formed is ideal for measuring the optical properties of the CLC mixtures. The reflectance spectra are determined on a microscope (OLYMPUS BH-2) coupled to a high-resolution spectrometer (Ocean Optics HR4000), described in detail elsewhere [8]. Temperature control of the sample is achieved by a Linkam hot stage with a relative accuracy of 0.1˚C. On the basis of the spectrometer and the hot stage, the central wavelength of the CLC film's reflectance at different temperature can be obtained in the later. Furthermore, whether the CLC material has a temperature-dependence can be confirmed.

5.3 Results and discussion

5.3.1 The transition temperature (nematic to isotropic) of the CLC

In order to have an obvious comparison of the effects of the chiral dopant's presence, firstly, we use the DSC to measure the transition temperatures for liquid crystals without chiral dopant. The transition temperature for pure 5CB, pure 6CB, and pure 7CB are 34.9 ˚C, 28.7 ˚C, and 30.3 ˚C, respectively, and it is expected that the inclusion of the chiral dopant will lead to a reduction in the transition temperature.

For the chiral liquid crystals, we use the same equipment to measure the transition temperatures of the mixtures. Here, we take the average of the transition temperatures of the second and third cooling processes as the final result (shown in Figure 5.3). The transition temperatures of the high chirality mixtures are 27.2 ˚C, 25.5 ˚C, and 36.9 ˚C for the 5CB, 6CB and 7CB mixtures respectively (the DSC traces are shown in Figure 5.4). Similarly, the transition temperature of the less chiral 5CB mixture, is found to be 34.4 ˚C.

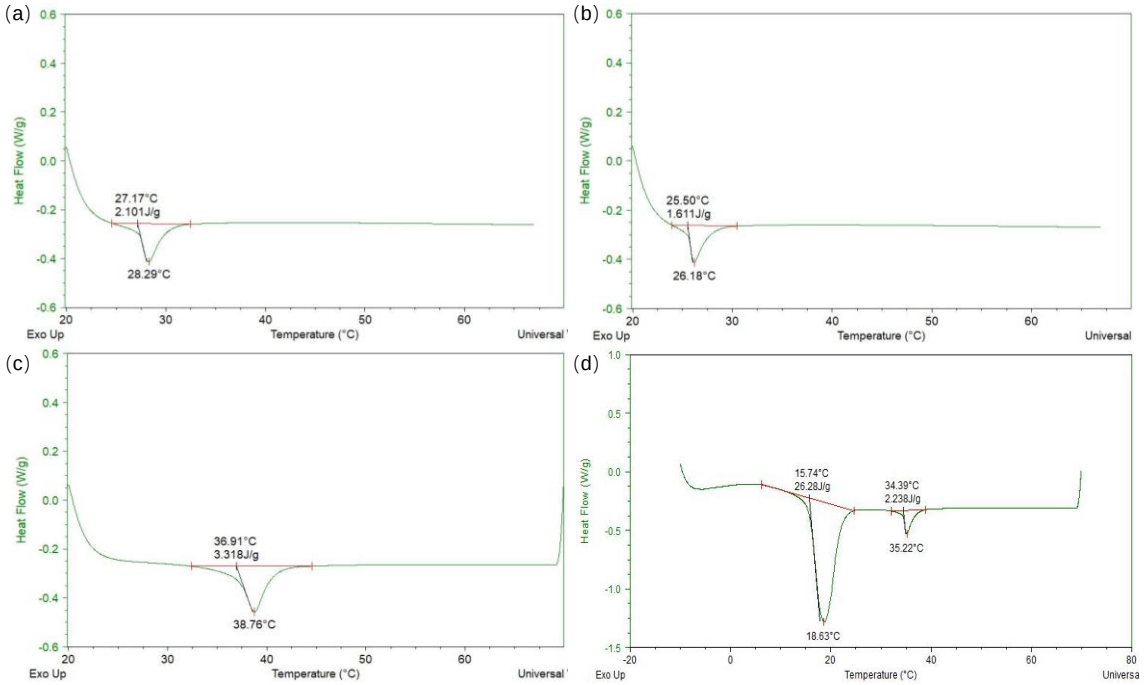

Figure 5.4 The transition temperature for chiral CLC mixtures. (a) for high chiral 5CB, the transition temperature (Tc) is 27.1 ˚C; (b) for high chiral 6CB, the transition temperature is 25.5 ˚C; (c) for high chiral 7CB, the transition temperature is 36.9 ˚C; (d) for less chiral 5CB, the transition temperature is 34.4 ˚C.

5.3.2 The observation of the high chiral CLC droplets

For the high chirality liquid crystal droplets coated with PVA, the structures will not be affected compared to just making droplets with no coating in water, but the droplet stability is improved. Figure 5.5 shows the high chirality 5CB/6CB/7CB droplets in unpolarized transmittance mode, polarized transmittance mode, and polarized reflectance mode separately. The diameters of the droplets are around 20 microns, and the disclination line is clear for the some of them (as shown in Figure 5.5 g, and h). The droplets of high chirality 5CB/6CB/7CB all present the Frank-Pryce structure with parallel surface anchoring. These high chirality droplets look similar to the nematic droplets with radial director in transmission because of the “average birefringence”, shown in Figure 2.2(a). However, they are different from each other in detail. For the Frank-Pryce structure with high chirality, the director lies perpendicular to the radial pitch axis and rotates uniformly.

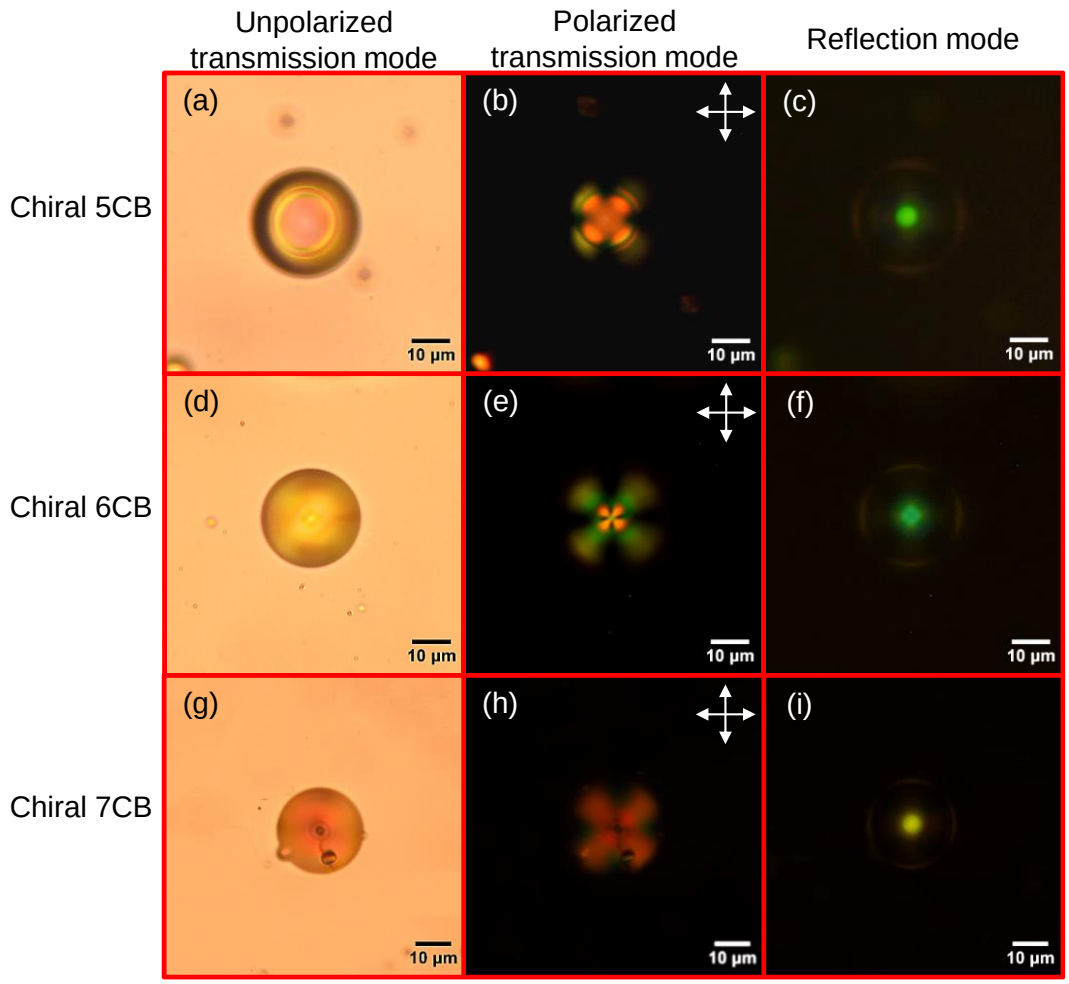

Figure 5.5 The images of LC droplets doped with S1011. (a), (d) and (g) 'bright field' transmission-mode, (b), (e) and (h) transmission-mode, between crossed polarizers and (c), (f) and (i) reflection-mode, between crossed polarizers. (Top row) 5CB, (middle row) 6CB and (bottom row) 7CB.

5.3.3 The pitch analysis of the droplets

The 5CB/6CB/7CB droplets with a concentration of 7.3 wt% of S1011 reflect green light basically, because the expected pitches of them are around 340 nm (shown as Table 5.1). The centre of the reflection band can be calculated from the equation

$$\lambda = \bar{n} \times p, \tag{2-1}$$

If the average refractive index $\bar{n}$ is assumed to be around 1.6, the reflection wavelength is around 544 nm, which is in the range of green to yellow light. The reflection colours of the droplets were confirmed by

measuring the reflection spectra of thin films of the chiral materials.

Here we use the results from the sample of 5CB with S1011 as an example for further analysis below.

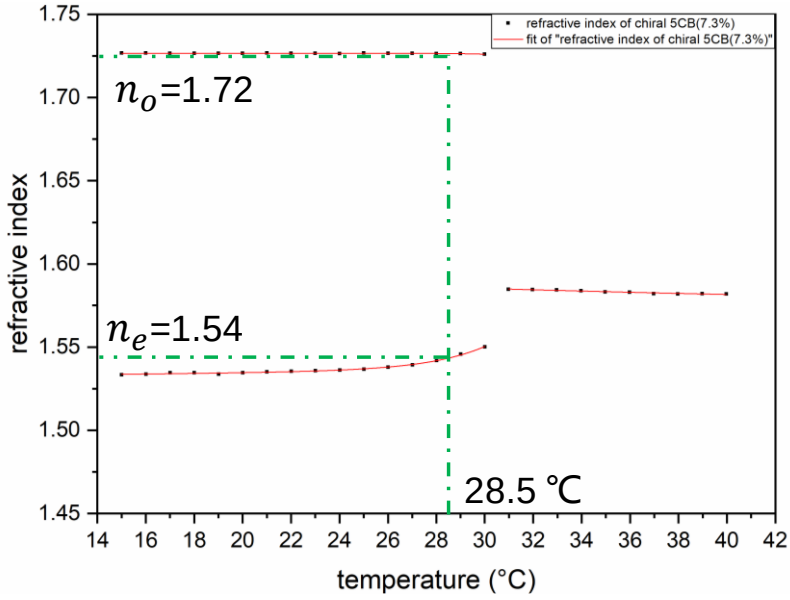

Figure 5.6 Temperature-dependent refractive index of high chiral 5CB (7.3 wt% S1011). The black points are real data of reflective index, and the red curves are fitting line of the refractive index depending on the temperature. The green dash is the auxiliary line of the reflective index at the temperature of 28.5 ˚C. Data are obtained by the Abbe refractometer (Model 60/ED).

By using Abbe refractometer (Model 60/ED), we plotted the birefringence diagram (as seen in Figure 5.6). From the birefringence measurements, we can see how the refractive index of high chirality 5CB changes with temperature. At the temperature of 28.5 ˚C, for example, we can read the n_e is 1.54, and the n_o is 1.72. As shown in Figure 5.7 (a), the high chiral 5CB will reflect a certain range of light at 28.5˚C. Under this condition, the reflection spectrum has a full width at half maximum (FWHM) of 55 μm and a central wavelength of 563 nm. According to the equation of

$$p = \frac{\lambda}{n}, \tag{5-1}$$

we can get two values of the pitch using both n_e and n_o. For one value of the

pitch,

$$p_1 = \frac{\lambda_1}{n_e} = \frac{535}{1.54} = 347\ nm, \tag{5-2}$$

and for the other one,

$$p_2 = \frac{\lambda_2}{n_o} = \frac{590}{1.72} = 343\ nm. \tag{5-3}$$

These two values of the pitch are in good agreement with the pitch that we calculated in Table 5.1, which is 343 nm. These all prove the method that we used to calculate the pitch with the value $HTP = 40\mu m^{-1}$ and the formula (2-2) is correct, so the pitch values that we calculate for less chiral 5CB and high chiral 6CB/7CB mixtures are credible.

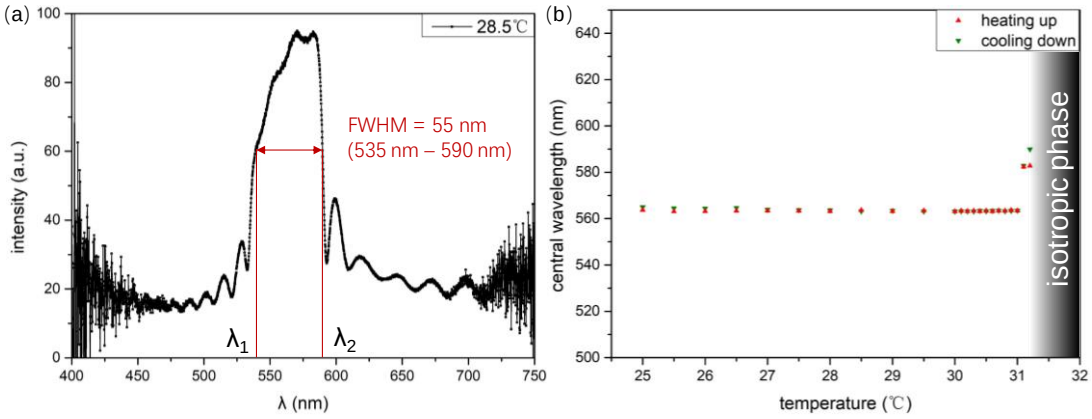

Figure 5.7 The relationship between selectively reflected wavelength and temperature. (a) selective reflection from the sample at 28.5 ˚C. The central wavelength is 563 nm, and the full width at half maximum is 55 nm; (b) the central wavelength has only a slight temperature-dependence (pitch is pinned, but the sample birefringence changes, see Figure 5.6).

When heated, the central wavelength of high chirality 5CB mixture has a weak temperature dependence across the N* phase. As illustrated in Figure 5.7 (b), the central wavelength of high chirality 5CB barely increased when the temperature rises. In addition, from the birefringence chart of high chiral 5CB, we can also see the refractive index changes very slightly as the temperature changes until the transition temperature (as shown in Figure 5.6).

5.3.4 The observation of the less chiral CLC droplets

The less chiral 5CB droplets are made up of 5CB with 0.53 wt% S1011, so the pitch should be 4.7 μm based on the formula (2-2). Therefore, the less chiral 5CB can reflect the light with a wavelength of 4.7 μm, which is in the range of infrared light. It is able to observe the pitches clearly and measure them under the optical microscope. As shown in Figure 5.8, there are many uniform droplets, made microfluidically, in orderly rows and lines. The droplets diameters are approximately 17 μm, and the pitches measured from the Frank-Pryce structure are all around 4.5 μm. Most of these chiral 5CB droplets with PVA show Frank-Pryce structure, and a few of them are spiral.

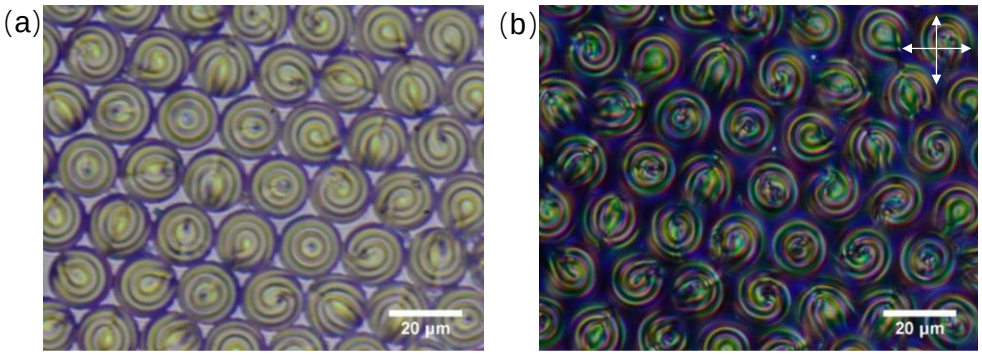

Figure 5.8 A monolayer of PVA coated 5CB droplets doped with 0.53 wt% of S1011 produced microfluidically. (a) Bright field transmission-mode image and (b) transmission-mode image with crossed polarizers.

5.4 The effect of lipid coatings on the LC droplets

We can vary the surface treatments of the nematic liquid crystal droplet with a variety of lipids. As is shown below, we used four kinds of lipids, MFPC, DFPC, DnPdPC and DOPC: DOPG to modify the surface of droplets. Because of the fluorescent dye (Texas red) in the composition, the coating place will become brighter than other areas under the fluorescence microscope, allowing us to verify that the lipids fully coat the droplets.

From other the experiments carried out on pure 5CB, it is known that the droplets present radial structures with MFPC, DnPdPc, and DOPC/ DOPG [9]. However, DFPC, gives a different droplet geometry, forming the bipolar

structure (shown in Figure 5.9).

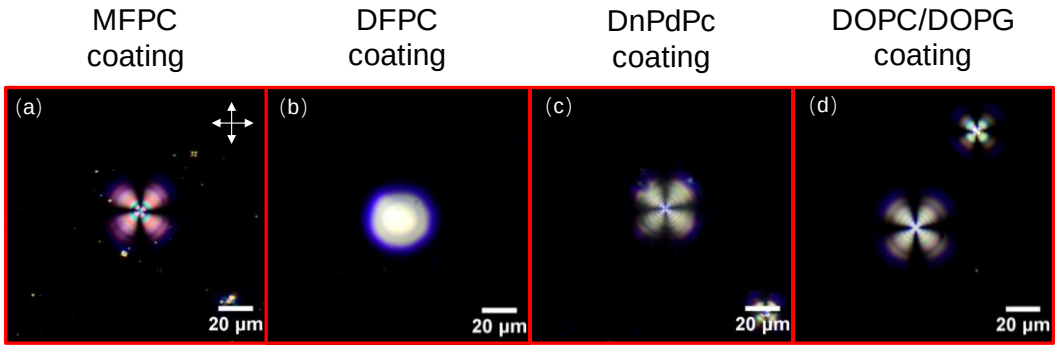

Figure 5.9 Observation of the high chiral 5CB droplets with the optical microscope (a) - (d) the polarized images in transmittance mode.

Nevertheless, the situation for cholesteric liquid crystal droplets is different from those formed from nematic liquid crystals, as the form of droplet makes it more complicated. When the high chirality liquid crystal droplet coated with different lipids, it will form different structures. As is shown above, we used MFPC, DFPC, DnPdPc and DOPC/ DOPG to modify the surface of high chirality 5CB droplets. Only the droplets coated with DFPC maintain the Frank-Pryce structure with parallel surface anchoring, the other three kinds of lipids all change the droplets' surface orientation. From Figure 5.10 (e)-(h), the bright rings that surround the droplets show a coating status with all of the lipids.

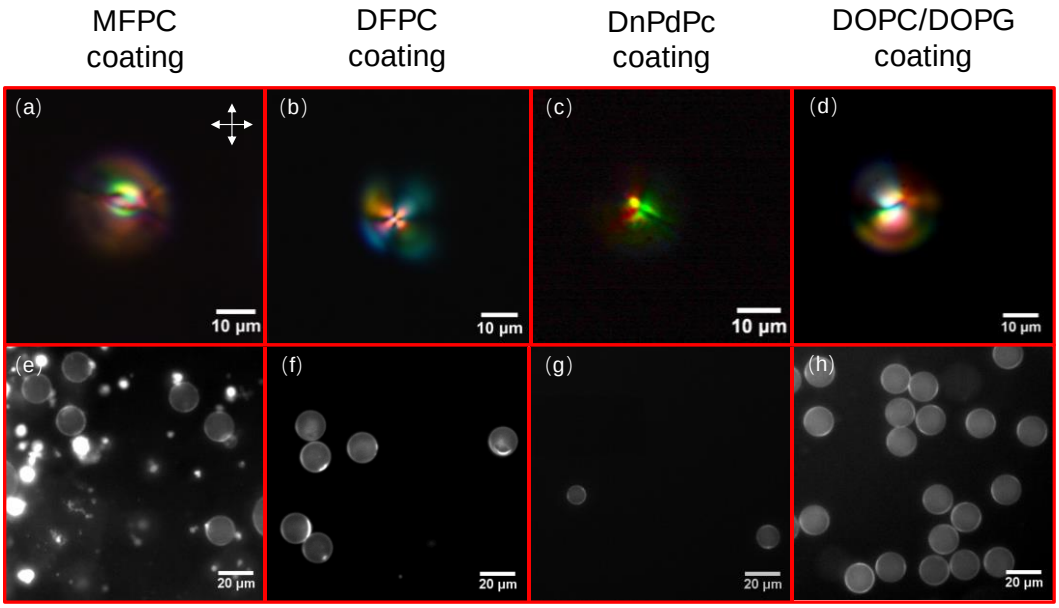

Figure 5.10 Microfluidically produced 5CB droplets doped with ~7.3 wt% of S1011 with the lipid surfactant type detailed in the top row. (a) - (d) Transmission-mode images between crossed polarizers; (e) - (h) Fluorescence images.

Similar to the high chirality 5CB, the less chiral 5CB droplets are also affected by the different lipids, and as a result, present different director structures. The lipid MFPC, DnPdPc and DOPC/ DOPG destroyed the director's original relationship with the pitch axis. All these four lipids coat these uniform less chiral 5CB droplets very well, as illustrated in Figure 5.11 (i)–(l).

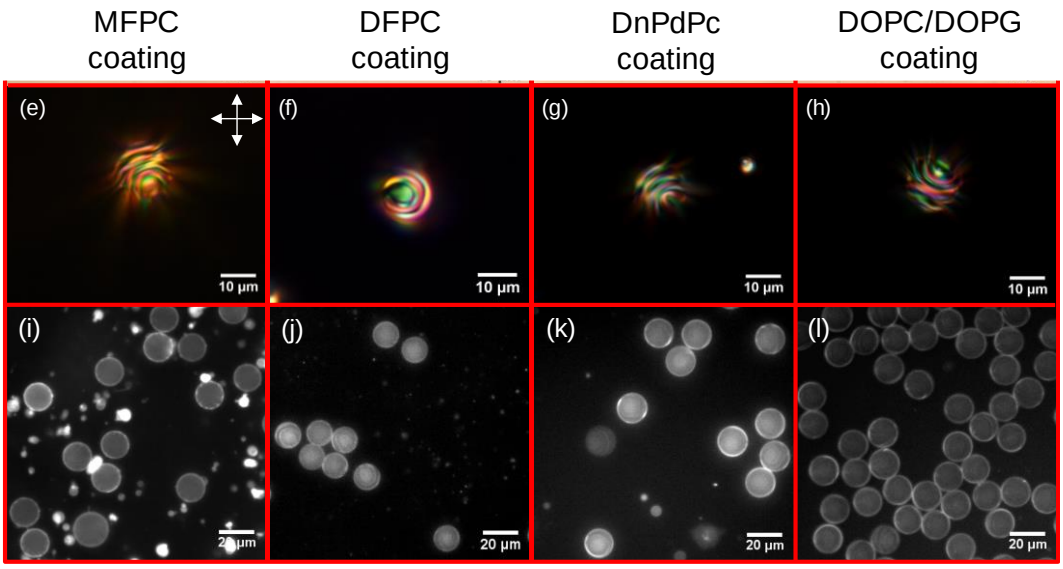

Figure 5.11 Microfluidically produced 5CB droplets doped with 0.53 wt% of S1011 with the lipid surfactant type detailed in the top row. (a)-(d) Transmission-mode images between crossed polarizers; (e) - (h) Fluorescence images showing a clear bright ring around the droplets which can be assigned to a lipid monolayer.

5.5 Summary

It is important to be able to control the surface anchoring properties, particularly for the phospholipid-coated LC droplets (droplets of the type relevant to the creation of biosensors). This is because, for most LC/phospholipid combinations, the phospholipid monolayer promotes such strong perpendicular anchoring that switching of the anchoring to planar, and the subsequent reorientation of the director field, is rather difficult.

According to the work shown here, some points are discovered and worth thinking about more deeply. Different CLC mixtures have different Nematic-Isotropic transition temperatures. The temperature for 5CB+0.53%S1011, 5CB+7.3%S1011, 6CB+7.3%S1011 and 7CB+7.3%S1011 are 27.2 ˚C, 30.2 ˚C, 25.5 ˚C and 36.9 ˚C separately, which are all higher than room temperature. What's more, the CLC mixtures that we use have only a slight temperature dependence, which is good for the stability of the proposed devices.

The uniform droplets we made using microfluidic method are all around 17 μm in size. The high chirality droplet has a pitch of ~ 340 nm, and it can reflect green light. However, the pitch of less chiral droplet is close to 3.4 μm,

and the reflected light from less chiral liquid crystal would be in the infrared range.

Generally speaking, all four kinds of lipids (MFPC, DFPC, DnPdPc and DOPC/ DOPG) can coat the droplets well. Most pure LC droplets with a PVA coating show a bipolar structure. MFPC, DnPdPc and DOPC/ DOPG coating changes the structure from bipolar into radial, while the DFPC coating helps the droplet to maintain a bipolar structure. For the less chiral LC droplets, most of them present a Frank-Pryce structure with a PVA coating. MFPC, DnPdPc and DOPC/ DOPG influence their structure while DFPC keeps the original Frank-Pryce structure. Similarly, the high chirality LC droplets mainly form as a kind of Frank-Pryce structure with parallel surface anchoring. Likewise, MFPC, DnPdPc and DOPC/ DOPG play a role to make a difference, but DFPC does not affect the structure. After repeated testing, the MFPC and DFPC lipids are found to be ‘sticky’, which may influence droplets’ stability and cause fluorescent ‘pockets’ that can be seen in some of the images. Comparatively speaking, the DOPC/ DOPG is the most stable one among these four lipids.

By selecting either the LC or the phospholipid, it is possible to combat the natural propensity for strong perpendicular anchoring. The results obtained for these chiral droplets follow those we previously obtained for their non-chiral counterparts, demonstrating that the effect of these two components on the alignment's sign is not appreciably modified by the presence of a chiral dopant. The ability to switch between highly reflective Frank-Pryce structures with planar anchoring and lower reflective structures with perpendicular anchoring, however, suggests that chiral doped LC droplets will prove to be much more useful in developing workable sensor systems due to the strong optical signature associated with the change in director field.

The work described above represents effective progress in achieve the aim of producing biological sensors with chiral nematic liquid crystal droplets. Phospholipids are a major component of biomembranes as they can form lipid bilayers, so these lipid-coated droplets have a lot of potential in this area. We

can control the initial droplet geometry as radial alignment by choice of lipid, ensuring it becomes planar (Frank-Pryce) on removal of lipids by bacterial toxins, which would allow a color change rather than birefringence change [6]. Hope our results are useful for the realizing the ultimate goal of a cheap, sensitive and easy-read biosensor, which could find wide applications in point-of-care testing.

References

1. Paterson, D. A.; Du, X. X.; Bao, P.; Parry, A. A.; Peyman, S. A.; Jones, J. C.; Sandoe, J. A. T., Evans, S. D.; Luo, D.; Bushby, R. J.; Jones, J. C.; Gleeson, H. F. *Mol. Syst. Des. Eng.*, **2022**, 7, 607-621
2. Yang, Y. Optical trapping of nematic and chiral nematic liquid crystalline droplets. PhD diss., University of Manchester, **2009**.
3. Cook, M. J.; Wilson, M. R. *The J. Chem. Phys.* **2000**, 112, 1560-4.
4. Hsiung, S. K.; Chen, C. T.; Lee, G. B. Micro-droplet formation utilizing microfluidic flow focusing and controllable moving-wall chopping techniques. *J. Micromech. Microeng.* **2006**, 16, 2403.
5. Kim, J.; Khan, M.; Park, S. Y. Glucose sensor using liquid-crystal droplets made by microfluidics. *ACS Appl. Mater. Interfaces.* **2013**, 5, 13135-13139.
6. Bao, P.; Paterson, D. A.; Harrison, P. L.; Miller, K.; Peyman, S.; Jones, J. C.; Sandoe, J. A. T.; Stephen D. Evans, S. D.; Bushby, R. J.; Gleeson, H. F. Lab Chip, 2019,19, 1082-1089.
7. Bao, P.; Cheetham, M. R.; Roth, J. S.; et al. On-Chip Alternating Current Electrophoresis in Supported Lipid Bilayer Membranes. *Anal. Chem.* **2012**, 84, 10702-10707.
8. Yoon, H. G.; Dierking, I.; Gleeson, H. F. Cholesteric pitch divergence near smectic phase transitions. *Phys. Rev. E.* **2010**, 82, 011705.
9. Paterson, D. A.; Bao, P.; Abou-Saleh, R. H.; Peyman, S. A.; Jones, J. C.; Sandoe, J. A. T.; Evans, S. D.; Gleeson, H. F.; Bushby, R. J. *Langmuir*, **2020**, 36, 6436-6446.
10. Bao, P.; Paterson, D. A.; Peyman, S. A.; Jones, J. C.; Sandoe, J. A. T.; Bushby, R. J.; Evans, S. D.; Gleeson, H. F. *Crystals*, **2021**, 11, 65.

Chapter 6 Sensors Based on Liquid Crystal Droplets influenced by UV Light

Cholesteric liquid crystals have attracted much attention in several fields due to their complex and interesting structures accompanied with particular optical properties making them low-cost, label-free and sensitive. In this work, Light-driven dynamic hierarchical architecture of three-dimensional self-assembled cholesteric liquid crystal droplets can be obtained, which provides an interesting way to write novel structural alignments within droplets and has potential use in fields of biosensors, soft photonics, and functional materials.

In this chapter, we manifest light-driven changes in the topological configuration of cholesteric liquid crystals droplets, examined experimentally. Photo-responsive azo-LC doped CLC droplets were manipulated by irradiation by UV light to form novel topological configurations with stable 3D structures. Several topological configurations of CLC droplets have been demonstrated such as closed-ring structures with cone-shaped centers and concentric elliptical centers, and open-ring structures formed under uni-directional illumination of UV light. Structures with parallel CLC pitch lines at the centre and with a central point singularity are also formed under multi-directional illumination. All proposed configurations are stable and controllable by light, which enable CLC droplets novel topological structures with new characteristics.

6.1 Introduction

The typical form of CLC in restricted geometries is in spherical particles and as such CLC droplets [1-3] exhibit a lot of potential applications in such as environmental sensors and biosensors [4-7], communication system [8-9], security identification [9-10], hierarchical materials assembly [11], microlasers [8, 12], random lasing and band edge lasing [13] and active laser arrays [14].

CLC droplets have complex and interesting 3D structures accompanying with particular physical and optical properties of low-cost, label-free and sensitive. The applications of CLC droplets are inseparable from the structure of CLC droplets. However, the reports CLC droplets with stable topological structures are still very limited, and most of them are restricted to Frank-Pryce structure (onion-like concentric structure with a line defect) [4-5, 8-10], which extremely hinders the fast development and broad application of CLC droplets-based devices. We previously tried LC/phospholipid combinations to realize an analyte-induced droplets transition between a Frank–Pryce structure (with planar anchoring) and a nested-cup structure (with perpendicular anchoring), which suggested as a prime option for being used as the foundation for creating inexpensive, single-use sensor devices based on liquid crystal [15].

Researchers have studied the properties of CLC droplets with different structures by experiments and simulations [1-2,16-17]. Frank-Pryce structure, nested-cup structure, equatorial structure, were evidenced in the droplets for several biological applications [15]. The structure of CLC droplets can be regulated by changing the solute in solution [1, 15, 17-18], changing the temperature of solution [19-21], changing the pitch of the CLC and surface anchoring by light [8-22]. The alteration of a surfactant, for example, sodium dodecyl sulfate [17], imidazolium ionic liquids [18] and phospholipid [15] can control the surface anchoring of droplets, whose structures are relatively stable. The reconfiguration of CLC droplets can be realized by changing the temperature of the solution [19-21]. The droplets will switch from isotropic to a Frank-Pryce structure when cooled down [20]. In addition, the structure in droplets can be influenced through changing the pitch of CLC and surface anchoring by light [8, 22]. Wang *et al.* evidenced a light-driven chiral switch through the combination of left-handed axially chiral molecular and right-handed photo-insensitive chiral dopant. The droplet's configuration switched from Frank-Pryce to bipolar nematic upon UV light irradiation [8]. Orlova *et al.* explained that the spiraling structure's pitch gradually increases until it

vanishes forming a bipolar configuration [22]. Nevertheless, all the previous methods can only obtain CLC droplets with limited structures of Frank-Pryce or chiral bipolar structure. Electric field [23] and magnetic field [24-25] were applied on the CLC droplets to achieve new topological configurations. According to Swisher's work, the Frank-Pryce structure elongates into a prolate ellipsoid with increasing electric field strength before the director becomes parallel to the field [23]. Mullol *et al.* reported inducing an elliptical concentric structure using magnetic field [25]. Although electric and magnetic fields can induce the CLC droplets to form new configurations, the fields must be maintained to retain such configurations. Therefore, how to achieve new topological configurations in CLC droplets with 3D structures that are stable in the absence of an external stimulus is still a challenge.

Photo-responsive azobenzene liquid crystal (azo-LC) doped CLC droplets were manipulated by irradiation using ultraviolet (UV) light to form novel topological configurations with 3D structures that are stable on removal of the illumination. Under the irradiation with UV light, the part of a CLC droplet near UV light quickly transforms into the isotropic phase, and the other part away from UV light remains as CLC. After turning off the UV light at an appropriate time, the isotropic part of CLC droplet gradually reverts to the CLC state. During the recovery process, different structures can be observed in the CLC droplet. The configurations form as a result of phase transitions in the CLCs. Several topological configurations have been demonstrated under one-directional illumination of UV light such as closed-ring structures with cone-shaped centers and concentric elliptical centers, and open-rings structures. Structures with parallel CLC stripes center and with central point singularity can be formed under multi-directional UV illumination.

6.2 Materials

The CLC droplets were produced by a microfluidic chip that we made using polydimethylsiloxane (PDMS). The production process of the microfluidic chip

can be found in Chapter 4.4. The PDMS material used in this experiment was SYLGARD184, which was purchased from Dow Corning (USA).

The buffer consists polyvinyl alcohol (PVA), sodium dodecyl sulfate (SDS), and deionized water (DI water). The PVA and SDS is used to ensure a planar and vertical alignment of the LC director at the droplet surface, respectively. These two kinds of surfactants (PVA and SDS) will compete with each other in the alignment process if mixed.

The CLC mixture is made up of the nematic liquid crystal 5CB (4-Cyano-4'-pentylbiphenyl, purchased from HCCH), the chiral dopant S811 (obtained from HCCH), and the azo-LC 1205 (purchased from Beam.co). The structures of the chemicals are shown in Figure 6.1. Table 6.1 shows three kinds of CLC mixtures used in our experiments (M1, M2, and M3).

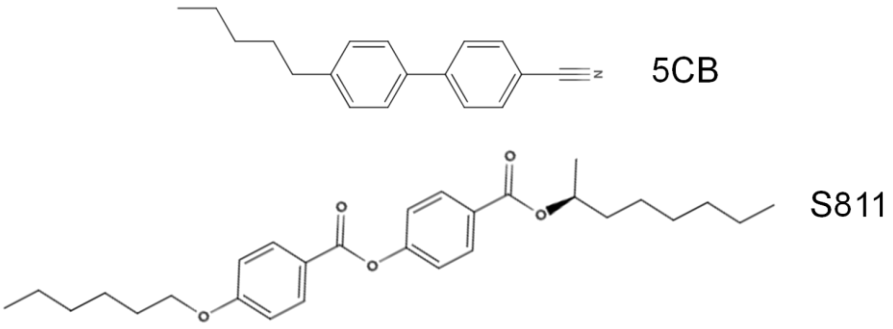

Figure 6.1 The molecule structure of materials

Table 6.1 The composition of the CLC mixtures used in the different experiments

	5CB	S811	Azo-LC 1205
M1	95 wt%	1 wt%	4 wt%
M2	94 wt%	2 wt%	4 wt%
M3	93 wt%	3 wt%	4 wt%

After generation, a small sample of the uniform droplets is transferred onto a slide to observe the structure and physical properties of CLC droplets under the polarization optical microscopy (POM, Nikon Ci).

6.3 Preparation of the uniform droplets

In order to provide better evidence of the Frank-Pryce structure through visualisation of the Bragg-Onion layering, the droplets with larger sized and less chiral compared to the previous chapter are generated. Figure 6.2 demonstrates the schematic illustration and microscope image of the microfluidic setup for CLC droplets generation, respectively. The microfluidic chip is made up from PDMS, and the width of the channel is 150 μm. There are two inlets in this droplet formation device, where the buffer is injected from the left entrance as the outer aqueous and divided into two side channels at the first conjunction, as the yellow arrows show. The CLC mixture (M2) is pumped into the chip through the middle entrance and surrounded by the buffer at the second conjunction. CLC droplets with diameter of 60 μm and pitch of 4.9 μm (inset figure) can be generated from the right-hand outlet when the flow rate of CLC mixture and buffer are set to be 0.01 μl/s and 0.25 μl/s, respectively.

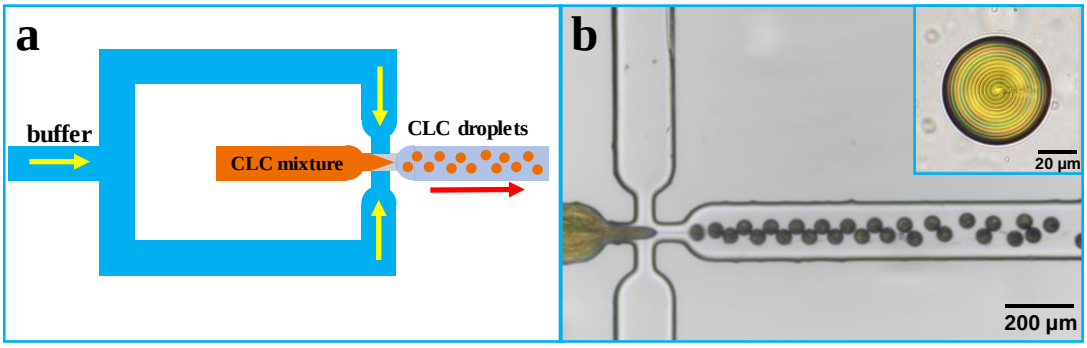

Figure 6.2 The structures of the micro-channel in the PDMS chip. (a) the schematic of the droplets generation; (b) the real process of droplets' generation through microfluidic technology observed under the microscope. The inset figure of b is an image of the generated droplets observed under the optical microscope.

6.4 Experimental setup

The experimental setup to observe the CLC droplet using M2 during the UV-induced phase transition was illustrated in Figure 6.3 (a). The CLC droplet is

dispersed in aqueous solution containing about 3 wt% PVA and 0.2 wt% SDS. The CLC contains 2 wt% S811, 4 wt% azo 1205 and 94 wt% 5CB. The UV light has a wavelength of 365 nm and an intensity of 5 mW/cm^2. The best direction of UV light should be horizontal which helps the observation of the progress of the phase transition interface in the CLC droplets. However, purely horizontal UV light will be strongly scattered by the cell. As shown in Figure 6.3 (a), the incident direction of the UV light was set to be deviated from the horizontal direction by a small angle (here we set it as 30°). The schematic structure of initial CLC droplet with the well-defined Frank-Pryce structure is depicted in Figure 6.3 (b), where the LC, trans-azo-LC, and cis-azo-LC are represented by green rods, brown rods, and a bending rod, respectively.

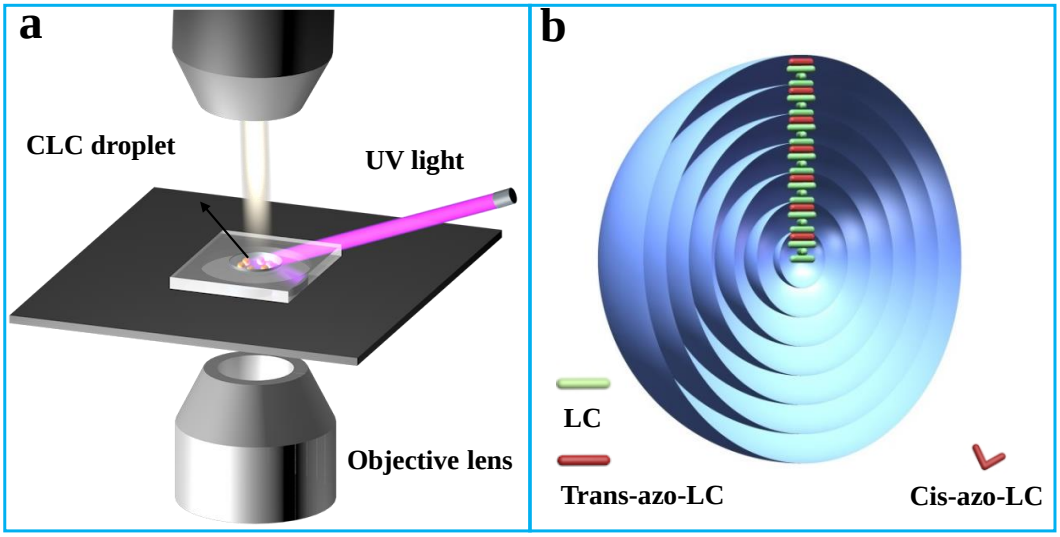

Figure 6.3 (a) The experimental setup to observe the CLC droplet during the phase transition triggered by UV light. (b) The schematic diagram of the CLC droplets with planar surface alignment – the Frank-Pryce structure.

6.5 Results and discussion

6.5.1 The observation of the azo-CLC droplets

During the phase transformation of photo-controlled chiral nematic liquid crystal droplets, it is found that the interface morphology of the CLC boundary is related to the planar anchoring strength of the droplet's surface [1, 16]. The solute of PVA produces a CLC droplet with planar surface anchoring while the

SDS decreases the strength of planar surface anchoring. The strength of the planar anchoring of liquid crystal molecules on the surface of the droplets can be changed by adjusting the concentration of PVA and SDS [15]. The concentration of PVA is fixed to 3 wt% and the concentration of SDS was set to be 0, 0.1, and 0.2 wt% separately. After generating them from the microfluidic device, the droplets were further induced by the UV light (365 nm, 1.5 mW/cm^2) in this section of experiment. All the droplets in our experiments presents Frank-Pryce structure at original state, which has several concentric circles (Figure 6.3). The helical twisting power (HTP) of S811 is 10.1 μm^{-1}. According to the equation

$$p = [HTP \times x_c]^{-1}, \tag{2-2}$$

the pitch for this kind of droplets is calculated to be 4.9 μm.

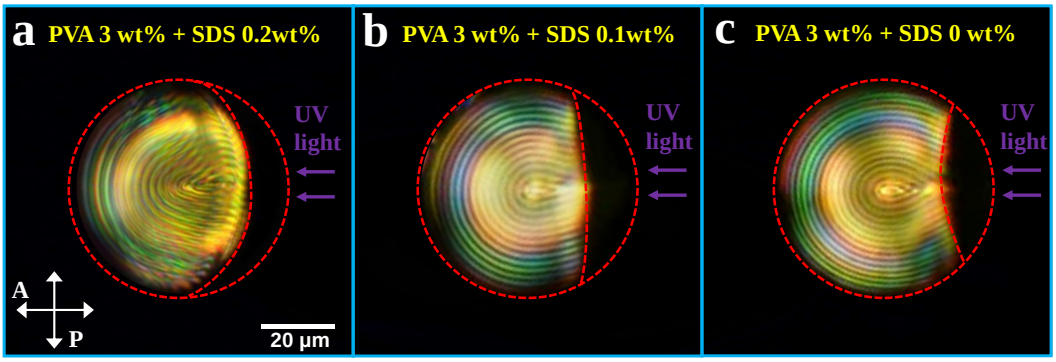

Figure 6.4 Polarizing microscopy images of CLC droplets after UV light illumination (365 nm, 1.5 mW/cm^2) in buffers comprising (a) 3 wt% PVA and 0.2 wt% SDS, (b) 3 wt% PVA and 0.1 wt% SDS. and (c) 3 wt% PVA and 0 wt% SDS. The scale bar is 20 μm in images (a) – (c).

There are three typical states of the droplets' two-phase interface in three different types of environments (Figure 6.4) after UV light illumination, where the corresponding LC-isotropic phase interface demonstrates different shapes due to different buffers. The strength of surface anchoring plays a significant role in the light phase transition. The transformation area (the black area or isotropic phase) in the CLC droplet is induced by the UV light, where the

decrease in order resulting from the trans-cis isomerization of the azo-LC induces a transition from the LC phase to the isotropic phase. In Figure 6.4 (a), where the buffer contains 3 wt% PVA, 0.2 wt% SDS and deionized water, the UV light induced phase boundary is convex; the isotropic region takes the shape of a crescent moon. The photo image is obtained under POM, where P and A represent the polarizer and analyzer directions respectively. When the concentration of SDS is reduced to 0.1 wt% or 0 wt%, as illustrated in Figure 6.4 (b) and (c), the edge of the UV light induced transformation area varies as well. In our following experiment, to achieve phase transition of CLC droplets more easily at the same UV light intensity, the concentration of PVA and SDS is fixed at 3 wt% and 0.2 wt%, respectively.

6.5.2 The phase transition under the UV exposure

The CLC droplets doped with trans-azo-LC are opaque to 365 nm UV light which results in a limited penetrating depth. Ideally, the trans-state azo-LC molecules absorb UV light and transforms into cis-state, which induces CLC to rapidly transform into the isotropic phase. The azo-LC molecules with cis-state cannot absorb UV light anymore which means the isotropic phase in the droplet is transparent to UV light, so the UV light continues to go deep into the droplet until the droplet completely become isotropic phase.

The light driven phase transition from chiral nematic to the isotropic phase in the CLC droplets is important for the further exploration about controlling the structural changes induced by phase transition. The CLC droplets are dispersed in aqueous solution containing 3 wt% PVA and 0.2 wt% SDS. The strength of surface anchoring plays a significant role in the light phase transition. The dynamic process of the light-driven phase transition in CLC droplet observed under POM at 0 s, 24 s, 30 s, and 42 s of UV light exposure, is shown in Figure 6.5(a)-(d), respectively. Before UV light exposure, the CLC droplets is completely cholesteric [Figure 6.5(a)]. After UV light exposure, the azo-LC molecules will absorb UV light and undergo a transition from the trans-

state to the cis-state, which induces an LC-isotropic phase transition. This transition progresses with time, causing the isotropic region to grow (Figure 6.5(b)-(c)). The CLC and isotropic regions can distinguish in POM by their vivid birefringence color and dark appearance, respectively. The azo-LC molecules in their cis-state do not absorb UV light which means the isotropic region in droplet transmits the UV light, thus the UV light will continue to go deep into the droplet until the droplet completely transitions to the isotropic phase [Figure 6.5(d)].

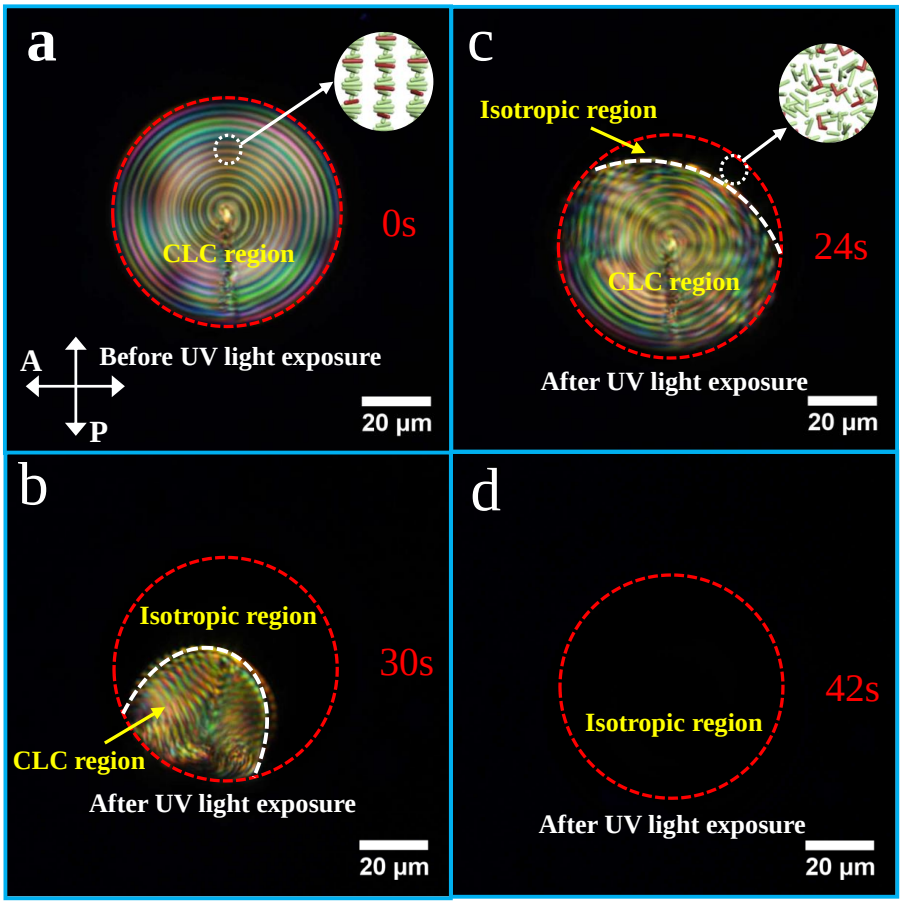

Figure 6.5 The four states of the CLC droplet gradually change into the isotropic phase. The images of the droplets observed at (a) 0 s; (b) 24 s; (c) 30 s; (d) 42 s. The CLC droplet is dispersed in an aqueous solution containing about 3 wt% PVA and 0.2 wt% SDS. The CLC contains 2 wt% S811, 4 wt% azo 1205 and 94 wt% 5CB. The wavelength of the UV light is 365 nm, and the intensity is 5 mW/cm^2.

6.5.3 The analysis of the UV exposure's induction

The next stage considers how the light driven phase transition can be used to

direct the configurations of CLC droplets. The UV light was turned off at specific points during the phase transition and the droplets with a crescent-shaped isotropic region [as in Figure 6.4(a)] were seen to form new structures. The CLC droplets with Frank-Pryce structure are known as particularly stable because they not only keep the structure during considerable perturbation such as water flow, but also make self-recovery to the initial states even after partial disordering [15]. It is intuitive that the structure of CLC droplet can restore to the Frank-Pryce structure quickly if the UV light was turned off at the very early stage of phase transition, which was verified in our experiments. The key point that determines the relaxed topological structure of the CLC droplet is how much the phase transition trigger CLC droplets to form some new topological structures after turning off the UV light.

A central angle θ that corresponds to the angle between the droplet equator and the edge of the isotropic phase at the surface of the CLC droplet can be used to represent the progress of the light-driven phase transition, as shown in Figure 6.6(a). There are two forces might trigger the topology change of CLC droplets. The first force $F_{interface}$ is from the iso-CLC interface and exerted on the ends of CLC stripes in contact with the interface which tends to bend CLC stripes to be perpendicular to the interface. The $F_{interface}$ causes a collective motion of the CLC pitch lines along with the interface. The other force $F_{elasticity}$ comes from the elasticity energy. These two forces work together to reorganize the part of CLC stripes to be straight and perpendicular to the interface. The reorganized CLC stripes are dominated by the elasticity energy and the iso-CLC interface energy (called as EI stripes in the following) while the other CLC stripes are still remain as Frank-Pryce structure, as shown in Figure 6.6(b).

The central angle θ corresponding to the isotropic phase in a CLC droplet is used to represent the progress of light-driven phase transition. The value of θ is regarded as the threshold for topological changes of CLC stripes. The value of the threshold θ in CLC droplets determines the distinct topological

differences that occur following the cessation of the UV radiation through the recovery of CLC from the isotropic phase. Beyond the threshold, the structure of central CLC pitch lines will be maintained during the broadening of the isotropic phase area, and the shape of the inner CLC stripes is stretched as spherical cones in the recovery even if the UV light is turned off. The threshold θ in CLC droplets is related to the diameter (R) of the CLC droplets as shown in Figure 6.6 (c) that the threshold θ increases as the R increases. The density of bending energy can be expressed as

$$E = \frac{1}{2} k_{33} \left(\frac{\partial n_x}{\partial z} + \frac{\partial n_y}{\partial z} \right)^2, \quad (6\text{-}1)$$

where E is the density of bending energy, k_{33} is the bend elastic constant. The small, non-zero components n_x and n_y describe the fluctuations of the optical axis at any point, and z axis is the optical axis.

The density of the bending energy in Frank-Pryce structure is inversely proportional to the rule of

$$E \propto 1/r^2, \quad (6\text{-}2)$$

where r represents the maximum curvature radius of the CLC stripes in the isotropic region, as reflected in Figure 6.6(a). For CLC droplets with a fixed radius R, the curvature radius r of the CLC stripe near the iso-CLC interface decreases with the progress of the isotropic phase and the density of the suppressed bending energy increases. The higher bending energy stretches inner CLC stripes towards the interface much easier in this situation. However, it goes different for CLC droplets with a variable radius R. The distance r from droplet's center to the interface increases when the radius R of droplet increases, even though the central angle θ corresponding to the isotropic phase is a constant. These can explain that the larger CLC droplet requires a larger threshold angle θ to achieve a particular density of bending energy of

CLC stripes near the interface.

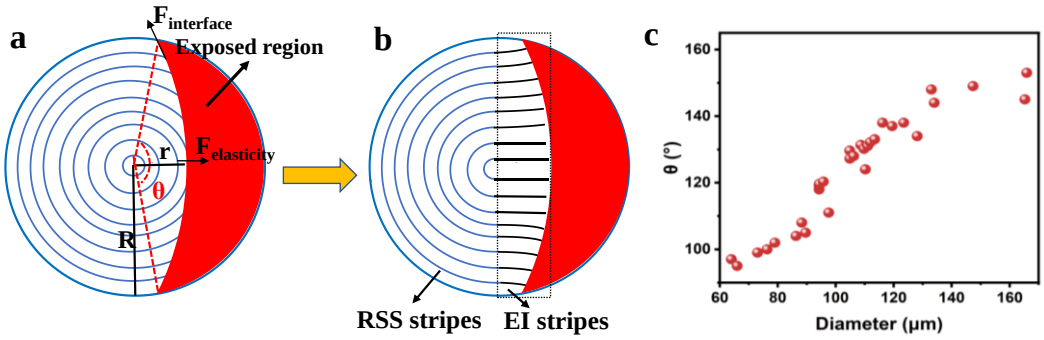

Figure 6.6 CLC stripes are similar to Frank-Pryce stripes and the integrity of circular CLC stripes near the droplet center is kept. (a) The schematic of droplet's partial phase transition and force analysis at the critical condition. The UV light is turned off at once. (b) The schematic of the droplet's recovery process. (c) The threshold θ in CLC droplets with various diameters. The buffer solution contains 3 wt% PVA and 0.2 wt% SDS.

Once the angle θ is larger than the threshold in a CLC droplet, the topological structure of CLC stripes will change, driven by the free energy. The changed stripes in turn store potential energy that hindered the perfect recovery of Frank-Pryce structure when the UV light is turned off and CLC droplets with new metastable architectures can be obtained. The stretched inner stripes are finally perpendicular to the interface as shown in Figure 6.6(b). The relationship between the threshold θ of the isotropic state and the diameter of the droplet during the light-controlled phase transition induced onion-like CLC droplets to produce stripes. The trend is depicted in Figure 6.6 (c), which demonstrates that the larger the droplet diameter, the larger the threshold θ.

6.5.4 The droplets' internal conformation under induction

A typical topological change of CLC droplets triggered by the phase transition is shown in Figure 6.7(a). The initial structure of the droplet is Frank-Pryce structure which can be regarded as some closed circular stripes and the existence of the isotropic phase break the integrity of CLC stripes that contacted with the interface. The CLC stripes near the droplet center that are

not in contact with the interface in Figure 6.7(a) i & ii are still circular stripes. The further UV illumination will facilitate the disappearance of the integrity of inner stripes. The spontaneous stretch of central circular stripes towards the iso-CLC interface becomes much stronger with the continuous advance of iso-CLC interface. However, after turning off the UV light, the shapes of the inner CLC stripes change quickly. The final recovered structure is shown as Figure 6.7(a) iii-v, in which the inner CLC stripes are cone-shaped. Such a shape change mainly comes from the elasticity energy. The existence of the isotropic phase frees the suppressed elasticity energy, especially the bending energy, which is derived from the competition of elasticity energy and surface energy. The force $F_{elasticity}$ stretches the central circular stripes towards the iso-CLC interface. The CLC stripes in Figure 6.6(a) are stretched to be cone-shaped.

The new topology structure in Figure 6.7(b) shows as the concentric ellipses, which are similar to the tracks for running. The EI stripes in Figure 6.6(c) keep parallel after the recovery. As the UV illumination continues, the EI stripes further progress [Figure 6.7(d)] and the area of Frank-Pryce stripes decreases as the continuous forward shift of the iso-CLC interface. The droplet in Figure 6.7(d) recovers to a layer by layer of acute angle structure. The concave iso-CLC interface induces EI stripes to be divergent. Potential energy is stored in those divergent EI stripes, which promotes the later growth of CLC stripes to keep the divergent orientation. However, the divergent orientation is not preferred by the surface anchoring. After turning off the UV light, the shaping effect of surface energy increases and the CLC stripes get as smooth as possible because of the shifting away of the interface which results in the increase of Frank-Pryce stripes and the elimination of the distinct transition between Frank-Pryce stripes and EI stripes. The divergent orientation of CLC stripes can be quickly destroyed by surface energy and replaced by the parallel stripes if the potential energy of divergent orientation is not strong enough. The divergent orientation of stripes can be kept only if the potential energy is strong enough to compete with surface anchoring and

a recovered divergent orientation is shown in Figure 6.7(d) iii-v.

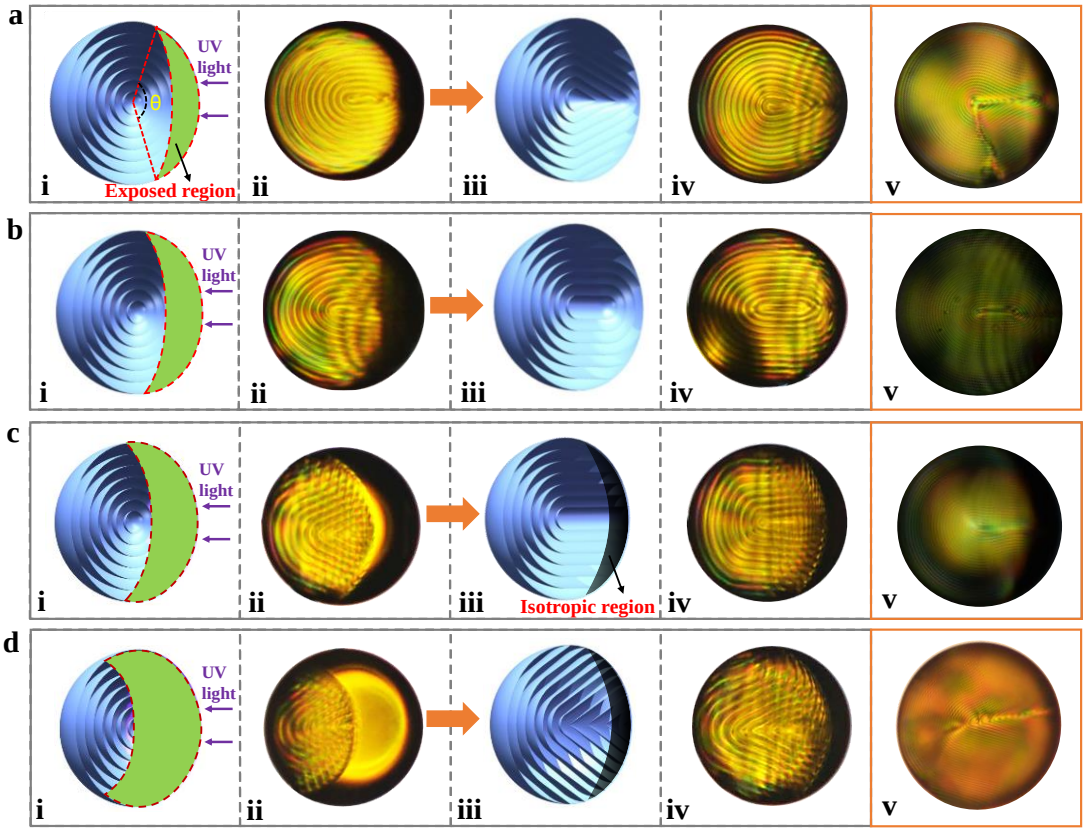

Figure 6.7 The process of topological changes of CLC droplets triggered by the phase transition. The exposed time and region are increasing gradually from (a) to (d). (i) the 3D presentation of the phase transition region; (ii) the images of the droplet corresponding to (i); (iii) the 3D figure of the final recovered structure; (iv) the images of the droplet with a lower chirality corresponding to (iii); (v) the images of the droplet with a higher chirality corresponding to (iii). The insets show that the optical rings on the surfaces are resulted from the periodic structural deviation from perfect Frank-Pryce structure. The 3D images are made through Cinema4D.

When the UV light is turned off, the iso-CLC interface stops the progress immediately then the backward shift starts. The CLC stripes grow along with the backward shift of the interface. The recovered CLC stripes from isotropic phase are affected by the interplay of surface energy, iso-CLC interface energy, and elastic energy. Here the influence of planar surface energy is greatly decreased by the addition of Frank-Pryce structure in aqueous solution. And both the interface energy and elastic energy are mainly affected by the progress of light driven phase transition. In this way, the architectures of CLC

droplets can be simply controlled by terminating the UV illumination at a particular stage of phase transition. Figure 6.7 shows four different conditions of turning off the UV light. Figure 6.8(a) shows the condition that the UV light is turned off at an early state. The exposure time is increasing gradually from Figure 6.8(a) to (d). The advance of the interface stretches the inner CLC stripes to be perpendicular to the interface and such an arrangement is kept during the backward shift of the interface. The final recovered EI stripes in CLC droplets can be even perpendicular to the droplet surface. All the four recovered CLC droplets show optical rings on their surface which indicates that the recovered droplets have similar surface structure regardless of their internal architectures. And the optical rings indicate a periodic structural deviation from Fran-Pryce structure since the surface of Frank-Pryce structure should be smooth.

A simple diffusion model is employed here to explain the steady shift of the iso-CLC interface. The isotropic phase is decided by the concentration of cis azo-LC. The concentration of the cis azo-LC at the iso-CLC interface is exactly the threshold for the phase transition. The diffusion of cis azo-LC occurs since the concentration of cis azo-LC in isotropic phase is higher than that in CLC. The diffusion decreases the concentration of cis azo-LC in the isotropic phase, especially the part near the interface which results in the concentration of cis azo-LC is lower than the threshold and the phase transition from isotropic phase to CLC. The crystallization of CLC in the isotropic phase can also be triggered by the photoisomerization of azo-LC from cis-state to trans-state induced by green light. However, the CLC stripes induced by the green light are randomly aligned, which decreases the controllability for the topology reconstruction in CLC droplets. The intensity of green light is kept low in experiments to avoid the green light-driven crystallization of CLC.

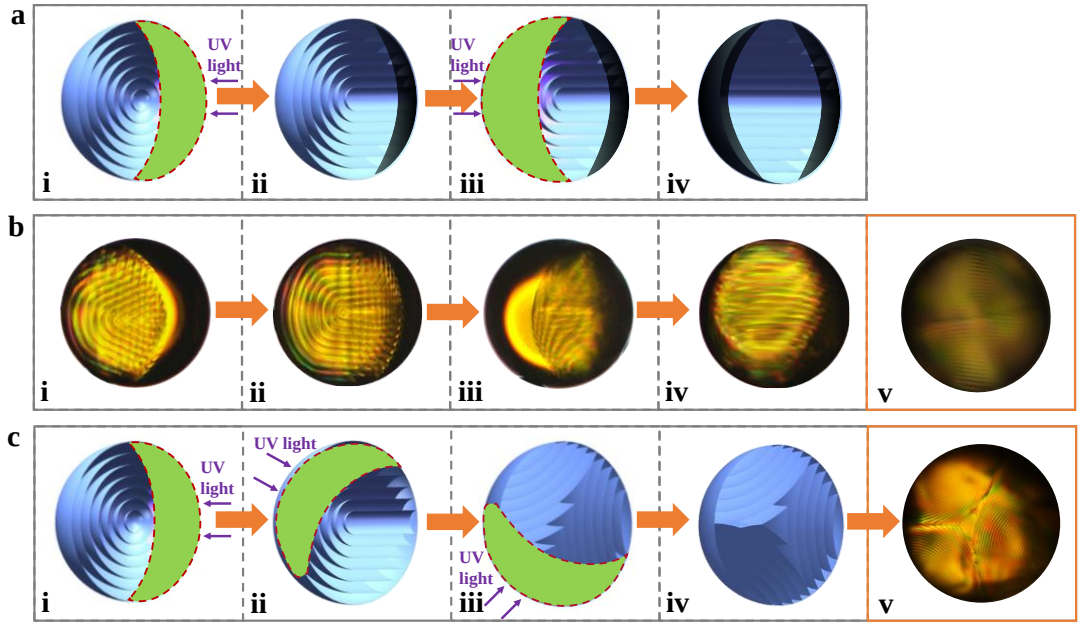

Figure 6.8 The schematic diagram of two ways for the recovery of CLC droplets corresponding to different numbers of UV light to induce the transformation from different direction. (a) CLC droplet is exposed to two UV light from opposite direction step by step. The first exposure directs CLC droplet to form parallel stripes on half of the droplet closed to the UV light. The second exposure directs CLC droplet to form completely parallel stripes. (b) The real droplet corresponding to each step in (a). The final structure of the droplet with a lower chirality and higher chirality are shown as iv and v separately. (c) CLC droplet is exposed to three UV light from the direction of the circular external triangle step by step. The black areas in pictures may have many defects because of the competition between elastic energy and surface energy.

Besides illuminating CLC droplets in one direction, CLC droplets can also be exposed in two directions. The bi-directional exposure can be carried simultaneously or sequentially. In our experiments, the two UV exposures are employed step by step on the CLC droplet (Figure 6.8). Figure 6.8(a) and (b) show schematic illustrations and experimentally obtained photo images of the bi-directional exposure, respectively. The CLC droplet is first exposed to one UV light to produce an iso-CLC interface before the droplet center, which stretches CLC stripes towards the interface [Figure 6.8(a & b) i]. After turning off the UV light, parallel CLC stripes are formed in the exposure area [Figure 6.8(a & b) ii]. The parallel stripes are quite stable because the surface anchoring is not strong enough to surmount the repulsion from the merge of CLC stripes. Then the same exposure but from the opposite direction is

applied to the CLC droplet to induce the parallel stripes [Figure 6.8(a & b) iv] from Frank-Pryce stripes [Figure 6.8(a & b) iii]. It is noticed that a similar topological structure of CLC droplet also can be formed by M3 with higher chirality and smaller pitch, as shown in Figure 6.8(b) v.

Tri-directional exposure with a 120° angle between the three exposures in the same plane induced CLC droplets (using M3) also shows another new topological structure, Figure 6.8(c). The schematic illustration of transformation process is shown in Figure 6.8(c) i-iv, where three exposures of UV light are employed step by step on a CLC droplet, leading to a hyperbolic triangle structure with central point singularity and three-fold symmetry [Figure 6.8(c) v].

6.6 Summary

In this chapter, Photo-responsive azo-LC doped CLC droplets were manipulated by irradiation of UV light to form novel topological configuration of CLC droplets with stable 3D structure through phase transition of liquid crystals. Besides, iso-CLC interfaces with different shapes are created by tuning the strength of the planar surface anchoring. The orientations of CLC stripes induced by the interfaces affect the structure reconstruction of CLC droplets after turning off the UV light. The competition of the elastic energy and surface energy of CLC droplets leads to the formation of the new topological configurations. CLC droplets with several novel architectures are demonstrated such as closed-ring structures of cone-shaped center and concentric ellipses center, and open-ring structures under uni-directional illumination of UV light, as well as structures with parallel CLC stripes center and with central point singularity under multi-directional illumination of UV light. CLC droplets with metastable topological structures offer them unique properties which have potential use in fields of biosensors, soft photonics, and functional materials [26].

Although not discussed in this paper, the light-driven phase transition can

also be used to manipulate the defects in CLC droplets such as change the shape or position of the line defect. The defects are important properties of LC systems [24]. The UV exposure can be further designed including confining the exposed area on CLC droplets and using multidirectional UV light. Which may produce CLC droplets with complex structures. What's more, the light-driven phase transition can be employed in confined LC systems of other shapes to change the competition of elastic energy and surface energy.

References

1. Xu, F.; Crooker, P. P. Chiral nematic droplets with parallel surface anchoring. *Phys. Rev. E* **1997,** 56, 6853–6860.
2. Bezić, J.; Žumer, S. Structures of the cholesteric liquid crystal droplets with parallel surface anchoring. *Liq. Cryst.* **1992,** 11, 593–619.
3. Tran, L.; Kim, H. N.; Li, N.; Yang, S.; Stebe, K. J.; Kamien, R. D.; Haase, M. F. Shaping nanoparticle fingerprints at the interface of cholesteric droplets. *Sci. Adv.* **2018,** 4, eaat8597.
4. Lee, H. G.; Munir, S.; Park, S. Y. Cholesteric Liquid Crystal Droplets for Biosensors. *ACS Appl. Mater. Inter.* **2016,** 8, 26407–26417.
5. Franklin, D.; Ueltschi, T.; Carlini, A.; Yao, S.; Reeder, J.; Richards, B.; Duyne, R. P. V.; Rogers, J. Bioresorbable microdroplet lasers as injectable systems for transient thermal sensing and modulation. *ACS Nano* **2021**, 15, 2327-2339.
6. Tran, L.; Lavrentovich, M. O.; Durey, G.; Darmon, A.; Haase, M. F.; Li, N.; Lee, D.; Stebe, K. J.; Kamien, R. D.; Leon, T. L. Change in Stripes for Cholesteric Shells via Anchoring in Moderation. *Phys. Rev. X* **2017,** 7, 041029.
7. Dubtsov, A. V.; Pasechnik, S. V.; Shmeliova, D. V.; Kralj, S. Light and phospholipid driven structural transitions in nematic microdroplets. *Appl. Phys. Lett.* **2014,** 105, 151606.
8. Wang, L.; Chen, D.; Gutierrez-Cuevas, K. G.; Bisoyi, H. K.; Fan, J.; Zola, R. S.; Li, G.; Urbas, A. M.; Bunning, T. J.; Weitz, D. A.; Li, Q. Optically reconfigurable chiral microspheres of self-organized helical superstructures with handedness inversion. *Mater. Horiz.* **2017**, 4, 1190–1195.
9. Noh, J.; Liang, H. L.; Olenik, I. D.; Lagerwall, J. P. F. Tuneable multicoloured patterns from photonic cross-communication between cholesteric liquid crystal droplets. *J. Mater. Chem. C* **2014,** 2, 806–810.
10. Seo, H. J.; Lee, S. S.; Noh, J.; Ka, J. W.; Won, J. C.; Park, C.; Kim, S. H.; Kim, Y. H. Robust photonic microparticles comprising cholesteric liquid crystals for anti-forgery materials. *J. Mater. Chem. C* **2017,** 5, 7567–7573.

11. Rahimi, M.; Roberts, T. F.; Pérez, J. C. A.; Wang, X.; Bukusoglu, E.; Abbott, N. L.; Pablo, J. J. Nanoparticle self-assembly at the interface of liquid crystal droplets. *Proc. Natl. Acad. Sci. USA* **2015,** 112, 5297–5302.
12. Cipparrone, G.; Mazzulla, A.; Pane, A.; Hernandez, R. J.; Bartolino, R. Chiral self-assembled solid microspheres: A novel multifunctional microphotonic Device. *Adv. Mater.* **2011,** 23, 5773–5778.
13. Hands, P.J.W.; Gardiner, D.J.; Morris, S.M.; Mowatt, C.; Wilkinson, T.D.; Coles, H.J. Band-edge and random lasing in paintable liquid crystal emulsions. *Appl. Phys. Lett.* **2011**, 98, 141102.
14. Gardiner, D.J.; Hsiao, W.-K.; Morris, S.M.; Hands, P.J.W.; Wilkinson, T.D.; Hutchings, I.M.; Coles H.J. Printed photonic arrays from self-organized chiral nematic liquid crystals. *Soft Matter*, **2012**, 8, 9977.
15. Paterson, D. A.; Du, X. X.; Bao, P.; Parry, A. A.; Peyman, S. A.; Sandoe, J. A. T.; Evans, S. D.; Luo, D.; Bushby, R. J.; Jones, J. C.; Gleeson, H. F. Chiral nematic liquid crystal droplets as a basis for sensor systems, *Mol. Syst. Des. Eng.* **2022**, 7, 607-621.
16. Zhou, Y.; Bukusoglu, E.; González, J. A. M.; Rahimi, M.; Roberts, T. F.; Zhang, R.; Wang, X.; Abbott, N. L.; Pablo, J. J. Structural Transitions in Cholesteric Liquid Crystal Droplets. *ACS Nano,* **2016,** 10, 6484–6490.
17. Shechter, J.; Atzin, N.; Mozaffari, A.; Zhang, R.; Ross, J. L. Direct observation of liquid crystal droplet configurational transitions using optical tweezers. *Langmuir* **2020**, 36, 7074-7082.
18. Ramou, E.; Rebordao, G.; Palma, S. I. C. J.; Roque, A. C. A. Stable and oriented liquid crystal droplets stabilized by imidazolium ionic liquids. Molecules 2021, 26, 6044.
19. Yoshioka, J.; Araoka, F. Topology-dependent self-structure mediation and efficient energy conversion in heat-flux-driven rotors of cholesteric droplets. *Nat. Commun.* **2018,** 9, 432.
20. Kolacz, J.; Wei, Q. H. Self-Localized liquid crystal micro-droplet arrays on chemically patterned surfaces. *Crystals* **2022**, 12, 13.

21. Durey, G.; Ishii, Y.; Lopez-Leon, T. Temperature-driven anchoring transitions at liquid crystal / water interfaces. *Langmuir* **2020**, 36, 9368-9376.
22. Orlova, T.; Aßhoff, S. J.; Yamaguchi, T.; Katsonis, N.; Brasselet, E. Creation and manipulation of topological states in chiral nematic microspheres. *Nat. Commun.* **2015,** 6, 7603.
23. Swisher, R. R. The cholesteric-nematic transition in droplets subjected to electric fields. *Liq. Cryst.* **1999,** 26, 57–62.
24. Parshin, A. M. Structural stability of nematic liquid crystal droplets in the light of the catastrophe theory. *Mod. Phys. Lett. B* **2019**, 33, 1950434.
25. Ignés-Mullol, J.; Mora, M.; Martínez-Prat, B.; Vélez-Cerón, I.; Herrera, R. S.; Sagués, F. Stable and metastable patterns in chromonic nematic liquid crystal droplets forced with static and dynamic magnetic fields. *Crystals*, **2020**, 10, 138.
26. Wang, X.; Bukusoglu, E.; Abbott, N. L. A Practical Guide to the Preparation of Liquid Crystal-Templated Microparticles. *Chem. Mater.* **2017,** 29, 53–61.

Chapter 7 Sensors Based on the Liquid crystal and Aggregation Induced Emission materials that detecting the lead ions

Lead ions, as major heavy metals in environmental pollutants, are harmful to human health and can lead to problems such as muscle paralysis, anemia, memory loss, and mental health concerns. The existing analytical methods usually require large or expensive equipment with sophisticated operators, complicated operation processes, and time-consuming sample pretreatments. In this chapter, we show a new fluorescence sensor for detecting lead ions derived from liquid crystals doped with an aggregation-induced emission luminogen. The mechanism is based on the variation of fluorescence intensity caused by the disturbance of an ordered liquid crystal configuration in the presence of Pb^{2+}, induced by DNAzyme and its catalytic cleavage. The proposed fluorescence sensor exhibits a low detection limit of 0.65 nM, which is 2 orders of magnitude lower than that previously reported in an optical sensor based on liquid crystals. The detection range of the Pb^{2+} fluorescence sensor is broad, from 20 nM to 100 μM, and it also selects lead ions from numerous metal ions exactly, resulting in a highly sensitive, highly selective, simple, and low-cost detection strategy of Pb^{2+} with potential applications in chemical and biological fields.

Much of the work contained in this chapter was published by Xiaoxue Du and Helen F. Gleeson, “A Fluorescence Sensor for Pb^{2+} Detection Based on Liquid Crystals and Aggregation-Induced Emission Luminogens”, *ACS Applied Materials & Interfaces*, 13(19), 2021 [1].

7.1 Introduction

Recently, liquid crystal (LC) based optical biochemical sensors [2-4] sensors have attracted considerable attention due to the extraordinary sensitivity of

chemical and physical properties at a bounding interface that can transduce molecular events to a bulk response [5-7]. LC based optical sensors for the detection of protein and cancer cells [8], polymer chemicals [9], bacteria [10], viruses [11], and mercuric ions [12] have been designed with features including low-cost, simplicity and rapid responses. Moreover, many studies have reported DNA functionalized sensing systems, including “8-17” DNAzyme [13, 14], quadruplex DNAzyme [15], and GR-5 DNAzyme [16, 17]. Further, a novel naked-eye optical sensor based on LCs decorated with DNAzyme for the detection of lead ions was recently reported by our group [13]. The LC sensor described in that work exhibits a particularly wide range detection of lead ions (50 nM ~ 500 μM). However, the limit of detection is approximately 36.8 nM, which is unsatisfactory. Therefore, it is highly desirable to improve the limit of detection of the LC sensor for Pb^{2+} while maintaining the broad detection range.

In this chapter, we report a liquid crystal fluorescence sensor developed for Pb^{2+} detection derived from liquid crystals doped with an aggregation-induced emission (AIE) luminogen. The mechanism is based on the variation of the fluorescence intensity caused by the disturbance of the liquid crystal configuration due to the existence of Pb^{2+}, induced by DNAzyme and its catalytic cleavage. The proposed fluorescence sensor reveals a low detection limit as well as a broad detection range, leading to a highly sensitive, highly selective, simple, and low-cost detection strategy for Pb^{2+}. This device can be applied in environmental monitoring, industry process monitoring, and clinical toxicology with great potential.

7.2 Materials and equipments

H_2O_2, H_2SO_4, dimethyloctadecyl [3-(trimethoxysilyl) propyl] ammonium chloride (DMOAP), (3-Aminopropyl) triethoxysilane (APTES), C_2H_5OH, glutaral (GA), dodecyl trimethyl ammonium bromide (DTAB), $Pb(NO_3)_2$, $CuCl_2$,

$ZnCl_2$, $AgNO_3$, $CdCl_2$, $MgCl_2$, $MnCl_2$ and KCl were purchased from Sigma-Aldrich (St. Louis, USA). The nematic liquid crystals 4-cyano-4'-pentylbiphenyl (5CB) was purchased from HCCH (Jiangsu China). Deoxyribozyme (DNAzyme) is a catalytic DNA sequence in the cooperative presence of metal ions. It is highly selective to metal ions. The DNAzyme used here were obtained from Shenggong Bioengineering (Shanghai, China), which is highly selective to Pb^{2+}. The lead ion will insert into the U-shaped ring and shear the strand at the "rA" site (Figure 7.1 b). The catalytic cleavage destroys the order of the original system, disturbing the orientation of both the liquid crystal and AIEgens, resulting in a darker fluorescence in the sensor. Dongsheng Glass (Taizhou, China) provided the glass slides (Sail brand). The TPE-PPE (tetraphenylethylene-propylphenylethyne), as the AIE material here, was supplied by Beihang University. The chemical structures of 5CB, DTAB, APTES, GA, TPE-PPE and DMOAP are shown in Figure 7.1 (a).

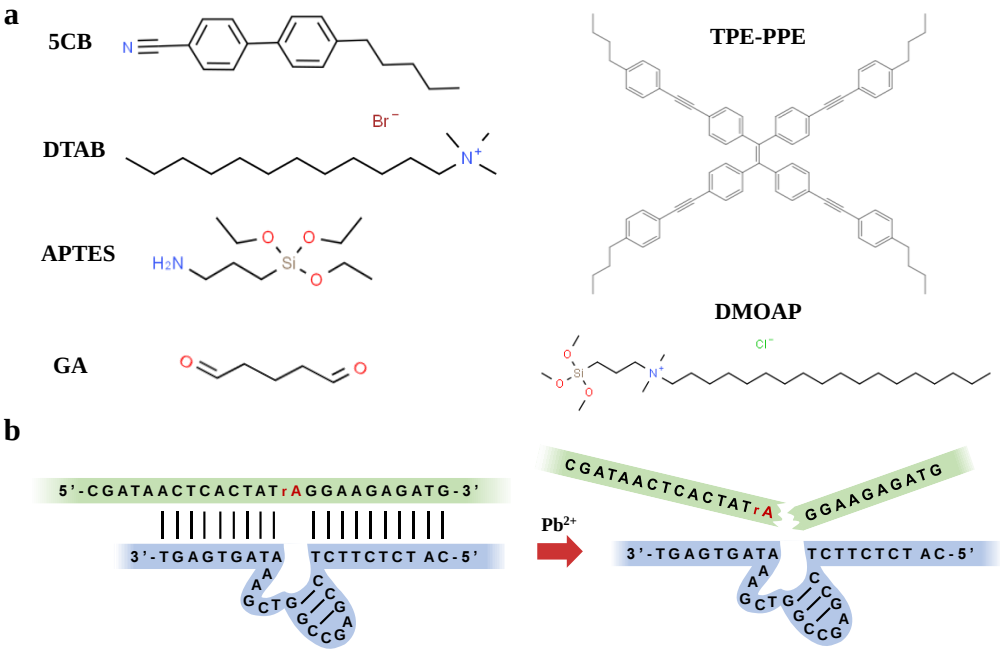

Figure 7.1 (a) Chemical structures of 5CB, DTAB, APTES, GA, TPE-PPE and DMOAP for lead ion fluorescence sensor. (b) Schematic illustration of catalytically cleave of complementary DNA molecules.

The samples' images were captured by optical microscope (Eclips Ti200, Nikon). The fluorescence intensity was obtained from processing the images,

which were captured by a charge coupled device (CCD) camera (Nikon Ds-Ri2), where the gamma correction coefficient of the CCD was 1 and the integration time was 200 ms. The fluorescence spectrum was obtained by microspectrophotometer (CRAIC technologies Inc.). The Milli-Q water purification system (Millipore, Bedford, MA) was operated to prepare all aqueous solutions with deionized water (DI water).

7.3 Experimental details

7.3.1 The pretreatment of the substrates

The process of substrate's pretreatment and anchoring operations are the same as those in previous work on the optical sensor based on liquid crystal and DNAzyme [13]. More preparation details can be checked in [13]. The substrate was treated with sufficient piranha solution and then washed with plenty of DI water. Then it was dried with N_2 and soaked in an ethanol solution containing DMOAP and APTES. The anchoring of 5CB was indeed influenced by the DMOAP. For this sensor, the DMOAP was bonded to the substrate because of the covalent Si-O-Si bonds. The carbon chain units on the other side of the "Si" kept vertical and induced the liquid crystals to vertically align on glass substrate. The APTES molecules, which has terminal amino groups capable of attracting anionic complementary DNA strands (base sequence and structure corresponded to Figure 7.1 b). The strands consisted of a catalytic strand and its combined strand, attaching on the glass substrate through covalent bonds (Si-O-Si). GA was subsequently applied to the surface and dried. Then, the catalytic strands (200 μM) and combined strands (200 μM) were combined to this system. GA acted as the intermediate through the amino groups between APTES and DNA strand. Next, the unbonded DNA strands of sample were washed by DI water. Transmission electron microscopy (TEM) grids (copper mesh) were then put on the glass substrate.

After that, 1 μL of solution mixed with 5CB (99.9 wt%) and TPE-PPE (0.1 wt%) was distributed onto the grid. Finally, the TEM grid was placed in DTAB environment. The electrostatic interaction linked DTAB molecules to the DNA and this led to a good dissolution of DNA through a self-assembled monolayer at the LC/aqueous interface. On the bottom glass substrate, the DMOAP was applied to help the LC molecules be in a homeotropic alignment. On the top interface of LC and aqueous solution, the DTAB also aligned LC molecules vertically. Based on both vertical alignments of DMOAP and DTAB, a homeotropic configuration of the LC was achieved [14]. The DNAzyme is a kind of 8-17 DNAzyme, which is a mature and popular choice that corresponding to lead ion [15]. The DNAzyme would be disassembled because of catalytic cleavage at the “rA” site of DNA molecules, as shown in Figure 7.1(b). The thickness of the TEM grid was 10 μm and all experiments were undertaken at room temperature (25 ˚C). The orientation of AIE featured TPE-PPE obtained a perpendicular orientation in the homeotropic LC mixture [19]. It is worth noticing that the orientation of AIE-featured TPE-PPE was induced by the orientation of the nematic liquid crystal 5CB here. The liquid crystal molecules and AIE molecules were anchored by these vertical long chains formed by DMOAPAPTES-GA-DNA-DTAB on the glass substrate [13, 14]. The homeotropic configuration of LC/AIE was formed through self-assembly property of LC molecules.

7.3.2 The preparation of the sensing system

In our experiment, the sensor was placed under an optical microscope to capture the fluorescence signal, and was stimulated by an ultraviolet (UV) light (365 nm). Figure 7.2 depicts the process of Pb^{2+} sensing in the AIE doped LC optical sensor. The AIE-featured TPE-PPE molecules aggregate in the nematic liquid crystal mixture at a concentration of 0.1 wt% in our experiment, which leads to a significantly high fluorescence efficiency [19]. According to

quantum chemistry calculations, the emission dipole moment of TPE-PPE is parallel to the double bond [20]. The dipole moment along the short axis direction is greater than that along the long axis direction of TPE-PPE molecule, leading to a stronger fluorescence of molecules for a homeotropic configuration when observed using optical microscopy [21]. Initially, the liquid crystal 5CB molecules (and DNA strands) possess a vertical alignment configuration (homeotropic configuration) on the glass substrate with DMOAP, which forms homeotropic configuration and induces vertically alignment of AIE-featured TPE-PPE (as shown in the left part of Figure 7.2). The corresponding florescence intensity of sample under UV illumination is relatively high. In the presence of lead ions, the complementary DNA strand disassembles based on catalytic cleavage of DNA, which disturbs the vertical alignment of LC (5CB) as well as AIE-featured TPE-PPE (as shown in the right part of Figure 7.2), resulting in a relatively low florescence intensity of sample under UV illumination. It is worth noticing that the orientation of AIE-featured TPE-PPE is induced by the orientation of the nematic liquid crystal 5CB here, thus leading to the fluorescent intensity change, which is different from the ordinary AIE where the fluorescent intensity change is due to the aggregation of AIE molecules.

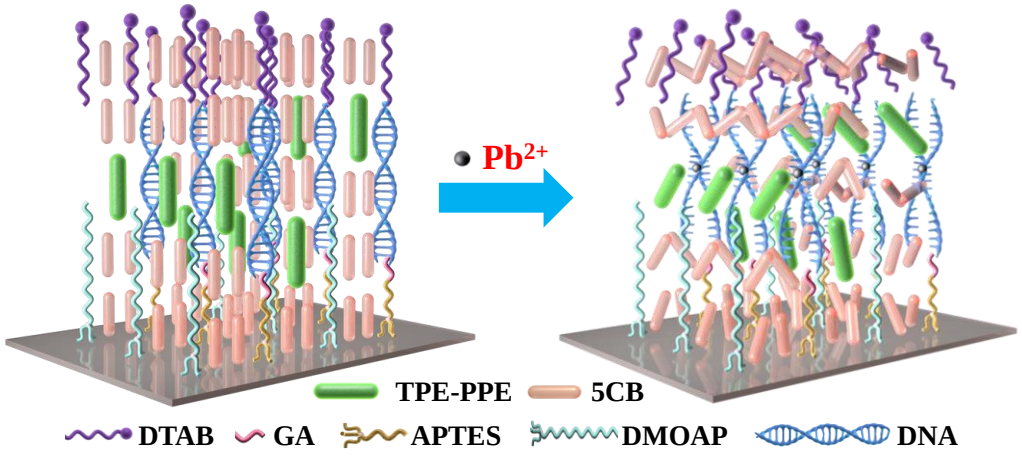

Figure 7.2 Schematic illustration of the sensing system on the basis of liquid crystals doped with AIE for detecting lead ions.

7.4 Results and discussion

7.4.1 The promotion of the concentration of DTAB

The concentration of DTAB is critical for liquid crystal alignment with DNA molecules in the initial homeotropic configuration. The fluorescence image of the Pb^{2+} sensor under illumination by UV light (365 nm, 5.6 mW/cm^2) is shown in Figure 7.3, for concentrations of DTAB varying from 0 μM to 50 mM without the presence of Pb^{2+}. It can be seen that, without DTAB (0 μM) the fluorescence intensity of sample is low, leading to a relatively dark fluorescent image (Figure 7.3 a). The brightness increases with increasing concentration of DTAB (Figures 7.3 b-d), suggesting that more AIEgens are anchored on the glass slide vertically. The fluorescence image tends to saturate when DTAB's concentration reaches 10 mM, above which there is no further significant change in the brightness of sample. The saturation of the alignment effect of DTAB is accompanied by the anion-cation balance originating from the cationic in DTAB and anionic in the complementary DNA strand. In our following experiments, the optimum concentration of DTAB was chosen to be 10 mM. Figure 7.3 (e) plots the relationship of DTAB concentration and the fluorescence intensity. The fluorescence intensity here is a mean value, which is obtained by calculating the ratio of integrated density to the area.

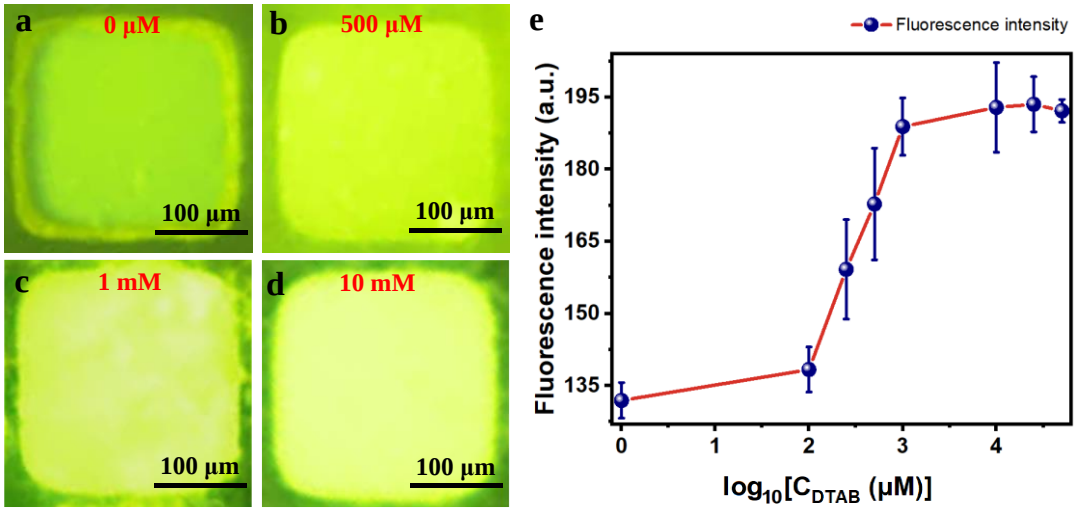

Figure 7.3 Fluorescence image of the lead ion sensor sample viewed by optical microscopy with the concentration of DTAB varying from (a) 0 μM, (b) 500 μM, (c) 1 mM, (d) 10 mM, without the presence of Pb^{2+}. (e) The relationship of DTAB concentration and the fluorescence intensity. The scale bar is 100 μM.

7.4.2 The images of the sensing results

The influence of lead ions' concentrations on the luminance of sensor's fluorescence was studied to provide a quantitative analysis. Figures 7.4 (a-h) show fluorescence images of the Pb^{2+} sensor under illumination by UV light at am intensity of 6.7 mW/cm^2, for varying concentrations of Pb^{2+} (from $Pb(NO_3)_2$) solution (0 nM - 100 μM). The initial fluorescence image, without Pb^{2+}, is shown in Figure 7.4 (a), demonstrating a highly brightness. Herein, the AIE molecules were anchored on the glass slide vertically with the homeotropic configuration of LC molecules. During the process of adding Pb^{2+}, the DNA molecules are catalytically cleaved, disturbing the orientation of both the liquid crystal and AIEgens, resulting in a darker fluorescence in the sensor. The concentration of added Pb^{2+} determined the amount of cleavage of the DNA strands; increasing the Pb^{2+} concentration caused more DNA strands to be cleaved, leading to a darker sensor. The response time is counted with starting time of adding Pb^{2+} on the sensor and ending time of viewing stable fluorescence in optical microscope. The response time of Pb^{2+} sensor was less than 20 seconds. Figure 7.4 (i) plots the absorption spectra of our sensor

before and after adding 1 μM Pb^{2+}. It is clear that there is no obvious difference between the two spectra. Figure 7.4 (j) shows the emission spectra of our sensor before and after 1 μM Pb^{2+} added, where the central wavelength is unchanged while the intensity dramatically decreases after addition of 1 μM Pb^{2+}.

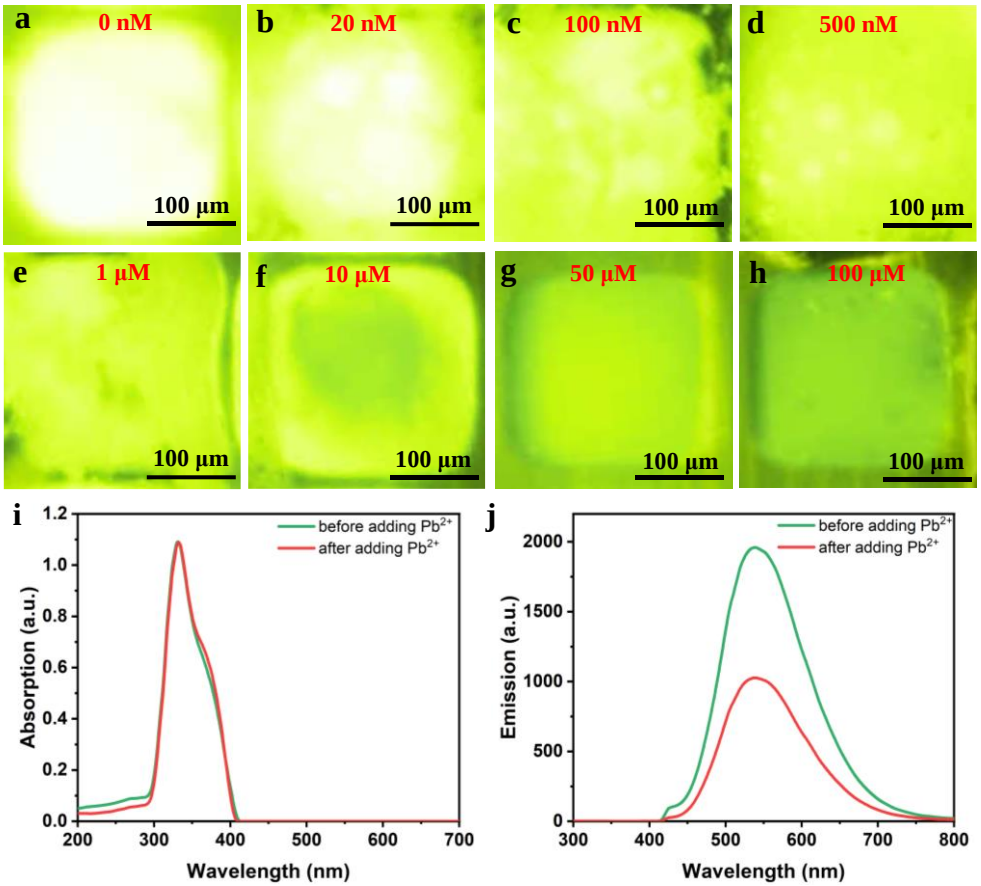

Figure 7.4 The fluorescence images of the sensor observed using a microscope where the concentration of Pb^{2+} is (a) 0 nM, (b) 20 nM, (c) 100 nM, (d) 500 nM, (e) 1 μM, (f) 10 μM, (g) 50 μM, and (h) 100 μM. The scale bar is 100 μm. (i) Absorption spectrum of our sensor before and after adding 1 μM Pb^{2+}. (j) Emission spectrum of our sensor before and after adding 1 μM Pb^{2+}.

7.4.3 The sensitivity of the sensor

The relationship of Pb^{2+} concentration and the fluorescence intensity of the sensor was plotted as Figure 7.5. Within the detection range, from 20 nM to 100 μM, the fluorescence intensity varies from very bright to relatively dark. This sensor is relative stable and not very sensitive to the environmental

temperature within 15 ˚C ~ 30 ˚C. After processing the images from multiple samples under the same conditions, the average intensity, I, and standard deviation were determined for each Pb^{2+} concentration was measured and fitted to the relationship

$$I = -26.98(\ln C_{Pb^{2+}}) + 237.1, \quad (7\text{-}1)$$

which has a correlation coefficient of $R^2 = 0.9918$ ($C_{Pb^{2+}}$ is the concentration of Pb^{2+} in nM).

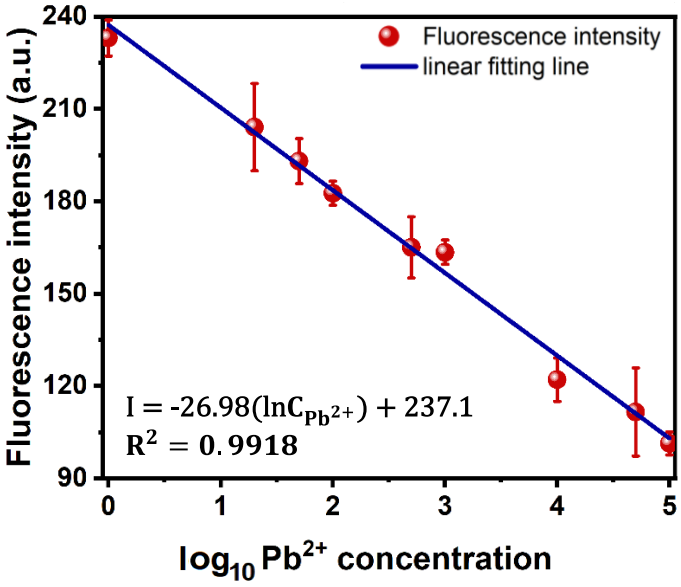

Figure 7.5 The relationship of Pb^{2+} concentration and the fluorescence intensity of sensor.

According to the theory of Martins and Naes [22], the limit of detection (LOD) with the rule of 3σ/slope (σ refers to the standard deviation of the background obtained from multiple measurements in blank samples) can be worked out as 0.65 nM, which is two orders of magnitude lower than previously reported result of 36.8 nM from liquid crystal based Pb^{2+} optical sensor [13]. It can compare with those of sensors based on organic dye and quantum dots (from 0.1 nM-0.6 nM) [23-25]. In addition, the detection range (20 nM-100 μM) of this proposed strategy is rather wider than those based on organic dyes (2-50 nM) [23], semiconductor quantum dots (0.1-10 nM) [24], graphene quantum dots/graphene oxide (9.9-435.0 nM) [25], and graphene

quantum dots/gold nanoparticles (50 nM-4 μM) [26]. The comparison of these related Pb^{2+} sensors are shown in Table 7.1. It is difficult for existing detection methods to balance limit of detection and linear detection range. Otherwise, the cost of materials and fabrication will be high. The broad detection range with high sensitivity of our sensor is critical for its practical applications.

Table 7.1 The comparison of related Pb^{2+} sensors

Methods	**Materials**	**LOD**	**Linear range**	**References**
Fluorescent	GR-5 DNAzyme, nanoparticles	1.108 nM	0-1 nM	Ref 16
Fluorescent	G-quadruplex DNA, graphene oxide	0.4 nM	2-50 nM	Ref 22
Fluorescent	CdSe/ZnS quantum dots, graphene oxide	0.09 nM	0.1-10 nM	Ref 23
Fluorescent	Graphene quantum dots-aptamer probe, graphene oxide	0.6 nM	9.9-435.0 nM	Ref 24
Fluorescent	Graphene quantum dots, gold nanoparticles	16.7 nM	50 nM-4 μM	Ref 25
Gray-value	8-17 DNAzyme, LC	36.8 nM	50 nM-500 μM	Ref 12
Fluorescent	8-17 DNAzyme, LC, AIE	0.65 nM	20 nM-100 μM	Our work

7.4.4 The selectivity of the sensor

The selectivity is also a critical indicator for sensor. Figure 7.6 plots the performance of the sensor at 1 μM Pb^{2+} and 100 μM Cu^{2+}, Zn^{2+}, Ag^{+}, Cd^{2+}, Mg^{2+}, Mn^{2+} and K^{+}. The initial and final fluorescence is denoted by F_i and F_f, respectively. The ratio of the change in fluorescence intensity is determined by

$$\frac{F_i - F_f}{F_i} . \tag{7-2}$$

It is obviously that the change of fluorescence intensity is significant on adding 1 μM Pb^{2+} to the sensor, while effectively no change occurs in the

presence of other metal ions with the concentration of 100 μM. About three times the value of influence of lead ions was achieved in comparison to other metal ions. The results indicate that only Pb^{2+} ions can cleave the DNAzyme strands, thus disrupting the homeotropic configuration of the LC and the AIE materials TPE-PPE. This fluorescence sensor shows a negligible response to Cu^{2+}, Zn^{2+}, Ag^{+}, Cd^{2+}, Mg^{2+}, Mn^{2+} and K^{+} under similar condition. The "rA" site of "8-17" DNAzyme only binds specifically to Pb^{2+}, leading to the sensor's high selectivity. Due to the reason that double stranded DNA with C or G bases in addition of sufficient Ag^{+} can form Ag^{+}-mediated guanine pairing [27], the anchoring of the sensing system would be affected slightly. Therefore, the Ag^{+} had a higher fluorescence changing ratio compared to other ions.

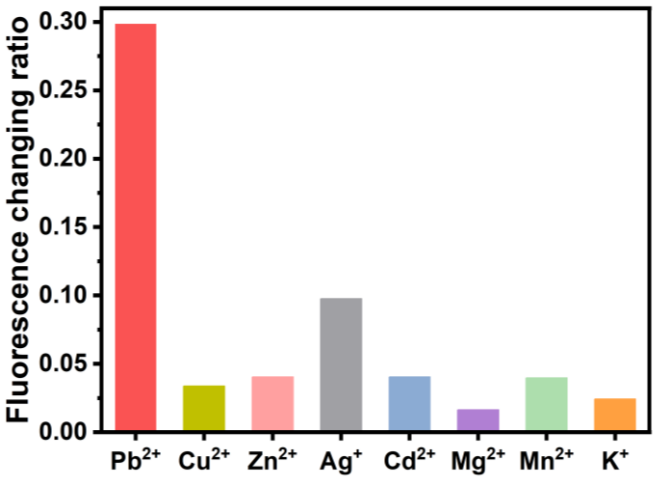

Figure 7.6 Selectivity of the fluorescence sensor under existing of 100 μM Cu^{2+}, Zn^{2+}, Ag^{+}, Cd^{2+}, Mg^{2+}, Mn^{2+}, K^{+} and 1 μM Pb^{2+}.

7.5 Summary

In this study, a fluorescence sensor for detecting lead ions on the basis of AIE-doped liquid crystals has been demonstrated. A disordered configuration of the liquid crystal sample doped with AIE luminogen leads to reduction in the fluorescence intensity, which is led by catalytic cracking of complementary DNA strand in existing of Pb^{2+}. The proposed fluorescence sensor possesses a low LOD of 0.65 nM, which is two orders of magnitude lower than that from previously reported LC optical sensor. The detection range of the Pb^{2+}

fluorescence sensor is broad, from 20 nM to 100 μM. It also indicates that this sensor can select Pb^{2+} from many other metal ions correctly, resulting in a highly sensitive, highly selective, simple and low-cost detection strategy for Pb^{2+} with potential applications in chemical and biological fields. This LC fluorescence sensor can provide an inspiring platform for detection by varying the decorated molecules, such as detecting other heavy metal ions and antigens.

References

1. Du, X. X.; Liu, Y. J.; Wang, F.; Zhao, D. Y.; Gleeson, H. F.; Luo, D. A Fluorescence Sensor for Pb^{2+} Detection Based on Liquid Crystals and Aggregation-Induced Emission Luminogens. *ACS Appl. Mater. Interfaces* **2021**; 13, 22361–22367.

2. Wang, X.; Miller, D. S.; Bukusoglu, E.; de Pablo, J. J.; Abbott, N. L. Topological Defects in Liquid Crystals as Templates for Molecular Self-Assembly. *Nat. Mater.* **2016,** 15, 106–112.

3. Iino, H.; Usui, T.; Hanna, J. Liquid Crystals for Organic Thin-Film Transistors. *Nat. Commun.* **2015,** 6, 6828.

4. Sivakumar, S.; Wark, K. L.; Gupta, J. K.; Abbott, N. L.; Caruso, F. Liquid Crystal Emulsions as the Basis of Biological Sensors for the Optical Detection of Bacteria and Viruses. *Adv. Funct. Mater.* **2009,** 19, 2260–2265.

5. Shah, R. R.; Abbott, N. L. Principles for Measurement of Chemical Exposure Based on Recognition-Driven Anchoring Transitions in Liquid Crystals. *Science* **2001,** 293, 1296–1299.

6. Price, A. D.; Schwartz, D. K. DNA Hybridization-Induced Reorientation of Liquid Crystal Anchoring at the Nematic Liquid Crystal/Aqueous Interface. *J. Am. Chem. Soc.* **2008,** 130, 8188–8194.

7. He, Z. Q.; Tan, G. J.; Chanda, D.; Wu, S. T. Novel Liquid Crystal Photonic Devices Enabled by Two-photon Polymerization. *Opt. Express* **2019,** 27, 11472-11491.

8. Yoon, S. H.; Gupta, K. C.; Borah, J. S.; Park, S. Y.; Kim, Y. K.; Lee, J. H.; Kang, I. K. Folate Ligand Anchored Liquid Crystal Microdroplets Emulsion for in Vitro Detection of KB Cancer Cells. *Langmuir* **2014,** 30, 10668–10677.

9. Manda, R.; Dasari, V.; Sathyanarayana, P.; Rasna, M.; Paik, P.; Dhara, S. Possible Enhancement of Physical Properties of Nematic Liquid Crystals by Doping of Conducting Polymer Nanofibres. *Appl. Phys. Lett.* **2013,** 103, 141910.

10. Cadwell, K. D.; Alf, M. E.; Abbott, N. L. Infrared Spectroscopy of Competitive Interactions Between Liquid Crystals, Metal Salts, and Dimethyl Methylphosphonate at Surfaces. *J. Phys. Chem. B* **2006,** 110, 26081–26088.

11. Han, G. R.; Song, Y. J.; Jang, C. H. Label-Free Detection of Viruses on a Polymeric Surface Using Liquid Crystals. *Colloids Surf., B* **2014,** 116, 147–152.

12. Chen, C. H.; Lin, Y. C.; Chang, H. H.; Lee, A. S. Y. Ligand-Doped Liquid Crystal Sensor System for Detecting Mercuric Ion in Aqueous Solutions. *Anal. Chem.* **2015,** 87, 4546–4551.

13. Niu, X. F.; Liu, Y. J.; Wang, F.; Luo, D. Highly Sensitive and Selective Optical Sensor for Lead Ion Detection Based on Liquid Crystal Decorated with Dnazyme. *Opt. Express* **2019,** 27, 30421-30428.

14. Huang, Z. J.; Chen, J. M.; Luo, Z. W.; Wang, X. Q.; Duan, Y. X. Label-Free and Enzyme-Free Colorimetric Detection of Pb^{2+} Based on RNA-Cleavage and Annealing-Accelerated Hybridization Chain Reaction. *Anal. Chem.* **2019,** 91, 4806–4813.

15. Xiang, Y.; Tong, A.; Lu, Y. Abasic Site-containing DNAzyme and Aptamer for Label-free Fluorescent Detection of Pb^{2+} and Adenosine with High Sensitivity, Selectivity, and Tunable Dynamic Range. *J. Am. Chem. Soc.* **2009,** 131, 15352-15357.

16. Zhou, Y. Y.; Tang, L.; Zeng, G. M.; Zhang, C.; Zhang, Y.; Xie, X. Current Progress in Biosensors for Heavy Metal Ions Based on DNAzymes/DNA Molecules Functionalized Nanostructures: A review. *Sens. Actuators, B* **2016,** 223, 280-294.

17. Jia, M.; Lu, Y. F.; Wang, R. N.; Zhang, J. L.; Xu, C. H.; Wu, J. K. Extended GR-5 DNAzyme-based Autonomous Isothermal Cascade Machine: An Efficient and Sensitive One-tube Colorimetric Platform for Pb^{2+} Detection. *Sens. Actuators, B* **2020,** 304, 127366.1-127366.7.

18. Chu, L. T.; Leung, H. M.; Lo, P. K.; Chen, T. H. Visual Detection of Lead Ions Based on Nanoparticle-amplified Magnetophoresis and Mie Scattering. *Sens. Actuators, B* **2019,** 306, 127564.1-127564.8.

19. Zhao, D. Y.; Fan, F.; Cheng, J.; Zhang, Y. L.; Wong, K. S.; Chigrinov, V. G.; Kwok, H. S.; Guo, L.; Tang, B. Z. Light-Emitting Liquid Crystal Displays Based on an Aggregation-Induced Emission Luminogen. *Adv. Opt. Mater.* **2014,** 3, 199-202.

20. Zhao, D. Y.; Fan, F; Chigrinov, V. G.; Kwok, H. S; Tang, B. Z. Aggregate-Induced Emission in Light-Emitting Liquid Crystal Display Technology. J. Soc. Inf. Display **2015,** 23, 218-222.

21. Zhao, D. Y.; He, H. X.; Gu, X. G.; Wongm K. S.; Lam, J. W. Y.; Tang, B. Z. Circularly Polarized Luminescence and a Reflective Photoluminescent Chiral Nematic Liquid Crystal Display Based on an Aggregation-Induced Emission Luminogen. *Adv. Opt. Mater.* **2016,** 4, 534-539.

22. Martins, H.; Naes, T. Multivariate Calibration. Wiley, New York, **1989.**

23. Li, X.; Wang, G. K.; Ding, X.; Chen, Y. H.; Gou, Y. P.; Lu, Y. A Turn-on Fluorescent Sensor for Detection of Pb^{2+} Based on Graphene Oxide and G-quadruplex DNA. *Phys. Chem. Chem. Phys.* **2013,** 15, 12800–12804.

24. Li, M.; Zhou, X. J.; Guo, S. W.; Wu, N. Q. Detection of Lead (II) with a Turn-on Fluorescent Biosensor Based on Energy Transfer from CdSe/ZnS Quantum Dots to Graphene Oxide. *Biosens. Bioelectron.* **2013,** 43,69–74.

25. Qian, Z. S.; Shan, X. Y.; Chai, L. J.; Chen, J. R.; Feng, H. A. Fluorescent nanosensor Based on Graphene Quantum Dots-Aptamer Probe and Graphene Oxide Platform for Detection of Lead (II) Ion, *Biosens. Bioelectron.* **2015,** 68, 225–231.

26. Niu, X. F.; Zhong, Y. B.; Chen, R.; Wang, F.; Liu, Y. J.; Luo, D. A “Turn-on” Fluorescence Sensor for Pb^{2+} Detection Based on Graphene Quantum Dots and Gold Nanoparticles. *Sens. Actuators,* B **2018,** 255, 1577–1581.

27. Swasey, S. M.; Leal, L. E.; Lopez-Acevedo, O.; Pavlovich, J.; Gwinn, E. G. Silver (I) as DNA glue: Ag+-mediated Guanine Pairing Revealed by Removing Watson-Crick Constraints. Sci. Rep. 2015, 5, 10163.

Chapter 8 Force Sensing Actuators Based on Fluorescent Liquid Crystal Elastomers

In this chapter, a fluorescent sensor for force detection based on the liquid crystal elastomers have been investigated experimentally. The AIE-featured TPE-PPE molecules aggregate in the nematic liquid crystal mixture at a concentration of 0.1 wt% in our experiment. The mechanism is derived from the variation of the fluorescence intensity caused by the changes in the degree of aggregation due to stretching. When the external force applied, the fluorescent LCE will be stretched, leading to a reduction in the aggregation degree of TPE-PPE. So that the fluorescence intensity of the device will be weakened with a greater force, which enables a sensitive non-contact force measurement and provides a lot of potential applications in biosensors and interactive electronics.

8.1 Introduction

For a variety of applications, including human mobility tracking [1-2], rehabilitation/personalized health monitoring [3-4], human-machine interaction [5-6], strain sensors have drawn a lot of interest. Certainly, the size and detection range requirements for force sensors vary depending on the application fields. For the small sensor detecting micro force, for example a surgical instrument sensor or a yarn tension, the small size, high mechanical compliance, and good recoverability are necessary within the range of small force [7-9]. Several methods have been proposed for force sensing with the development of interactive electronics. Three basic sensing modalities are used for most existing force sensors in microelectromechanical systems (MEMS): resistive, piezoelectric, and capacitive [10-12]. By causing variations in resistance, resistive sensors can identify mechanical stimuli [10]. While measuring applied forces, piezoelectric sensors produce voltage [11]. As the

distance between opposing plates shrinks or the permittivity of the dielectric medium between the plates rises, the capacitance of the pairs of plates that make up a capacitive sensor often increases [12]. However, there is a tradeoff between these sensors' sensitivity and precision. Additionally, these sensors provide analog signals that are susceptible to disturbances [13]. To overcome these problems, some soft materials were introduced. Wang *et al.* evidenced a force sensor composed of polyvinylidene fluoride fabrics that has exceptional flexibility and breathability as well as good sensitivity and reactivity to external mechanical forces [14]. Besides, Ruben *et al.* explained that it is possible to create a flexible and multilayer capacitive microfluidic normal force sensor with a 5*5 taxel array by using liquid metal-filled microfluidic channels as the capacitive plates and conductive [15]. Nevertheless, based on a flexible titanium construction, a 5 mm diameter tri-axial force sensor has been constructed, and the deformations are monitored using reflecting measurements with three optical fibers. Its axial and radial ranges are 2.5 N and 1.7 N, respectively [16]. Even though these designs overcome the electromagnetic interference, they cannot work wirelessly. Moreover, these methods still need the computational analysis to compare the output signal. Therefore, it is very necessary to design a sensitive sensor with the properties of flexible, high stretchability and a naked eye comparison that works wirelessly against electromagnetic interference.

As a kind of popular smart material, liquid crystal elastomers and networks have become the materials of choice for the fabrication of bio-inspired fields [17-18]. Infrequently have liquid crystal elastomers (LCEs) been thought of as optical strain sensors. A wide range of systems, including biological tissues and biomedical devices, might potentially be studied and tested using these materials due to their outstanding mix of physical properties. According to Mistry’s work, when mechanically strained, acrylate-based isotropic LCE display a classical isotropic rubber response with high strain-optic coefficients and high compliances. [19]. But it can only distinguish the

magnitude of the force by the different kinds of colors, which is not sensitive enough. For further application, many groups combined some functional materials with the liquid crystal elastomer to form a liquid crystal elastomer-based composite material [20-23]. Here the aggregation-induced emission (AIE) material was worth being introduced. The AIE fluorogens are extremely emissive in aggregation because of the restriction of rotation within the molecule, which is the contrary of aggregation-induced quenching [24-26]. AIE materials and liquid crystal materials have been combined in several studies, such as display [27-29], ions detection [30] and temperature sensing [31-33]. Nevertheless, it is the first time to apply the AIE-featured LCE into the force sensor.

8.2 Materials

The liquid crystal mesogen 1,4-Bis-[4-(3-aryloyloxypropyloxy) benzoyloxy]-2-methylbenzene (RM257, 95%) was provided by Nanjing Leyao Technology Co. Ltd. (China). Pentaerythritol tetrakis (3-mercaptopropionate) (PETMP, ⩾ 95%) was purchased from Shanghai D&B biological Science and Technology Co. Ltd. (China). 2,2'-[1,2-Ethylenedioxy] diethanethiol (EDDET, 95%) and Dipropylamine (DPA, 99%) were obtained from Macklin (China). N,N-Dimethylformamide (DMF) was purchased from Shanghai Lingfeng Chemical Reagent Co. Ltd. (China). The TPE-PPE, as the AIE material here, was supplied by Beihang University. The chemical structures of RM257, PETMP, EDDET, DPA and TPE-PPE are shown in Figure 8.1. The images of LCE were captured by a digital single lens reflex (SLR) camera (Nikon D7100). The fluorescence intensity was obtained from processing the images, which were captured by a digital SLR camera (Nikon D7100), where the shutter speed of the digital SLR camera was 1/60 s and the ISO sensitivity was ISO 1250 (ISO is short for International Organization for Standardization). The fluorescence spectrum was obtained by microspectrophotometer (CRAIC technologies

Inc.). The mixtures were produced by the mixer from SCILOGEX (MX-S). The Milli-Q water purification system (Millipore, Bedford, MA) was operated to prepare all aqueous solutions with DI water.

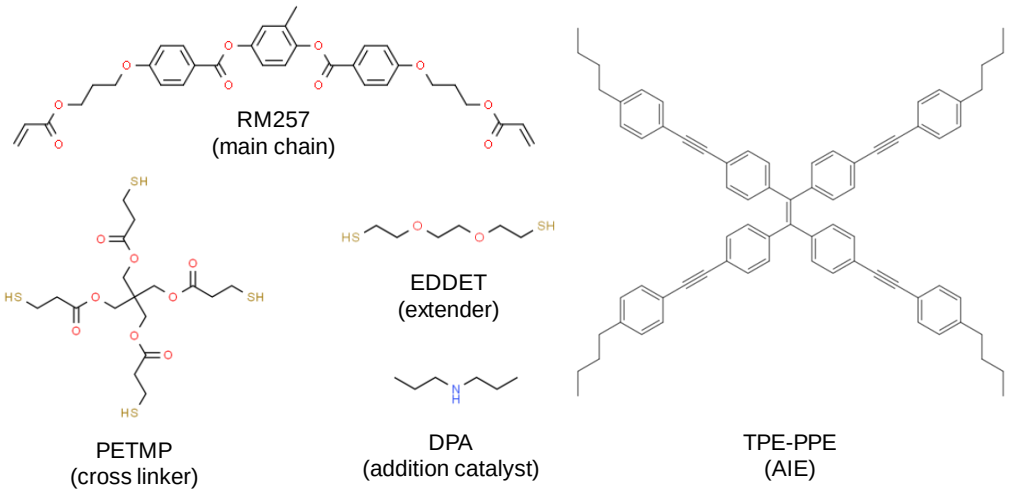

Figure 8.1 Chemical structures of RM257, PETMP, EDDET, DPA and TPE-PPE used in the formation of fluorescent liquid crystal elastomers.

Table 8.1 The compositions of LCE.

	Main Chain	Cross Linker	Extender	AIE	Addition Catalyst
Chemicals	RM257	PETMP	EDDET	TPE-PPE	DPA
Mole	2.1 mmol	0.24 mmol	1.52 mmol	/	/
Weight or volume	1236.08 mg	277.10 mg	117.28 mg	0.6 mg	5 μl

8.3 Preparation of the fluorescence LCE

The preparation method of the LCE was based on two-step crosslinking with a small amount of change [34-38]. To make 1.6 g of elastomer, firstly, 1236.08 mg (2.1 mmol) RM257 was dissolved into 1 ml DMF, and heated to 85 ˚C for the purpose of hydrotropy. After cooling to room temperature, 277.10 mg (1.52 mmol) of extender EDDET and 117.28 mg (0.24 mmol) of cross-linker PETMP were added into the mixture. The catalyst DPA was dissolved into DMF to form a DPA-DMF solution with a 2 % (v/v) concentration of DPA. After the RM

mixture had dissolved completely, 250 μl of the prepared 2 % (v/v) catalyst DPA-DMF solution was added into the RMs mixture to catalyze the polymerization. The dilution of DPA is to prevent the catalytic reaction from being too violent and causing heterogeneous polymerization Then, the mixture was treated by the mixer to ensure even mixing. After that, the mixture was cast into a rectangular Teflon mold (10 mm × 3 mm × 1 mm) and degassed for 5 min. Later, the mixture was solidified in the mold at room temperature for 24 hours. Finally, after drying in an oven at 85 ˚C for solvent evaporation and cooling down at the room temperature for 2 h, a loosely cross-linked LCE was achieved.

8.4 Results and discussion

8.3.1 Determination of the optimum concentration of TPE-PPE

Since TPE-PPE is a well-known AIE (aggregation-induced emission) luminogen, to investigate its property of AIE-activation and the relationship between the concentration and photoluminescence (PL), several mixture samples with 5CB and different concentrations of TPE-PPE between 0.1 wt% ~ 0.005 wt% were prepared and the luminescence were tested. Considering both the fluorescence changing and the TPE-PPE's usage, the concentration of TPE is selected to be as small as possible while ensuring the change in fluorescence intensity is sufficiently obvious during stretching.

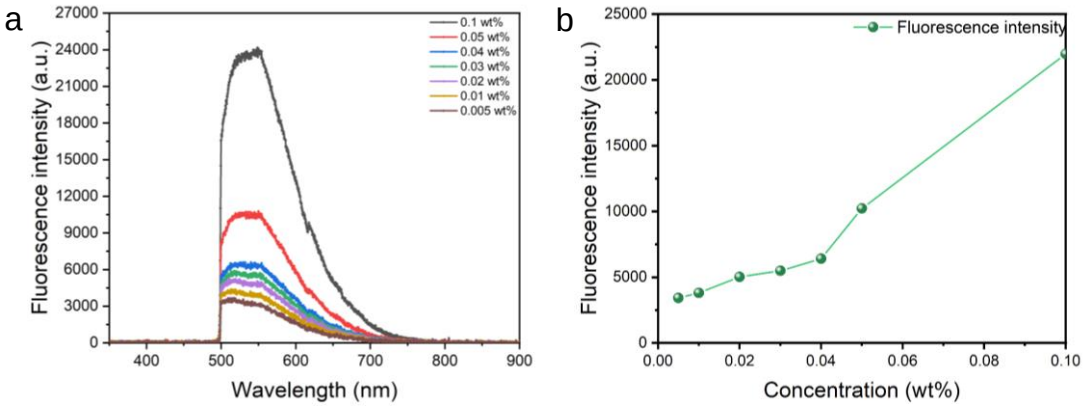

Figure 8.2 The curve of fluorescence intensity for different concentrations of TPE-PPE.

Here, four groups of mixtures with TPE-PPE concentration of 0.1 wt%, 0.05 wt%, 0.01 wt% and 0.005 wt% were obtained. As shown in Figure 8.2, with increasing of TPE-PPE concentration, the fluorescence intensity of the mixtures under UV excitation (365 nm) become stronger. The change in fluorescence intensity at the concentrations between 0.01 wt% and 0.005 wt% is too small to be distinguished by the naked eye. Another three groups of mixture (0.04 wt%, 0.03 wt%, 0.02 wt%) was inserted between concentrations of 0.05 wt% and 0.01 wt%. For our design of the sensor, the LCE will be stretched up to approximately 4 times of its original length. A concentration of 0.05 wt% was chosen as the basis for the later experiments.

8.3.2 The strain to failure of the LCE

Because only the first step crosslinking reaction was carried out from the two-step crosslinking method, the obtained LCE possesses a greater tensile capacity than normal LCE made by the complete two-step crosslinking method. Figure 8.3 shows the LCE in the tensile-testing machine and excited by the UV light (365 nm, 0.84 mW/cm^2). In the original unstretched state, the fluorescent LCE was 3.01 mm wide, 1.33 mm thick and 15 mm long.

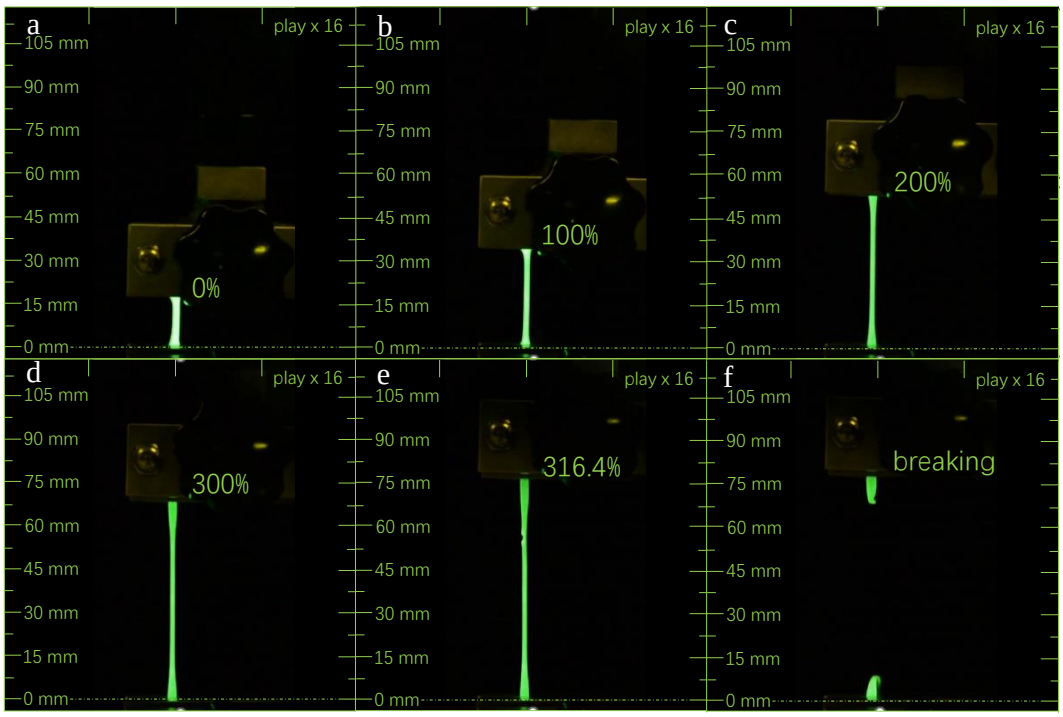

Figure 8.3 Photographs showing that the fluorescent LCE was stretched to over 300% strain before breaking. (a) the LCE before stretching; (b) the strain of 100%; (c) the strain of 200%; (d) the strain of 300%; (e) the maximum strain of 316.4%; (f) the moment of LCE's breaking.

Here, the standard for tensile stress-strain performance in this experiment is National Standard GB/T528-2009. According to this standard, the tensile strain S_{strain} can be expressed as

$$S_{strain} = \frac{100\%(L-L_0)}{L_0}, \tag{8-1}$$

where L is the final length of the LCE and the L_0 is the original length of the LCE. The tensile stress S_{stress} can be described as

$$S_{stress} = \frac{F}{Wt}, \tag{8-2}$$

where F is the force applied to the LCE, W is the width of the clamp in the tensile-testing machine, and t is the thickness of the LCE sample at the cutter area. The elongation E can be obtained by

$$E = \frac{100(L-L_0)}{L_0} . \quad (8\text{-}3)$$

The data of the LCE ‘s stretchability was collected and plotted into Figure 8.4. The red curve shows the “strain – stress” relationship (left axis). The blue curve shows the “strain - force” relationship (right axis). From the data collected from the tensile-testing machine, the maximum elongation is 44.68 mm, the maximum strain is 316.4%, the maximum stress is 2.246 MPa, and the maximum force is 9.64 N.

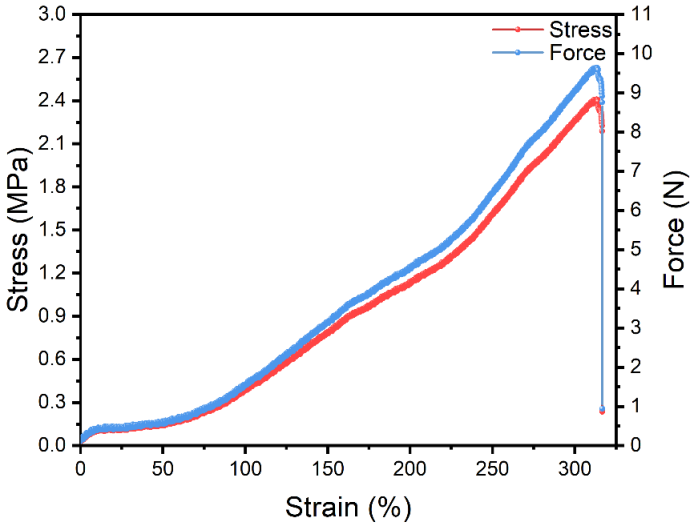

Figure 8.4 The relationship among the stress, strain and force. The red curve shows the “strain – stress” relationship (left axis). The blue curve shows the “strain - force” relationship (right axis).

8.3.3 The fluorescence characteristic of the LCE

When exposed to UV illumination (365 nm, 0.84 mW/cm^2), the LCE will present green fluorescence. The changing process of the LCE’s fluorescence intensity can be recorded into a video by the digital single lens reflex camera, and the fluorescence intensity at each stage can be extracted through a code program. The method is letting the loop code catch fluorescence intensity from the video each 0.1 s. The code is shown below. This code will add up the fluorescence signals from the pixels every 0.1 s in the video.

```
macro "Auto Measure and Save"
{
      dir_saving = getDirectory("G:\data\sample\0.1s");
      dir_processing = getDirectory("G:\data\sample\0.1s batching")
      list(i=0; i < list.length; i++)
      {
           open(list[i]);//open each image
           //Measure the fluorescence
           run("8-bit");
           setAutoThreshold("Default dark");
           //run("Threshold...");
           //setTool("wand");
           doWand(571, 686);
           run("Measure");
           saveAs("tiff", dir_saving + getTitle)
           close();
       }
}
```

After reading the fluorescence intensity at each stage, the “strain - force” relationship can be compared with “strain - fluorescence” relationship. As shown in Figure 8.5, the orange curve shows the “strain – force” relationship (left axis). The cyan curve shows the “strain - fluorescence” relationship (right axis).

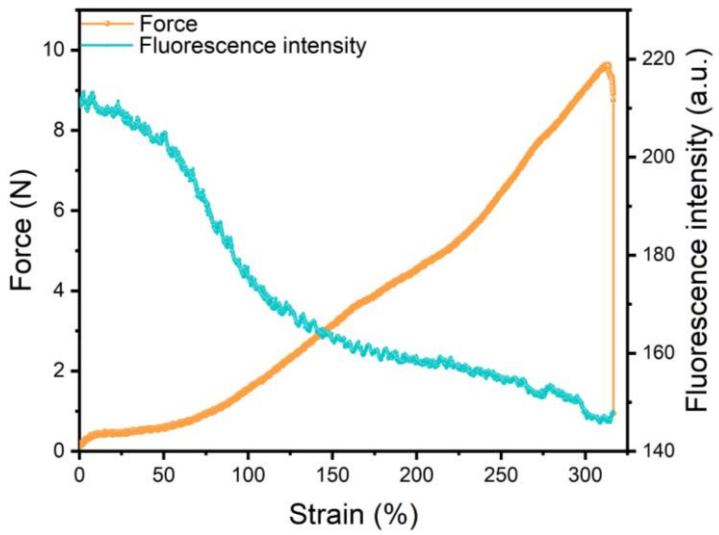

Figure 8.5 The relationship between strain, fluorescence intensity and force. The orange curve shows the “strain – force” relationship (left axis). The cyan curve shows the “strain - fluorescence” relationship (right axis).

After the reprocessing of the data, the “strain - force” and “strain - fluorescence” relationships can be combined and transferred into “fluorescence - force” relationship. As plotted in Figure 8.6, the trend of the change in fluorescence intensity and the fitted trend can be seen. The variation of the fluorescence intensity, ΔI, can be predicted from

$$\Delta I = -17.38 + 26.37 \times \left(1 - e^{-\frac{F}{25.60}}\right) + 61.22 \times (1 - e^{-\frac{F}{0.38}}) , \qquad (8\text{-}4)$$

where F is the force applied to the LCE, ΔI is the fluorescence intensity that the LCE presented under the UV exposure (365 nm, 0.84 mW/cm^2), and the goodness of fit is $R^2 = 0.99376$. This is just a data fit to the formulaic determination of the fluorescence intensity. The trend of the fluorescence change fits quite well with this function, but the function doesn’t represent some exact physical meaning. With the increasement of applied force, the fluorescence intensity decreased and the change of fluorescence intensity increased.

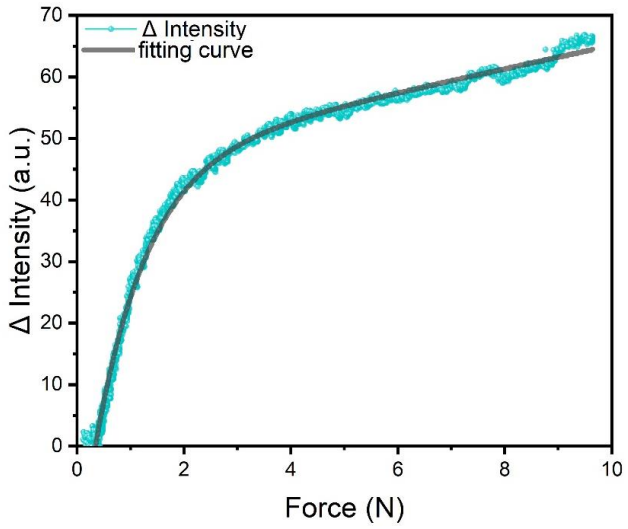

Figure 8.6 The relationship between the force and fluorescence intensity. The cyan curve is the variation of the fluorescence intensity ΔI, the gray curve is the fitting curve of it.

8.3.4 The force sensing performance

Some demonstrations were added into this project to verify the sensor’s

performance. There is a billiard ball (30.28 g), a toy (59.08 g) and an orange (83.87 g). The fluorescent LCE gives $\Delta I = 18.686\ (a.u.)$ for the billiard ball, corresponding to a calculated force of 0.3 N, so that the weight is 30.61 g, which is within error of 1.71 g with the real weight (30.28 g). The fluorescent LCE gives $\Delta I = 30.047\ (a.u.)$ for the toy, corresponding to a calculated force of 0.59 N, so that the weight is 60.20 g, which is within error of 1.71 g with the real weight (59.08 g). The fluorescent LCE gives $\Delta I = 37.645\ (a.u.)$ for the orange, corresponding to a calculated force of 0.823 N, so that the weight is 83.97 g, which is within error of 1.71 g with the real weight (83.87 g). The images of target objects testing with the fluorescent LCE are shown as below (Figure 8.7).

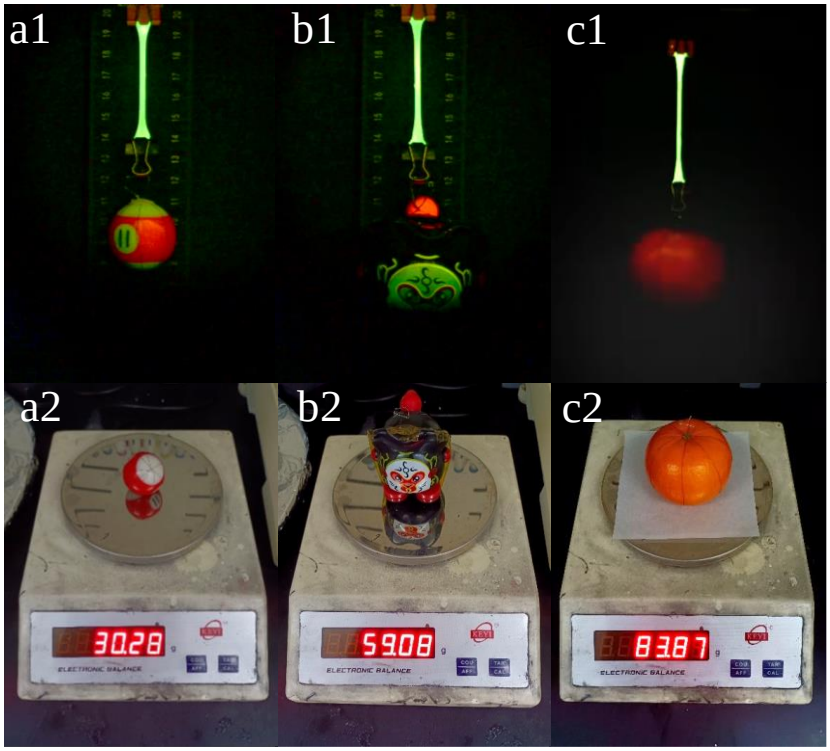

Figure 8.7 Images of target objects testing with the fluorescent LCE. Group 1 is the real testing image captured by the digital single lens reflex camera. Group 2 shows the objects weight measured by the electronic balance. (a1-a2) a billiard (30.28 g); (b1-b2) a toy (59.08 g); (c1-c2) an orange (83.87 g).

8.5 Summary

A fluorescence force sensor was achieved in this project. It can measure the

weight of the objects or detect the force between the objects at both ends of the LCE. This design of fluorescence force sensor has an applicable range, which is 0 ~ 2.5 N. Before broken or over range deformation, this fluorescence force sensor can recover to its original state quickly on a hot stage of ~ 85 ˚C for several minutes. This kind of sensor can realize repeat measurement. In some situation that are inconvenient for direct measurement, such as in inaccessible distances, liquid environments and toxic environments, this sensor will show its significance. In addition, under non-quantitative detection, the intensity of the forces can be roughly and conveniently compared by the different intensities of fluorescence. In summary, this work provides inspiration and a platform for a new generation of remotely interrogated detection via optical means.

References

1. Park, J. J.; Hyun, W. J.; Mun, S. C.; Park, Y. T.; Park, O. O. Highly stretchable and wearable graphene strain sensors with controllable sensitivity for human motion monitoring, *ACS Appl. Mater. Inter.* **2015,** 7, 6317-6324.
2. Khan, Y.; Ostfeld, A. E.; Lochner, C. M. A. Pierre, A. C. Arias, Monitoring of vital signs with flexible and wearable medical devices, *Adv. Mater.* **2016,** 28, 4373-4395.
3. Darabi, M. A.; Khosrozadeh, A.; Wang, Q.; Xing, M. Gum sensor: a stretchable, wearable, and foldable sensor based on carbon nanotube/chewing gum membrane, *ACS Appl. Mater. Inter.* **2015,** 7, 26195-26205.
4. Cheng, Y.; Wang, R.; Sun, J.; Gao, L. A stretchable and highly sensitive graphene-based fiber for sensing tensile strain, bending, and torsion, *Adv. Mater.* **2015**, 27, 7365-7371.
5. Wang, C.; Li, X.; Gao, E.; Jian, M.; Xia, K.; Wang, Q.; Xu, Z.; Ren, T.; Zhang, Y. Carbonized silk fabric for stretchable, highly sensitive, and wearable strain sensors, *Adv. Mater.* **2016**, 28, 6640-6648.
6. Yang, S.; Chen, Y. C.; Nicolini, L.; Pasupathy, P.; Sacks, J.; Su, B.; Yang, R.; Sanchez, D.; Chang, Y.; Wang, P.; Schnyer, D.; Neikirk, D.; Lu, N. Cut-and-paste" manufacture of multiparametric epidermal sensor systems, *Adv. Mater.* **2015**, 27, 6423-6430.
7. Trung, T. Q.; Lee, N. E. Flexible and stretchable physical sensor integrated platforms for wearable human-activity monitoring and personal healthcare, *Adv. Mater,* **2016**, 28, 4338-4372.
8. Amjadi, M.; Kyung, K. U.; Park, I.; Sitti, M. Stretchable, skin-mountable, and wearable strain sensors and their potential applications: a review, *Adv. Funct. Mater.* **2016**, 26, 1678-1698.
9. Amjadi, M.; Pichitpajongkit, A.; Lee, S.; Ryu, S.; Park, I. Highly stretchable and sensitive strain sensor based on silver nanowire-elastomer nanocomposite, *ACS Nano* **2014**, 8, 5154-5163.
10. Wang, Y. L.; Hao, J.; Huang, Z. Q.; Zheng, G. Q.; Dai, K.; Liu, C. T.; Shen, C. Y. Flexible Electrically Resistive-type Strain Sensors Based on Reduced Graphene

Oxide-decorated Electrospun Polymer Fibrous Mats for Human Motion Monitoring. *Carbon* **2018**, 126, 360-371.

11. Wang, X. D.; Zhou, J.; Song, J. H.; Liu, J.; Xu, N. S.; Wang, Z. L. Piezoelectric Field Effect Transistor and Nanoforce Sensor Based on a Single ZnO Nanowire. *Nano Lett.* 2006, **6**, 2768-2772.
12. Yousef, H.; Boukallel, M.; Althoefer, K. Tactile Sensing for Dexterous in-hand Manipulation in Robotics—A Review. *Sens. Actuators, A* **2011**, 167, 171-187.
13. Lü, X. Z.; Lu, W. K.; Zhu, C. C. Compensated SAW Yarn Tension Sensor. *IEEE Trans. Instrum. Meas.* **2014**, 63, 3162-3168.
14. Wang, Y. R.; Zheng, J. M.; Ren, G. Y.; Zhang, P. H.; Xu, C. A flexible piezoelectric force sensor based on PVDF fabrics. *Smart Mater. Struct.* **2011**, 20, 045009.
15. Wong, R. D. P.; Posner, J. D.; Santos, V. J. Flexible microfluidic normal force sensor skin for tactile feedback. *Sens. Actuators, A* **2012**, 179, 62-69.
16. Peirs, J.; Clijnen, J.; Reynaerts, D.; Brussel, H. V.; Herijgers, P.; Corteville, B.; Boone, S. A micro-optical force sensor for force feedback during minimally invasive robotic surgery. *Sens. Actuators, A* **2004**, 115, 447-455.
17. White, T.; Verduzco, R. Liquid Crystal Elastomers: Emerging Trends and Applications. *Soft Matter* **2017**, 13, 4320.
18. Zhang, W.; Nan, Y. F.; Wu, Z. X.; Shen, Y. J.; Luo, D. Photothermal-Driven Liquid Crystal Elastomers: Materials, Alignment and Applications. *Molecules* **2022**, 27, 4330.
19. Mistry, D.; Nikkhou, M.; Raistrick, T.; Hussain, M.; Jull, E.; Baker, D. L.; Gleeson, H. F. Isotropic Liquid Crystal Elastomers as Exceptional Photoelastic Strain Sensors. *Macromolecules* **2020**, 53, 3709-3718.
20. Xing, H.; Li, J.; Shi, Y.; Guo, J.; Wei, J. Thermally Driven Photonic Actuator Based on Silica Opal Photonic Crystal with Liquid Crystal Elastomer. *ACS Appl. Mater. Inter.* **2016**, 8, 9440-9445.
21. Brannum, M. T.; Steele, A. M.; Venetos, M. C.; Korley, L. T. J.; Wnek, G. E.; White, T. J. Light Control with Liquid Crystalline Elastomers. *Adv. Opt. Mater.* **2019**, 7, 1801683.

22. Wu, G.; Jiang, Y.; Xu, D.; Tang, H.; Liang, X.; Li, G. Thermoresponsive Inverse Opal Films Fabricated with Liquid-crystal Elastomers and Nematic Liquid Crystals. *Langmuir* **2011**, 27, 1505-1509.
23. Wei, W.; Zhang, Z.; Wei, J.; Li, X.; Guo, J. Phototriggered Selective Actuation and Self-Oscillating in Dual-Phase Liquid Crystal Photonic Actuators. *Adv. Opt. Mater.* **2018**, 6, 1800131.
24. Luo, J.; Xie, Z.; Lam, J. W. Y.; Cheng, L.; Chen, H.; Qiu, C.; Kwok, H. S.; Zhan, X.; Liu, Y.; Zhu, D.; Tang, B. Z. Aggregation-Induced Emission of 1-Methyl-1,2,3,4,5-Pentaphenylsilole. *Chem. Commun.* **2001**, 18, 1740-1741.
25. Chen, J.; Law, C. C. W.; Lam, J. W. Y.; Dong, Y.; Lo, S. M. F.; Williams, I. D.; Zhu, D.; Tang, B. Z. Synthesis, Light Emission, Nanoaggregation, and Restricted Intramolecular Rotation of 1,1-Substituted 2,3,4,5-Tetraphenylsiloles. *Chem. Mater.* **2003**, 15, 1535-1546.
26. Mei, J.; Hong, Y.; Lam, J. W. Y.; Qin, A.; Tang, Y.; Tang, B. Z. Aggregation-Induced Emission: The Whole is More Brilliant than the Parts. *Adv. Mater.* **2014**, 26, 5429-5479.
27. Zhao, D. Y.; Fan, F.; Cheng, J.; Zhang, Y. L.; Wong, K. S.; Chigrinov, V. G.; Kwok, H. S.; Guo, L.; Tang, B. Z. Light-Emitting Liquid Crystal Displays Based on an Aggregation-Induced Emission Luminogen. *Adv. Opt. Mater.* **2014**, 3, 199-202.
28. Zhao, D. Y.; He, H. X.; Gu, X. G.; Guo, L.; Wongm, K. S.; Lam, J. W. Y.; Tang, B. Z. Circularly Polarized Luminescence and a Reflective Photoluminescent Chiral Nematic Liquid Crystal Display Based on an Aggregation-Induced Emission Luminogen. *Adv. Opt. Mater.* **2016**, 4, 534-539.
29. Zhao, D. Y.; Bi, W. H.; Tang, B. Z. A Light-Emitting Liquid Crystal Display Device without Polarizers and Alignment Layers. *Adv. Opt. Mater.* **2021**, 9, 2100489.
30. Du, X. X.; Liu, Y. J.; Wang, F.; Zhao, D. Y.; Gleeson, H. F.; Luo, D. A Fluorescence Sensor for Pb^{2+} Detection Based on Liquid Crystals and Aggregation-Induced Emission Luminogens. *ACS Appl. Mater. Inter.* **2021**, 13, 22361-22367.

31. Li, W. L.; Huang, D.; Wang, J.; Shen, W. J.; Chen, L. Z.; Yang, S. Y.; Zhu, M. F.; Tang, B. Z.; Liang, G. D.; Xu, Z. X. A Novel Stimuli-Responsive Fluorescent Elastomer Based on An AIE Mechanism. *Polym. Chem.* **2015**, 6, 8194-8202.
32. Liu, L.; Wang, M.; Guo, L. X.; Sun, Y.; Zhang, X. Q.; Lin, B. P.; Yang, H. Aggregation-Induced Emission Luminogen-Functionalized Liquid Crystal Elastomer Soft Actuators. *Macromolecules* **2018**, 12, 4516–4524.
33. Wang, J.; Wang, T.; Jiang, Q.; Zhang, Y. P.; Qiu, Y.; Wang, H.; Yin, G. C.; Liao, Y. G.; Xie, X. L. Configuration-Dependent Liquid Crystal and Gel Behaviors of Tetraphenylethene-Containing Main-Chain Copolyesters. *Macromol. Rapid Commun.* **2022**, 2200154,1-8.
34. Finkelmann, H.; Kock, H. J.; Rehage, G. Liquid Crystalline Elastomers - A New Type of Liquid Crystalline Materia. Makromol. *Chem*. **1981**, 2, 317-322.
35. White, T. J.; Broer, D. J. Programmable and Adaptive Mechanics with Liquid Crystal Polymer Networks and Elastomers. *Nat. Mater.* **2015**, 14, 1087-98.
36. Ware, T. H.; McConney, M. E.; Wie, J. J.; Tondiglia, V. P.; White, T. J. Voxelated Liquid Crystal Elastomers. *Science*. **2015**, 347, 982-4.
37. Ware, T. H.; White, T. J. Programmed Liquid Crystal Elastomers with Tunable Actuation Strain. *Polym. Chem.* **2015**, 6, 4835-4844.
38. Xia, Y.; Zhang, X.; Yang, S. Instant Locking of Molecular Ordering in Liquid Crystal Elastomers by Oxygen-Mediated Thi-ol-Acrylate Click Reactions. *Angew. Chem. Int. Ed. Engl.* **2018**, 57, 5665-5668.

Chapter 9 Conclusion and Further Works

9.1 Conclusion

In this thesis, finished and ongoing work has demonstrated that LC-based sensors are potentially very sensitive and naturally amplifying. Besides, LC-based sensor technology also lends itself to point of care testing. It must be mentioned that the LCs can be used to make to very low-cost devices, which can decrease the cost of device. All these advantages provide the motivation for the development of LC-based sensors. The form in which liquid crystals exist in the sensing system (droplets, films, elastomers, etc.) does not limit their contributions in the field of sensors. The aim proposed at the beginning of the thesis has been preliminarily achieved according to the works presented above. Each form of the liquid crystal has its own special application in the field of sensor according to their characteristics. The combination of liquid crystals and the AIE materials is very successful and show a greater promise for future work. After all, the sensors based on liquid crystals are cheap and easy read compared to the traditional non-liquid crystal sensors. It is still well worth exploring a wider field of liquid-crystal-based sensing.

9.2 Further plan

In the next stage, these very attractive advantages of LC-based sensor need to be set against a number of significant challenges. The liquid crystal droplets can be Besides droplets, films and elastomers, there are still some possibilities to study more forms of liquid crystals in sensing field, such as the liquid crystal shell for transporting and releasing medicines.

If these benefits can be combined together to solve specific problems, a novel useful design will be achieved. What is more, some control theory deserves to be added into the sensors, such as temperature control, electronic control, magnetron. As a result, a controllable multifunctional LC-based

sensor will be realized through integrated design.

It can provide new inspirations for the sensor from the perspective of bionics. Now I have started a work on a bilayer LC-based bionic flower equipped with sensing components design, which can response to different wavelengths of irradiate light and perform different bionic commands.